

THE DEVELOPMENT OF TECHNIQUES TO PREPARE  
AND PROBE AT SINGLE ATOM RESOLUTION  
STRONGLY INTERACTING QUANTUM SYSTEMS  
OF ULTRACOLD ATOMS

---

**Martin David Shotter**

A thesis submitted in partial fulfilment of  
the requirements for the degree of  
Doctor of Philosophy at the University of Oxford



Christ Church  
University of Oxford  
Trinity Term 2009



# ABSTRACT

---

## **The development of techniques to prepare and probe at single atom resolution strongly interacting quantum systems of ultracold atoms**

**Martin David Shotton, Christ Church, Oxford University**

DPhil Thesis, Trinity Term 2009

Strongly interacting many-body quantum dynamics are inherently extremely complex. This makes strongly interacting quantum systems very hard to simulate, predict or understand. In certain circumstances, strongly interacting quantum dynamics may be observed in samples of ultracold atoms. Ultracold atomic systems have unique advantages for the investigation of such dynamics: further to the long coherence times and extremely low temperatures, there is the potential to have a great deal of control over the basic quantum processes. This suggests the possibility using systems of ultracold atoms as a quantum simulator, in which the quantum dynamics of one system is simulated by an experiment on a different system, the quantum simulator. Quantum simulation is a part of the emerging field of quantum information processing.

Up to the present time, observation of strongly interacting quantum states of ultracold atoms has been almost entirely limited to time-of-flight imaging of many thousands of atoms. Although one can learn much about the overall nature of the quantum states by this method, detail at the level of individual atoms is lost. My research has focussed on developing novel experimental techniques to make it possible to measure these complex states at the single atom level. In particular, I have developed methods which are capable of making unprecedentedly direct and detailed observation of hundreds or thousands of strongly interacting atoms, at the resolution of single atoms, and with a spatial resolution capable of reliably resolving atoms in individual wells of an optical lattice.

In this thesis, I describe work that I have carried out during the period of my DPhil, primarily concerned with the design and simulation of these techniques. I have also investigated new methods to prepare the initial quantum states needed for quantum simulation. In addition, I describe earlier work in which I constructed apparatus for, and reached, Bose-Einstein Condensation.

# ACKNOWLEDGEMENTS

---

I would like to thank my supervisor, Chris Foot, for his discussions and his support, particularly during the period of my illness. I'd also like to thank all the members of the Clarendon BEC group over the years, particularly those who I've worked closely with: Rachel, who showed a newbie the ropes (or at least the coaxes); Andrian and Ben, fellow basement troglodytes; and Dimitris, my most recent co-conspirator. My friends at Oxford kept me in at least passing contact with reality, for which I'm very grateful. In particular, I'd like to mention Myrto, who stuck with me while I was ill, and everyone at KEEN, with whom I've shared many eventful and happy hours. But above all, I'd like to thank my parents for the love and support they've always shown me.

# CONTENTS

---

<b>1</b>	<b>Introduction and motivation</b>	<b>1</b>
1.1	Structure of the thesis . . . . .	3
<b>2</b>	<b>Survey of literature related to strongly interacting systems of ultracold atoms and observation of individual ultracold atoms</b>	<b>5</b>
2.1	Ultracold atoms in optical lattices: the Bose-Hubbard model and a quantum phase transition . . . . .	5
2.2	Quantum simulation and quantum computation . . . . .	8
2.3	Detecting signatures of strongly interacting quantum systems of ultracold atoms . . . . .	11
2.3.1	Number squeezing and the Mott insulator transition . . . . .	11
2.3.2	Measurements of Mott insulator structure . . . . .	13
2.3.3	Direct measurement of sub-Poissonian statistics . . . . .	15
2.3.4	A lattice of double wells . . . . .	15
2.3.5	Strong interactions at low density in one dimensional systems . . . . .	16
2.4	The observation of low numbers of ultracold atoms using fluorescent imaging . . . . .	16
2.4.1	Fluorescent imaging in a three-dimensional optical lattice of period 5 microns . . . . .	16
2.4.2	Fluorescent imaging in a two-dimensional optical lattice of period 640 nanometres . . . . .	17
2.4.3	Fluorescent imaging of a single dipole trap immersed in a MOT . . . . .	20
2.5	Other techniques used to observe low numbers of ultracold atoms . . . . .	21
2.6	Summary . . . . .	22

<b>3</b>	<b>Constructing apparatus for Bose-Einstein Condensation and reaching quantum degeneracy</b>	<b>23</b>
3.1	Cooling requirements for quantum degeneracy . . . . .	23
3.2	Apparatus . . . . .	25
3.2.1	The magneto-optical trap . . . . .	25
3.2.2	The magnetic trap . . . . .	25
3.2.3	The laser beams . . . . .	26
3.2.4	The cooling sequence . . . . .	26
3.3	Reaching quantum degeneracy . . . . .	27
<b>4</b>	<b>A novel technique to probe strongly interacting ultracold atomic systems at high spatial and single atom resolution</b>	<b>36</b>
4.1	The criteria for observation of individual atoms within a periodic optical potential . . . . .	36
4.2	Comparison of techniques . . . . .	37
4.3	Fluorescent imaging and the criteria for the observation of individual atoms in a strongly interacting quantum system . . . . .	39
4.3.1	Resolution, distinguishability and spatial period . . . . .	39
4.3.2	Signal-to-noise ratio . . . . .	41
4.3.3	Light-assisted collisions . . . . .	42
4.4	The accordion lattice . . . . .	44
4.4.1	Collimation of lattice beams for the counter-propagating accordion lattice . . . . .	48
4.4.2	Maximum distance between accordion lattice sites . . . . .	51
4.5	The imaging lattice . . . . .	52
4.5.1	Practical considerations . . . . .	54
4.6	Cooling while detecting in the imaging lattice . . . . .	55
4.6.1	Outline of cooling methods . . . . .	56
4.6.2	The choice of cooling method . . . . .	57
4.7	Fluorescent imaging of atoms trapped in the imaging lattice . . . . .	59

4.7.1	Cooling in three dimensions . . . . .	60
4.7.2	Shared or separate optical elements . . . . .	61
4.7.3	Translation of the imaging lattice and three-dimensional imaging . . . . .	62
4.7.4	Fluorescence from out-of-plane atoms . . . . .	62
4.7.5	Coherence and reabsorption of scattered radiation . . . . .	63
<b>5</b>	<b>Theoretical and computational methods used to model the imaging lattice technique</b>	<b>65</b>
5.1	The mechanisms of polarisation gradient cooling in free space . . . . .	65
5.1.1	Orthogonal linear polarisations . . . . .	66
5.1.2	Orthogonal circular polarisations . . . . .	67
5.2	The mechanisms of polarisation gradient cooling of confined atoms . . . . .	68
5.2.1	Orthogonal linear polarisations . . . . .	69
5.2.2	Orthogonal circular polarisations . . . . .	71
5.3	Three-dimensional polarisation gradient cooling of confined atoms . . . . .	71
5.4	Simplification of the simulated system . . . . .	72
5.4.1	The imaging lattice . . . . .	72
5.4.2	Restricting the number of participating states using repumping . . . . .	74
5.5	Quantum description of polarisation gradient cooling . . . . .	74
5.5.1	Unitary quantum dynamics . . . . .	75
5.5.2	Relaxation mechanisms of the internal states . . . . .	76
5.5.3	Explicit retention of the excited states . . . . .	76
5.5.4	The Wigner transformation . . . . .	77
5.6	The semi-classical approximation . . . . .	78
5.7	Conversion to Langevin form . . . . .	79
5.8	Unravelling the Optical Bloch equations . . . . .	81
5.8.1	Continuous and discrete recoil momentum terms . . . . .	82
5.9	Computational methods . . . . .	82
5.10	Comment on nature of the simulation . . . . .	83
5.11	Extended Monte Carlo analysis . . . . .	83

---

5.11.1	The ‘measure’ and ‘events’ . . . . .	84
5.11.2	System dynamics when representative start vectors are known .	85
5.11.3	Finding representative start vectors . . . . .	86
5.11.4	Several daughters vectors per mother vector . . . . .	88
5.11.5	Focussing the analysis on less frequented regions . . . . .	89
5.11.6	The choice of points on the measure . . . . .	90
5.11.7	Extended Monte Carlo simulation: summary . . . . .	91
5.12	Markovian and non-Markovian analyses . . . . .	92
5.12.1	Markovian probability analysis . . . . .	92
5.12.2	The Markovian master equation . . . . .	94
5.12.3	Outline of non-Markovian treatment . . . . .	94
5.13	Implementation of the extended Monte Carlo algorithm for the imaging lattice technique . . . . .	95
<b>6</b>	<b>The simulated performance of the imaging lattice technique</b>	<b>97</b>
6.1	Consistency testing . . . . .	97
6.2	Frictional energy loss . . . . .	99
6.2.1	Free space . . . . .	100
6.2.2	Confined atoms . . . . .	100
6.3	Specific example of atomic hopping dynamics . . . . .	103
6.3.1	Rationale . . . . .	103
6.3.2	Parameters used . . . . .	105
6.3.3	Discussion of results . . . . .	105
6.3.4	Coherence properties of the scattered light . . . . .	110
6.3.5	Reabsorption . . . . .	111
6.3.6	Summary . . . . .	113
6.4	Atomic hopping dynamics over a range of parameters . . . . .	113

<b>7</b>	<b>Summary and extensions to the accordion and imaging lattice techniques; potential for novel ultracold physics</b>	<b>116</b>
7.1	High resolution three-dimensional measurements at the level of individual atoms for arbitrary ultracold atomic configurations . . . . .	116
7.2	Minimisation of fluorescence from out-of-plane atoms whilst imaging three-dimensional samples . . . . .	119
7.3	Summary of the basic technique . . . . .	121
7.3.1	Capabilities . . . . .	121
7.3.2	An exemplar experimental design . . . . .	122
7.3.3	Practicalities . . . . .	124
7.3.4	Performance . . . . .	127
7.4	Variations on the basic technique . . . . .	128
7.4.1	Measurement of the internal state of the atoms at each site of the lattice . . . . .	128
7.4.2	Lattices and superlattices . . . . .	128
7.4.3	Generalisation of accordion lattice geometry . . . . .	129
7.4.4	Using the accordion lattice to prepare a small initial sample of atoms . . . . .	129
7.4.5	Longer time-of-flight measurements and higher group velocity samples . . . . .	131
7.4.6	The use of shorter-wavelength light . . . . .	132
7.5	Comparison with the recent experiment at Harvard . . . . .	134
7.6	Outline of prospects for novel physics . . . . .	134
7.6.1	Direct observation . . . . .	135
7.6.2	Structure and detail of quantum states . . . . .	135
7.6.3	Correlations . . . . .	136
7.6.4	Excitations and finite temperature systems . . . . .	136
7.6.5	Observation of novel phenomena with few participating particles, low atom densities, or small length scales . . . . .	137
7.6.6	Quantum simulation and computation . . . . .	137

<b>8</b>	<b>Novel techniques to prepare ultracold atomic states suitable for quantum simulation: the Mott insulator phase transition and beyond</b>	<b>139</b>
8.1	Introduction: the importance of a reproducible starting state for quantum simulators . . . . .	139
8.2	The parameters of the Bose-Hubbard Hamiltonian . . . . .	141
8.3	Calculation of Hamiltonian parameters . . . . .	142
8.4	Discussion of factors which can lead to impurities in the Mott insulator	145
8.5	RF dressing: a technique to increase the interaction strength of tunnelling ultracold atoms . . . . .	147
8.5.1	Radio-frequency dressing of optical potentials . . . . .	148
8.5.2	Calculation of Hamiltonian parameters . . . . .	151
8.5.3	Discussion of results . . . . .	151
8.6	Inter-line optical trap evaporation . . . . .	156
<b>9</b>	<b>Closing remarks</b>	<b>163</b>
<b>A</b>	<b>Abbreviations and terminology</b>	<b>166</b>
<b>B</b>	<b>The Bose-Hubbard model in the mean field approximation</b>	<b>167</b>
<b>C</b>	<b>Aspects of the derivation of the dynamical equations of polarisation gradient cooling</b>	<b>169</b>
C.1	The direction of spontaneously emitted radiation . . . . .	169
C.2	The semiclassical approximation . . . . .	170
C.3	The recoil term: Wigner transformation and small recoil momentum approximation . . . . .	172
C.4	Conversion to Langevin form . . . . .	173
C.5	The quantum Monte Carlo wave function method and the optical Bloch equation . . . . .	173

---

## INTRODUCTION AND MOTIVATION

During the late 1980s and early 1990s remarkable progress was made in the laser cooling and trapping of neutral atomic gases, resulting in temperatures in the  $\mu\text{K}$  range [59], significantly lower than any previously observed in bulk physical systems. This progress led, in 1995, to the first observation of Bose-Einstein Condensation (BEC) in atomic gases [3, 20], in which the a single quantum state is occupied by hundreds of thousands of bosonic atoms, forming a mesoscopic object with manifestly quantum properties. The physicists behind laser cooling and Bose-Einstein Condensation were awarded Nobel Prizes in 1997 and 2001 respectively.

Since 1995 there has been a great profusion of BEC experiments, and BEC related experiments, around the world. A wide array of techniques has been developed to manipulate the quantum states of the ultracold atoms, predominantly by the use of laser, magnetic and radio-frequency fields. There is a major drive to use these techniques to make and probe strongly interacting many-body quantum systems.

Many-body quantum dynamics are inherently extremely complex. This extra complexity, compared to many-body classical mechanics, stems from the radical difference in the size of the state vector in the equations of motion. Broadly speaking, for  $N$  particles in  $M$  possible quantum states, the length of the quantum state vector is proportional to  $M^N$  (for distinguishable particles<sup>1</sup>), whereas in the classical case, with

---

<sup>1</sup>Symmetry considerations reduce this figure somewhat for indistinguishable particles; nevertheless, the number of basis states is still extremely large.

$N$  particles in any possible state, the length of the classical state vector is only proportional to  $N$ . This complexity leads to properties such as quantum superposition and entanglement, which have no classical analogues. With both  $N$  and  $M$  ranging from of order one to hundreds of thousands in a typical ultracold atom experiment, computing exact quantum dynamics in strongly interacting systems<sup>2</sup> from the equations of motion quickly becomes intractable for all but the simplest of cases.

By studying the quantum dynamics of systems of ultracold atoms, with great flexibility available to tailor-make the quantum Hamiltonian, and with long coherence times, it becomes possible to study quantum dynamics in a new and powerful way; the experimentalist can, in real-time, actively control many of the aspects of the evolution of these complex quantum systems.

It is thought that, apart from the pure research interest in the study of these complex quantum states, the techniques developed will have applications beyond the immediate field. By designing the correct Hamiltonian it is possible to experimentally simulate many situations of great interest in condensed matter physics; for example it is becoming possible to probe the phase diagram of the Bose-Hubbard or Fermi-Hubbard models in 1, 2 and 3 dimensions [28, 88], or to study quantum dynamics in the analogue of a high magnetic field [43]. Taking the idea of simulation one step further, it is possible to design a Hamiltonian to perform universal quantum logical computations, analogous to the logical computations of an ordinary computer, but using quantum objects, named qubits, instead of classical bits [41]. The advantage of such a ‘quantum computer’ is that by cleverly designing the algorithms it is possible to make the great complexity of quantum many-body systems work for you, instead of against you; certain types of calculations are expected to be exponentially faster on quantum computers compared to classical computers [90]. It is worth mentioning that other potential future applications include sub-shot noise precision interferometric measurements using atomic squeezed quantum states [5].

The main focus of the research I have undertaken during my DPhil has concentrated on developing methods for direct and detailed observation of these many-atom

---

<sup>2</sup>The definition of a strongly interacting system is discussed in Section 2.3.

quantum states, in periodic potentials, at the resolution of single atoms. Up to the present time, observation of these states has been almost entirely limited to time-of-flight imaging of the momentum distribution of many thousands atoms, after their release from the confining potential. Although one can learn a lot about the overall nature of the quantum states by this method, detail at the level of individual atoms is lost. My research has been focussed on developing novel experimental techniques to probe, and eventually manipulate, these states at the single atom level.

Furthermore, I have developed new methods aimed at satisfying one of the other requirements of quantum simulation, that of preparing a simple, reproducible, starting quantum state for the many-body system. The process of measurement on a quantum mechanical state acts to destroy that state, so to gain true knowledge of a particular state many copies need to be produced, to allow repeated measurements to be made; it is only when these measurements are analysed together may a more complete picture emerge. This procedure of quantum tomography requires the ability to produce predictable, ideally identical, starting states, upon which the Hamiltonian operator then acts to produce the dynamics and states of interest. For ultracold atomic systems, this starting state is usually proposed as a Mott insulator state with a single atom in the ground state of every site of an optical lattice. Methods which I have designed to improve the purity of such a starting state will be discussed.

## **1.1 Structure of the thesis**

During my time as a DPhil student I have carried out both experimental and theoretical (modelling) work. During the first year and a half of my DPhil, I was heavily involved in practical experimental work, in building a new rubidium BEC experiment; this work is described in Chapter 3. The object of this experiment was to be the direct observation of number squeezing of ultracold atoms in a periodic optical potential. Unfortunately I fell chronically ill in the middle of this work, and was forced to more or less abandon work on my DPhil for around three years. When I recuperated from this illness enough to restart work on my DPhil there wasn't the opportunity for me to continue experimental research using this apparatus.

I therefore turned to theoretical and computational modelling of the experiments which I had originally planned for that apparatus. I took the original ideas, improved them, and spent time modelling them, with the object to design the best possible experiment to directly observe a whole class of strongly interacting quantum dynamics (with the Mott insulator transition being the primary example). This work forms the main body of my thesis, and is described in Chapters 4 to 7. In addition, the development and modelling of two other experimental techniques, for use in preparing very low entropy initial states for quantum simulation, are described in Chapter 8.

---

# SURVEY OF LITERATURE RELATED TO STRONGLY INTERACTING SYSTEMS OF ULTRACOLD ATOMS AND OBSERVATION OF INDIVIDUAL ULTRACOLD ATOMS

This chapter summarises the recent developments in the field of ultracold atomic physics which are most relevant to the work set out in this thesis. The primary physical system, ultracold atoms in an optical lattice, is outlined, and the interest in using these types of systems for probing arbitrary quantum lattice Hamiltonians is discussed. Recent experiments which have been able to detect signatures of strongly interacting physics in these systems are surveyed. As the overall aim of this work is to find techniques which will allow direct observation of these strongly interacting states, a range of experiments with the capability to count small numbers of ultracold neutral atoms are profiled.

## **2.1 Ultracold atoms in optical lattices: the Bose-Hubbard model and a quantum phase transition**

As described in Chapter 1, we are interested in systems where  $N$ , the number of atoms, and  $M$ , the number of single-atom quantum states, are big enough that the dynamics may not be easily predicted<sup>1</sup>.

---

<sup>1</sup>In reality, the number of quantum states is unbounded in the direction of positive energy; in practice we require that only  $M$  states contribute to the quantum evolution. This means that the atoms must be at a very low temperature, effectively at or near Bose-Einstein Condensation temperatures.

One well-studied example of ultracold many-body physics is the Bose-Einstein condensate itself, which typically has  $N$  of order  $10^4$  to  $10^6$ , and  $M$  of order 1. The wave function of atoms in the condensate is well approximated by a single condensate wave function, which is the solution to the non-linear Gross-Pitaevskii equation

$$\left(-\frac{\hbar^2 \nabla^2}{2m} + V(\mathbf{r}) + g|\psi(\mathbf{r}, t)|^2\right)\psi(\mathbf{r}, t) = i\hbar \frac{\partial}{\partial t} \psi(\mathbf{r}, t) \quad (2.1)$$

with  $g = 4\pi\hbar^2 a_s/m$ , where  $a_s$  is the ultracold s-wave scattering length<sup>2</sup>. As the condensate is well described by a single wave function, the many-body dynamics of Bose-Einstein Condensates are relatively easy to simulate and understand. Even in the cases there are deviations from the single-wave-function behaviour, perturbation theory may be applied, with the condensate wave function as the first term (for example in a Bogoliubov perturbation expansion).

In contrast to the dynamics of the BEC itself, for ultracold atoms in optical lattices,  $N$  and  $M$  are roughly the same order of magnitude as each other, with  $N$  and  $M$  both in the range 10 to  $10^5$ . This is potentially a more complex system; even at zero temperature, the ground state can form different phases, dependent on the Hamiltonian parameters. At some sets of parameters, such as in the vicinity of a transition between these quantum phases, the structure of the ground state is very complex. These quantum systems are the major motivating examples for the precision probing techniques developed in this thesis.

An optical lattice is formed by the interference of laser light. In one dimension, the light intensity at a point  $x$  due to two interfering laser beams, each at an angle  $\theta$  to the  $x$ -axis (see Fig. 2.1), is

$$I(x) = I_0 \sin^2\left(\frac{2\pi \cos \theta}{\lambda} x + \phi\right). \quad (2.2)$$

The light induces a time-dependent dipole moment in the atoms. For light which has a large frequency detuning from atomic resonances, spontaneous scattering processes are negligible. The energy of the time-dependent dipole moment in the light field gives rise to a dipole, or a.c. Stark, potential which for alkali metal atoms is given by

$$V_{m_F}(\mathbf{r}) = \frac{\pi c^2 \Gamma}{2\omega^3} \left( \frac{1 - P g_F m_F}{\Delta_{D_1}} + \frac{2 + P g_F m_F}{\Delta_{D_2}} \right) I(\mathbf{r}). \quad (2.3)$$

<sup>2</sup>The condensate wave function has non-standard normalisation  $\int |\psi(\mathbf{r}, t)|^2 d\mathbf{r} = N$ .

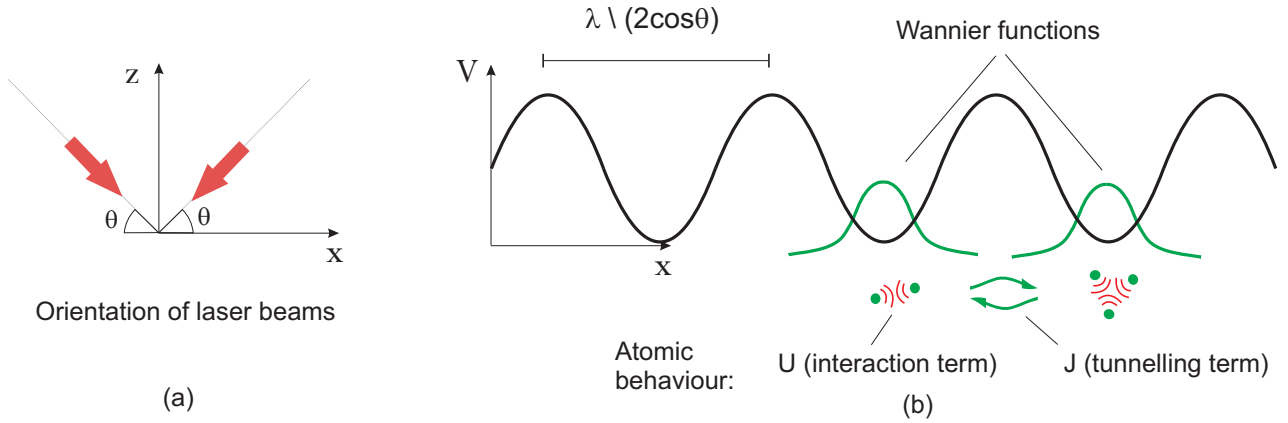


Figure 2.1: A representation of a one-dimensional optical lattice. (a) The orientation of the laser beams of Eqn. 2.3. (b) The potential energy of neutral ultracold atoms in the laser fields; along the  $x$  axis, the potential is periodic. The Wannier functions (shown in green) are the wave functions of atoms localised at single sites (see Section 8.4). The origin of the two terms of the homogeneous Bose-Hubbard Hamiltonian are shown pictorially: the inter-well tunnelling (parameter  $J$ ) and the on-site collisional interaction (parameter  $U$ ).

This equation is derived from a sum of the Clebsch-Gordon coefficients of the individual transitions, in the approximation that the laser frequency detuning from resonance is much greater than the width of the hyperfine structure [30]. Here  $m_F$  is the magnetic quantum number,  $\Delta_{D_1}$  and  $\Delta_{D_2}$  are the frequency differences from the two  $D$  lines,  $\Gamma = (\Gamma_{D_1} + \Gamma_{D_2})/2$ ,  $\omega = (\omega_{D_1} + 2\omega_{D_2})/3$  and  $P = \pm 1$  or  $0$  for optical  $\sigma^\pm$  or  $\pi$  polarisation. This periodic potential can be formed in 1, 2 or 3 dimensions, with various lattice structures and separations of potential minima (from  $\lambda/2$  upwards), by changing the configuration of the laser beams making up the lattice.

The density of atoms in a BEC can be made such that, when the atoms are adiabatically loaded into a periodic optical potential (which will have wells of volume  $(\lambda/2)^3$  or greater), each well will be loaded with at least one atom (over the spatial extent of the BEC). The temperature of the atoms will be such that they remain in the lowest quantum state of the individual wells, and near the ground state of the multi-well system (in a delocalised many-well wave function). The ultracold atoms in this system have two types of behaviour; they may tunnel between nearest-neighbour wells ( $J$  of Eqn. 2.4, equivalent to a kinetic energy term), and they feel s-wave ultracold elastic collisional interaction with other atoms in the same well ( $U$  of Eqn. 2.4, which can be considered

a type of potential energy term). If the atoms are cool enough, and the lattice potential high enough, other terms usually can be excluded as they correspond to a significantly higher energy or have rates much lower than the two dominant terms. Such a system is described by the Bose-Hubbard Hamiltonian of condensed matter physics [42]

$$H = -J \sum_{\langle i,j \rangle} \hat{a}_i^\dagger \hat{a}_j + \frac{U}{2} \sum_i \hat{n}_i(\hat{n}_i - 1) + \sum_i \epsilon_i \hat{n}_i \quad (2.4)$$

where  $J$  and  $U$  are the tunnelling and interaction parameters respectively,  $\epsilon_i$  is the energy offset of site  $i$ ,  $\hat{a}_i^\dagger$  is the creation operator for a particle in site  $i$ ,  $\hat{n}_i = \hat{a}_i^\dagger \hat{a}_i$ , and the bracket  $\langle i,j \rangle$  denotes a summation over nearest neighbours. This is the more general, inhomogeneous, version of the Bose-Hubbard Hamiltonian; the homogeneous version has  $\epsilon_i = 0$  for all  $i$ .

This well studied Bose-Hubbard Hamiltonian has a zero-temperature phase transition (see Fig. 8.1) between a delocalised atomic state, known as the superfluid phase, and a localised atomic state, known as the Mott insulator phase. A quantum phase transition such as this can typically occur only in strongly interacting quantum systems (in which the interaction terms are around the same order of magnitude as single-atom terms); the behaviour of such systems cannot simply be described by perturbative approaches. The Mott insulator phase transition was demonstrated experimentally a few years ago for ultracold atoms in an optical lattice [28]. The loss of long range phase coherence was measured by observing the momentum distribution of atoms released from the lattice, demonstrating a transition to a localised state; furthermore a gap was found to open up in the excitation spectrum (see Fig. 2.2).

## 2.2 Quantum simulation and quantum computation

The observation of the quantum phase transition of the homogeneous Bose-Hubbard Hamiltonian is only the first example of the strongly interacting quantum dynamics that can be investigated by these types of experiments. Looking at ultracold atoms in optical lattices in a more general way, it is possible to simulate a wide variety of strong interaction Hamiltonians, by exploiting the substantial degree of flexibility and control characteristic of ultracold atomic systems. The study of these dynamics has been

given the title of ‘quantum simulation’ to reflect the degree of control possible over the coherent quantum processes [44]. In this way, it is becoming possible to simulate a variety of systems of interest in condensed matter physics by constructing a similar Hamiltonian for ultracold atoms. Prospective systems of interest include: the Bose-Hubbard and Fermi-Hubbard models in 1, 2 and 3 dimensions, for a wide variety of lattice geometries [44, 28, 38, 88], quantum dynamics in a high effective magnetic field [43], and Bose and Anderson glasses in disordered potentials [19].

By using the high degree of control and long coherence times of systems of ultracold atoms, it is possible to investigate the properties of Hamiltonians that cannot be easily, or accurately, investigated any other way; quantum simulation potentially provides an intermediate step between theoretical studies and the reality of complex physical systems. Theoretical and computational work is limited by the massive size and complexity of the state vector needed to compute strongly interacting many-body quantum dynamics, has been discussed in Section 1; therefore theoretical modelling work has severe limitations when applied to certain phenomena in condensed matter physics. It is thought that the understanding of such systems will be increased by using ultracold atoms to simulate these interesting Hamiltonians. For example, probing the phase diagram of the two-dimensional Fermi-Hubbard model with ultracold atoms may shed light on the mechanism of high temperature superconductivity [10]. From a quantum information perspective, simulating these Hamiltonians using a quantum mechanical system is much more efficient than a simulation using ‘classical’ computer modelling.

The quantum simulation process can be subdivided into the operations of preparation, propagation, and observation. Preparation involves making a quantum starting state for the simulation; this can be thought of as the initialisation of the quantum data array. The starting state must be a predictable and reproducible, in order that it is almost identical for each run of the simulation. The propagation involves simulating the required Hamiltonian by the action of optical, magnetic and radio-frequency fields. The observation concerns the readout of the information contained within the final state of the system.

The preparation of the quantum starting state has been the aspect of quantum

simulation that has been most successfully demonstrated in experiments to date. A suitable starting state is typically taken to be a state in which there is precisely one atom at each site within a certain region of an optical lattice. This can be formed by going through the Mott insulator phase transition with an atomic sample of a certain density; however, the purity, or uniformity, of the starting state in current experiments [28] may not be as high as is desired for a quantum simulator [65, 80]. Novel methods which I have developed to increase the purity of these starting states will be discussed in Chapter 8.

The action of the required Hamiltonian for propagation of the wave function is the next aspect that must be addressed. To perform arbitrary quantum manipulations, one must control the atoms at each site separately. This is not easily achieved in current optical lattice experiments as the wells are too close to resolve (this is discussed below and in Section 4.3.1). Nevertheless, many Hamiltonians of interest can be simulated without individual site addressability [44]. For example, it is possible to address a certain subset of sites in the optical lattice by using a superposition of standing waves to make atoms in certain planes feel a different interaction from atoms in other regions of the lattice. Recently such manipulations were used to probe the dynamics of a lattice of double wells [2].

Observation, or readout, of the atomic states is the last stage of the simulation. In typical optical lattice experiments the separation between potential minima is around 300-400 nm ( $\lambda/2$  for the alkali D lines)<sup>3</sup>. Longer period lattices are formed when the laser beams intersect at an angle less than  $180^\circ$  (or use longer wavelengths, e.g. CO<sub>2</sub> lasers at  $10\mu\text{m}$ ), however if the wavelength of the lattice is larger than around 500-1000 nm (the exact value would vary depending on the experiment), coherent quantum dynamics across the lattice tend to break down, because effects due to loss of coherence would dominate the slow coherent inter-well tunnelling processes. Thus the observation of strongly interacting quantum states at a resolution of single wells and single atoms is difficult; the atoms will be typically separated by less than the Rayleigh limit at the D

---

<sup>3</sup>This could be decreased in the future by the use of a powerful laser at a shorter wavelength e.g. at 532 nm so  $\lambda/2 = 266$  nm.

resonances, even for lenses of very high numerical aperture ( $>0.5$ ). In current experiments only the overall properties of the quantum states are measured, typically by using the technique of time-of-flight imaging to determine the momentum distribution of the atoms (for example, see Fig. 2.2).

Taking the idea of simulation one step further, it is possible to perform arbitrary calculations using the quantum mechanical analogue of classical bits called qubits. There are a few ways that one can imagine implementing a qubit for neutral atoms in optical potentials: one way would be to have the qubit as two internal (e.g. hyperfine or magnetic) states of a single atom in a single well; another way would be to have an atom delocalised between two wells. It has been proven that an arbitrary quantum transformation on a qubit array can be decomposed into a succession of 1-qubit and 2-qubit manipulations [72]. A single qubit manipulation can be thought of as a site-specific internal rotation for the first scheme, or a tunnelling operation for the second scheme. Two qubit gates tend to be more complex, especially if the two qubits are distant from one another; one proposed scheme involves physically bringing the qubits together so that the atoms collide to accumulate a phase, conditional to their state, forming a ‘collisional gate’ [41]; other two qubit gate schemes rely on the coupling of dipole moments of atoms in excited Rydberg states [82], or coupling two atoms via single-photon interactions in optical cavities [13].

To achieve arbitrary quantum computation with ultracold atoms, there must be the ability to perform site-specific manipulations of individual potential wells, something that has not yet been achieved in optical lattice experiments.

## 2.3 Detecting signatures of strongly interacting quantum systems of ultracold atoms

### 2.3.1 Number squeezing and the Mott insulator transition

There have been a number of experiments that have looked into aspects of strongly interacting systems of ultracold atoms in optical potentials. All of these experiments used time-of-flight imaging of many thousands of atoms to extract the signature of the strongly interacting quantum dynamics.

Before describing these experiments it is worth considering what a strongly interacting system is, and how this can apply to an ultracold atomic system. The definition of a strongly interacting quantum system is that in which the energy of the interaction term or terms of the Hamiltonian (terms depending on relative co-ordinates) are larger than the single particle energy terms of the Hamiltonian (terms depending on single particle co-ordinates). One may think that it is strange that an ultracold gaseous atomic system can be strongly interacting at all; after all, in general, interactions between ultracold atoms must be kept weak to keep the ultracold gas from condensing into its true ground state, which is the solid metal. A resolution to this contradiction can be found by making the kinetic energy, and single particle potential energy terms, of the Hamiltonian very small. In an optical lattice, the kinetic terms are made small by inhibiting tunnelling between the wells; with a large energy gap to the first excited band and a cold atomic sample, the single particle dynamics is dominated by the low energy states of the narrow, flat ground state band<sup>4</sup>. In these circumstances, the collisional terms can dominate over the single particle terms, without the density of the gas becoming great enough that the interatomic binding processes (to first order, these are three-body recombination processes) can act to condense the gas within the time scale of the experiment. To summarise, it is possible to have a strongly interacting system with ultracold atoms as long as there is a separation of time scales  $\tau_{3\text{-body}} > t_{\text{exp}} > h/\langle E_k \rangle > h/\langle E_{\text{int}} \rangle$ , with the terms relating to the three-body losses, the time of the experiment, and the kinetic and interaction energies respectively.

---

<sup>4</sup>The single-particle potential energy terms can be made small by making sure the energy offset of each site is small; in experiments this is typically done by combining a weak magnetic potential trap with a broad envelope optical trap.

The superfluid to Mott insulator transition of the Bose-Hubbard model (Eqn. 2.4) has been the most studied system. The original observation was made by Greiner and co-workers [28], who found loss of long range atomic coherence as the lattice intensity was increased, and furthermore, evidence of low energy gaps in the excitation spectrum, indicative of a strongly interacting state (see Fig. 2.2). Another experiment by Orzel *et al.* [74] also probed an atomic state described by the Bose-Hubbard Hamiltonian and found evidence for number squeezed states of ultracold atoms i.e. a sub-Poissonian distribution of atoms in each well of the lattice which is caused by interatomic interactions. However they were not able to observe the Mott insulator transition itself as the number of atoms per well was much greater than one (see Section 8.2 for further details).

Following the initial observation of the Mott insulator transition in the three-dimensional optical lattice, a comparative study was done on the transition in one, two and three dimensions [53]. This was accomplished by using a three-dimensional optical lattice, while inhibiting tunnelling in the ‘unwanted’ directions by substantially increasing the lattice depth along those directions. The transition was probed by examining the excitation spectrum of the atomic sample; features dependent on the dimensionality of the dynamics were found.

### 2.3.2 Measurements of Mott insulator structure

The Mott insulator state in a lattice overlaid with a wide, weak harmonic potential has a characteristic shell structure [42]. The shell structure arise from competition between the interatomic repulsion and the weak harmonic potential; the atom number per site, rather than smoothly following the shape of the potential as in the superfluid, contains plateaus corresponding to specific Fock states  $\langle n \rangle = 1, 2$  etc.

Four experiments have been able to measure this feature in the number distribution of atoms across a harmonically confined lattice. Three of these used the shift in energy per atom  $(n - 1)U/2$  when  $n > 1$  atoms are present at a lattice site (Eqns. 2.4 and 8.2) to distinguish the different occupancies. One experiment [23] used spin changing collisions, controlled using on- and off-resonant microwave transitions, to selectively transfer atoms in double occupancy wells to different magnetic spin states, which then

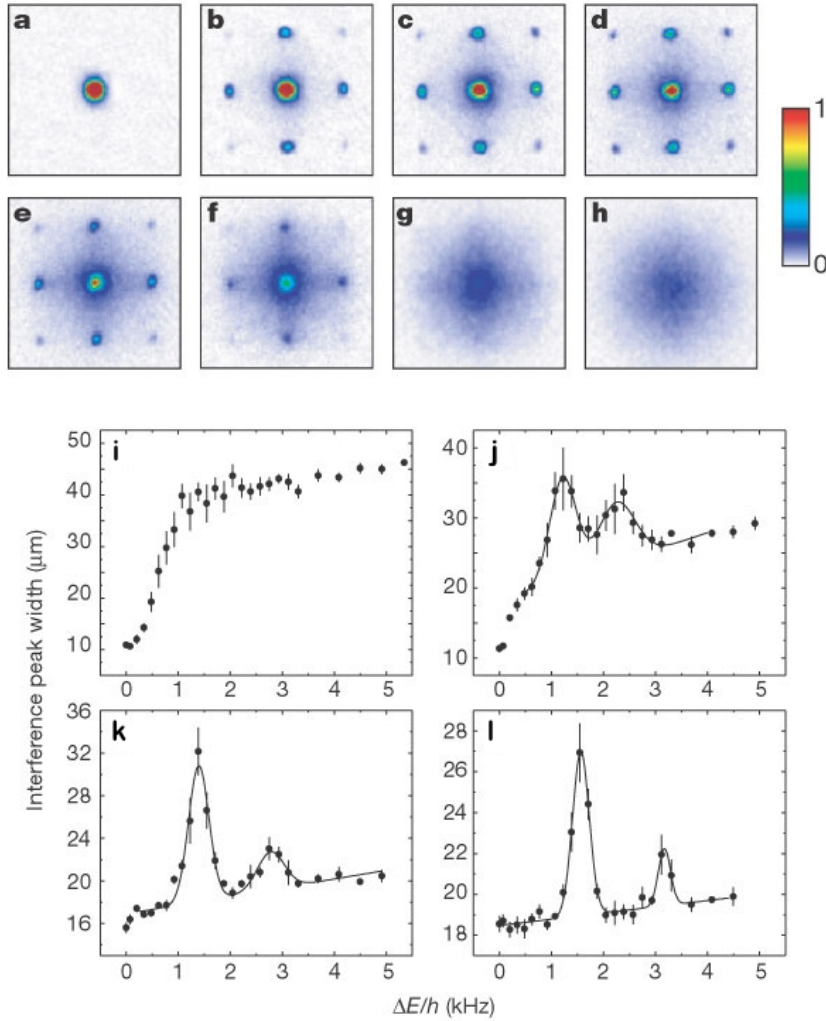


Figure 2.2: The observation of the transition from superfluid to a Mott insulator in a sample of ultracold atoms, from Greiner *et al.* [28]. Figures (a) to (h) show images of the interference pattern of atoms released from the optical lattice, with increasing lattice depth, from  $V_0 = 0$  in (a) to  $V_0 = 20E_r$  in (h). As the pictures are taken in time-of-flight, these effectively show the momentum distribution of the atoms in the lattice. The momentum wave functions are the Fourier transform of the spatial wave functions; therefore the side peaks in the momentum distribution are indicative of atomic wave functions delocalised over many lattice sites. These side peaks first appear as the weak lattice alters the wave function of the Bose-condensed atoms, but then disappear with further increases in lattice depth, indicating a transition to a regime where the atoms are localised in individual wells. Further evidence of the Mott insulator transition, demonstrating the role of collisional interactions, is given by the excitation spectrum in the Mott insulator state, which is given in Figs. (i) to (l), with the lattice depth increasing from  $V_0 = 10E_r$  in (i) to  $V_0 = 20E_r$  in (l). The excitation spectrum changes form, from a broad distribution at lower lattice depth, indicative of transitions within the lowest band of the superfluid regime, to a peaked distribution at higher lattice depth, indicative of the low energy gap structure due to collisional interactions in the Mott insulator spectrum. From Greiner *et al.* [28].

were separated by a magnetic field gradient using time-of-flight imaging. A different experiment [7] used resonant microwave transitions to transfer atoms from a specified Fock state into a different hyperfine level, which could be imaged separately. A third experiment [9] performed similar manipulations in a double well lattice (see Sect. 2.3.4). A fourth experiment was able to directly measure the flat-top density profile in a two dimensional Mott insulator state by absorption imaging [25]. The number and distribution of the wells of different occupancies broadly agreed with theoretical predictions.

All four of these experiments, although measuring properties of the number distribution, can only measure the distribution with a spatial resolution of a few micrometres, and are statistically averaged over many sites (thousands for the 3D lattices [23, 7, 9], and around 50 for the 2D lattice [25]).

### **2.3.3 Direct measurement of sub-Poissonian statistics**

Sub-Poissonian number statistics imply that collisional interactions are a factor in the number occupancy of a well or wells. Sub-Poissonian number statistics can be considered a weaker form of a Mott insulator; they are not necessarily a result of strongly dominating collisional dynamics, as in a Mott insulator, but of weaker collisional dynamics, such as is present in a BEC. After the first and somewhat ambiguous indirect observation of number squeezing in a lattice [74], a couple of experiments have demonstrated direct observation of sub-Poissonian statistics, for wells containing 100-200 atoms [11, 40]. However it becomes harder to achieve the phase transition to the Mott insulator state as the number of atoms per well increases (Eqn. 8.4).

### **2.3.4 A lattice of double wells**

In a recent experiment [58] a lattice with a double-well basis was set up in such a way that each double well could be merged into a single well. Atoms in each sublattice have the property that their internal state can be manipulated separately from the internal state of atoms on the other sublattice by different potential offsets. With a single atom in each well of both sublattices, the atoms in the two sublattices are transferred to different internal states, and then brought together into different vibrational levels of the combined

well. Controlled spin-exchange collisions, which caused the internal state of the atoms to oscillate, were observed by an analysis of the momentum distribution of the atoms. Such spin-exchange collisions can be used to implement quantum information protocols [35] for quantum simulation or quantum computation.

### **2.3.5 Strong interactions at low density in one dimensional systems**

Another experiment in which the signature of a strongly interacting quantum system was observed [76] was, in contrast to the experiments described above, conducted in the regime where the average number of atoms per site was much less than one. In the Tonks-Girardeau regime of a one-dimensional gas, the atoms can freely tunnel to an empty well, but encounter an energy barrier  $U$  for tunnelling to an already occupied site. When this energy barrier is large compared to the kinetic energy of the atoms  $J$  the system enters the Tonks-Girardeau regime, in which atoms cannot occupy the same well, and so cannot pass each other along the string of coupled wells. This causes the bosonic particles to have quasi-fermionic properties; the increased localisation was measured in the momentum distribution of the released atoms. This situation is unique to one-dimensional systems, as similar localisation is not possible in higher dimensional systems.

## **2.4 The observation of low numbers of ultracold atoms using fluorescent imaging**

This section and the next summarise recent published experimental work concerned with probing of atomic samples at the level of single atoms<sup>5</sup>.

Two experiments have particular relevance to the work set out in this thesis.

### **2.4.1 Fluorescent imaging in a three-dimensional optical lattice of period 5 microns**

The team of Weiss at Pennsylvania State University [71] imaged individual atoms in a three-dimensional array, with lattice sites spaced by around  $5\mu\text{m}$  (as shown in Fig. 2.3). They used polarisation gradient cooling to suppress the recoil heating of the atoms

---

<sup>5</sup>There are other groups moving in this direction; however only pre-prints placed on the arXiv up to September 2009 can be covered.

during the imaging process. The hopping rate of atoms between wells was less than  $0.01 \text{ s}^{-1}$ , which is slow enough for each atom to scatter many photons, resulting in a good signal for each atom. Individual planes of the lattice (separated by  $5 \mu\text{m}$ ) were distinguished by using a high numerical aperture objective lens with a short Rayleigh length so that atoms in the other planes of the lattice were not in focus.

These images do not show the initial distribution of atoms in the lattice, which was a thermal population of around 6 atoms per lattice site. Only one atom (or no atoms) could be detected at each lattice site because of strong light-assisted collisional loss processes (see Section 4.3.3), which significantly change the atomic distribution. The lattice period of  $5 \mu\text{m}$  is around an order of magnitude greater than what would be needed to observe strongly interacting quantum dynamics (see Sections 4.3.1 and 8.4). My own proposal, described in Chapters 4 to 7, shares the feature of using polarisation gradient cooling of atoms trapped in a lattice to increase the signal-to-noise ratio of the fluorescent signal from individual atoms.

A similar experiment has been carried out with a 1D lattice [48] with a site separation of 430 nm. The dimensionality of the lattice and the rather diffuse sample (average number of per well much less than 1) meant that it was possible, with some finite probability, to infer atomic separations which were under the diffraction limit of the imaging system.

#### **2.4.2 Fluorescent imaging in a two-dimensional optical lattice of period 640 nanometres**

The results of a second relevant experiment [4] have emerged as a pre-print as this thesis was being written (August 2009). The team of Greiner at Harvard have carried out a similar experiment to that of the group of Weiss at Penn State [71], but with a much smaller lattice period. The significance of this new work is that it has the potential to see strongly interacting quantum physics in ultracold systems at the level of single atoms, although this has not yet been observed. Despite the excellent progress that has been made by this research, the technique I propose has significant advantages for the study of strongly interacting physics in optical lattices; a detailed comparison of the two

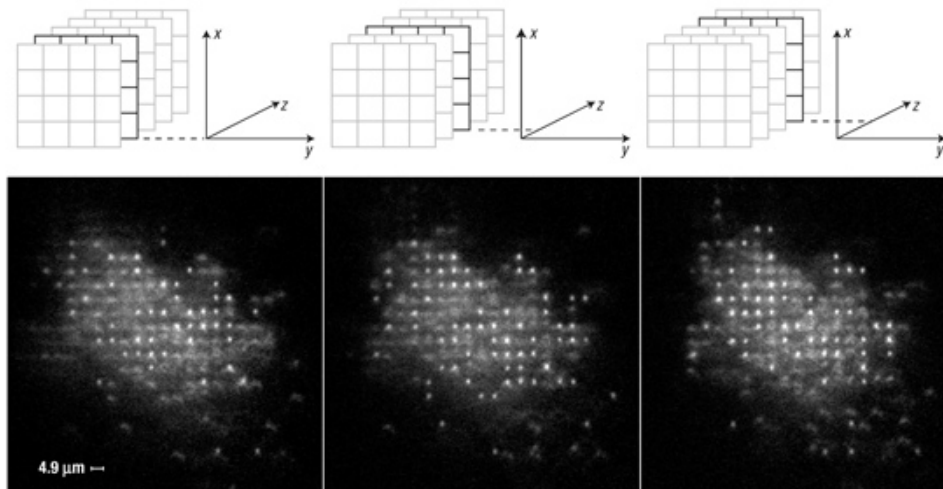


Figure 2.3: These pictures show single atoms imaged in a  $5\ \mu\text{m}$  period optical lattice. The large period of the lattice allows each site to be resolved. Atoms in other layers of the lattice (displaced along the  $z$  axis) are out of focus due to the short depth of field of the imaging lens. The three images show different layers of the lattice, taken by translating the lens along the  $z$ -axis. Polarisation gradient cooling was used to cool the atoms during the measurement process to allow a good signal-to-noise ratio in the images. The atomic distribution in this lattice initially had many atoms in each well of the lattice. Upon measurement, light-assisted collisional processes quickly reduced the number of atoms per well to one (for an odd number of initial atoms) or zero (for an even number of initial atoms); due to this process the images are not an accurate reflection of the initial atomic distribution in the lattice. From Nelson *et al.* [71].

methods is given in Section 7.5.

The major design feature of the experiment at Harvard which enabled spatially resolved measurements of sites of the  $640\ \text{nm}$  period lattice is the use of a very high numerical aperture lens system ( $\text{NA} \sim 0.8$ ), giving a resolution of around  $600\ \text{nm}$  (Eqn. 4.1). The lens system has elements both inside and outside the vacuum. The atoms are confined to a 2D sheet positioned  $1.5\text{--}3\ \mu\text{m}$  from the ultra-flat surface of the lens mounted within the vacuum—the close proximity of a high refractive index material gives a large solid angle for collection of fluorescent light that can be captured is increased, thus increasing the overall numerical aperture of the lens system.

They created a 2D optical lattice using a diffractive optical element to split incoming laser light into beams which are recombined at the position of the atoms (equivalent to projecting a filtered image of the phase grating onto the atoms). The same high numerical aperture lens as is used to view the atoms as to produce the optical lattice,

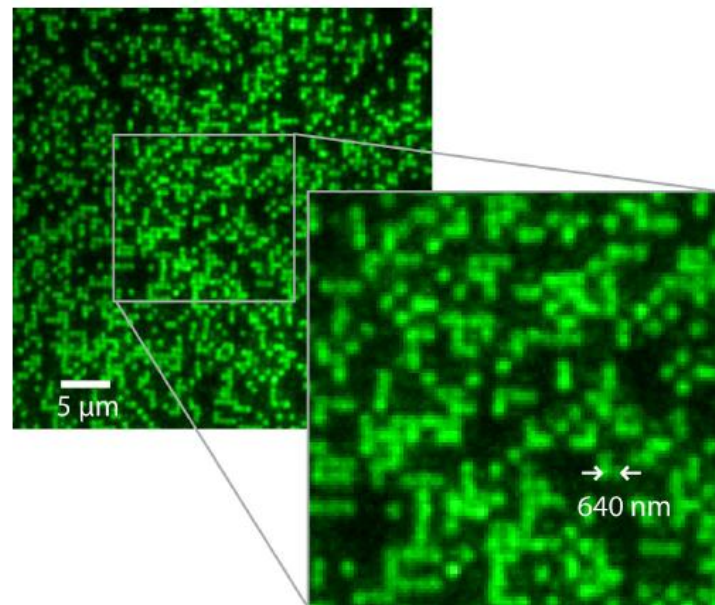


Figure 2.4: Single atoms imaged in a two-dimensional optical lattice. The lattice period is 640 nm, and the resolution of the microscope objective around 600 nm. The observed distribution is the parity of the true occupancy at each site, as light-assisted collisions remove atoms pairwise. From Bakr *et al.* [4].

which is of 640 nm period. A key feature of this method of making an optical lattice is the ability to form a lattice with the same period and phase for different wavelengths of incoming light. This allows the atoms to be transferred smoothly between off-resonant and near-resonant lattices, appropriate for quantum dynamics and probing respectively.

The atoms are cooled by polarisation gradient cooling while they are being imaged. However, in contrast to Reference [71], the atoms are confined to a region much smaller than an optical wavelength, which changes the polarisation gradient cooling dynamics (this is discussed in Sections 5.1 and 5.2).

The result is that atoms can be resolved at individual sites of the optical lattice (Fig. 2.4). There are various issues which are still present in this experiment; the technique I propose should overcome these.

- As with Reference [71], the effect of light-assisted collisions still dominate the observed atomic distribution; as acknowledged in the paper, it is the *parity* of the atom distribution distribution which is measured, rather than the true atomic distribution.

- The lattice period of 640 nm is not the optimal  $\lambda/2$ , which for example is around 380 nm for rubidium. The strength of the interaction, with the lattice depth set so that the atoms can still tunnel between the wells, increases markedly as the lattice period is decreased. The strongly interacting quantum phenomena of interest will become easier to observe, and purer, if the lattice period can be decreased; see Sections 4.3.1 and 8.4.
- The technique as described is only appropriate for 1D and 2D physics, as it is reliant on having only a single layer of atoms.

The technique described in later chapters overcomes all of these limitations. However, with the holographic lattice generation it is easy to change the lattice geometry and site connectivity, whereas changing the lattice geometry is possible in my method but not as straightforward.

### 2.4.3 Fluorescent imaging of a single dipole trap immersed in a MOT

Another set of experiments use a different approach to look at single atoms. Rather than loading many thousands of cold atoms into an optical lattice, they use one or more very deep, highly focussed, dipole traps to load a few atoms directly from a magneto-optical trap [87, 101, 56]. If there are no interatomic interactions, the number of atoms in the trap would be expected to conform to Poissonian statistics. However a ‘collisional blockade’ mechanism gives sub-Poissonian loading statistics: when two or more atoms are in a trap, there is a large 2-body light-assisted collisional loss rate which quickly gets rid of atoms in a pairwise process (see Section 4.3.3). To deterministically prepare a single atom per trap, however, a real-time feedback and control process must be implemented, due to the statistical nature of the atom capture process. Such control has been demonstrated to prepare a string of trapped single atoms [68]. With these types of experiments, the atoms are in highly excited vibrational states in the traps and would need to be cooled before strong coherent collisional interactions can be obtained<sup>6</sup>. Furthermore,

---

<sup>6</sup>Certain types of coherent quantum interatomic interactions are possible with a less stringent cooling requirement, for example by using Rydberg states or an optical cavity.

due to the statistical nature of the preparation process, these experiments are limited to a few atoms at a time, and are not suitable for filling an extended optical lattice potential.

## **2.5 Other techniques used to observe low numbers of ultracold atoms**

### **Optical cavity detection**

Single atoms can be detected as they traverse a mode of a high-finesse cavity. The resonance properties of the cavity change as the atom traverses due to the difference in permittivity between vacuum and the atom, which is most pronounced near optical resonances. This has been used in an experiment [95] to detect correlations between atoms of a coherent matter beam sourced from a BEC. This method is most applicable to one-dimensional distributions in time-of-flight imaging.

### **Metastable helium incident on a microchannel plate**

Correlations of atoms within a BEC of metastable helium ( $\text{He}^*$ ) were measured by letting the atoms fall onto a microchannel plate detector (i.e. time-of-flight imaging) [85, 46]. Upon contact with the plate, around 20 eV of energy was released from each atom; the signal from each atom could be detected with a horizontal positional sensitivity of around  $250 \mu\text{m}$ .

### **Electron beam ionisation and ion detection**

A recent experiment [26] uses an electron microscope to image atoms within a one-dimensional optical lattice. Electrons can have a much smaller de Broigle wavelength than optical photons, so the resolution of such images is under the optical resolution limit, at around 100-150 nm. The electrons ionise the ultracold atoms in-situ; the ions are subsequently collected and focussed, using ion optics, then detected. Individual sites of the optical lattice could be seen in summed images from a set of runs.

### **Photoionisation and ion detection**

In a similar way to electron beam ionisation, atoms may be photoionised via multiphoton processes, and the ions produced are subsequently detected [92, 54]; however the optical mode of ionisation limits the resolution.

### **2.6 Summary**

Although the research described in this section has demonstrated the preparation and probing of atomic samples at the resolution of single atoms, strongly interacting many-body quantum dynamics are yet to be observed at this level of detail. Whilst a recent experiment is described which is potentially capable of carrying out such investigations, the design of this experiment still has limitations, in particular in the inability to measure the true atomic distribution in the lattice.

The research I have carried out during my DPhil aims to combine the capabilities that the above experiments have demonstrated: to observe atoms individually, but within the quantum states of a strongly interacting, many-body system. It is surely in the combination of these capabilities that the future of quantum simulation, and perhaps even quantum computation, lies.

---

## CONSTRUCTING APPARATUS FOR BOSE-EINSTEIN CONDENSATION AND REACHING QUANTUM DEGENERACY

The work which is described in this section is somewhat independent of the rest of the work in this thesis, for the reasons outlined in Section 1.1. The work described in this chapter was performed in collaboration with the DPhil student Andrian Harsono (and later with Ben Fletcher). They were able to continue this work in my absence; both have now submitted their theses. The majority of their theses described how the apparatus was built and optimised. As this material has already been written up in detail, this chapter will only outline the work we performed together; for the details I refer the interested reader to the theses of my co-workers.

### 3.1 Cooling requirements for quantum degeneracy

A Bose-Einstein Condensate is the low-temperature limit of the Bose-Einstein distribution of number-conserved bosons

$$n(\epsilon) = \frac{1}{e^{\frac{\epsilon-\mu}{k_B T}} - 1} . \quad (3.1)$$

The chemical potential  $\mu$  is the Lagrange multiplier which ensures number conservation. At a given temperature, the addition of more particles will force  $\mu$  to increase. However  $\mu$  can never be larger than the energy of the ground state  $\epsilon_0$  (otherwise the occupancy

of the ground state becomes negative and so unphysical). Depending on the form of the confining potential, and at very low temperatures, the sum over the excited state occupancies may approach a fixed value for  $\mu \rightarrow \epsilon_0$ . In this situation, the only possible place for extra atoms is in the ground state, which therefore can have a very large occupancy of order the number of atoms in the distribution. This macroscopic occupation of the ground state is called a Bose-Einstein Condensate.

The temperature needed to make neutral gaseous bosonic atoms condense is very low; in a three-dimensional harmonic potential, the transition temperature can be found to be ([77] p21)

$$T_c = \frac{\hbar}{k_B} \left( \frac{\omega_1 \omega_2 \omega_3 N}{\zeta(3)} \right)^{\frac{1}{3}} \quad (3.2)$$

in which where  $\zeta(\alpha) = \sum_{n=1}^{\infty} n^{-\alpha}$  is the Riemann zeta function. For neutral atoms in magnetic potentials quantum degeneracy is achieved at temperatures of a few microkelvin or below. It can be seen that atoms must be cooled dramatically from room temperature to achieve condensation.

This cooling is necessarily a multi-stage process, with each stage appropriate to a certain temperature spread. In the experiment described in this chapter there are three major stages. Firstly, magneto-optical confinement and cooling captures hot neutral atoms (above room temperature) released from a rubidium getter. Once enough atoms have been collected in the MOT, polarisation gradient cooling is applied using the optical molasses technique. Finally the atoms are isolated from resonant light, and evaporative cooling in a magnetic trap.

I will omit from this thesis the principles and theoretical details of these cooling processes (although polarisation gradient cooling is described in another context in Chapter 5), as this material is fairly standard and is well covered in many sources (for example Metcalf and van der Straten [67]). This chapter shall instead review the technical details of our implementation.

## 3.2 Apparatus

### 3.2.1 The magneto-optical trap

We use two magneto-optical traps (MOTs) in our apparatus, with each MOT in a separate section of the vacuum system. These two sections are connected by hole which is small enough that each region can be maintained at a different background rubidium pressure. This allows relatively fast capture of atoms into the first MOT, which is of pyramidal design and is situated in the higher pressure ( $10^{-8}$  Torr) section; the MOT collects hot rubidium atoms released when nearby rubidium getters are heated. The atoms are captured and pre-cooled, then are continuously channelled, by radiation pressure from this first MOT, through the hole joining the two sections of the vacuum system and into the capture region of the second MOT. The second section of the vacuum system is maintained at a lower pressure ( $10^{-10}$  Torr). The atoms held in this section have a much lower loss rate due to collisions with room-temperature background gas atoms; this is where the experiments are carried out. The isotope  $^{87}\text{Rb}$  is used in our work.

### 3.2.2 The magnetic trap

The magnetic trap we constructed is of ‘baseball’ design. The baseball trap is a modified Ioffe-Prichard trap in which the pinch coils and Ioffe bars are combined into a single baseball coil (see Fig. 3.1). The magnetic field at the trap minimum is high for the bare baseball trap (over 100 Gauss). This corresponds to a high Ioffe-Prichard bias field, which means that the resultant trap is rather loose. Higher trap frequencies are required for efficient rethermalisation in the evaporative cooling stage. Therefore in this stage of the experiment the bias field needs to be reduced to a few Gauss, in our case by current flowing in additional coils called bias coils. The bias and baseball coils were designed so that the two fields approximately cancel at the trap centre when the same current flows in both coils. This allows the coils to be powered in series, greatly reducing the heating effects from noise fluctuations in the current, due to the near cancelling of common mode fluctuations.

### 3.2.3 The laser beams

Sub-Doppler spectroscopy is used to lock the lasers. The  $D_2$  transition of  $^{87}\text{Rb}$  in vapour cells is probed in a typical pump-probe configuration; an electronic feedback system acts to stabilise the laser frequency (we lock to the peak of the transition). Once locked to the transition, a succession of acousto-optic modulators gives independent control over the frequency detuning and timing of the cooling light to both MOTs and generates the required frequencies for optical pumping and probing light. The original ‘master’ laser is now amplified by injection into two ‘slave’ lasers, with the output of each carried by optical fibre to the MOTs.

A second ‘repumping’ laser is also similarly generated and stabilised. The frequency of this laser is set so that it can optically pump atoms from the  $F = 1$  to the  $F = 2$  hyperfine levels; this is necessary to rectify small but significant leakage from the  $F = 2$  state due to excitation of the excited  $F' = 2$  and  $F' = 1$  levels, with subsequent decay to the lower hyperfine level  $F = 1$ .

Optical pumping light, generated from the master laser, is used to transfer the atoms into the  $|F = 1, m_F = -1\rangle$  state immediately prior to the loading into the magnetic trap. They are pumped to the lower hyperfine level with a preferred orientation, as inelastic collisional loss processes are slower in the lower hyperfine level and when the atoms share orientation. The same optical path is used for the probing light (see Fig. 3.2). Both fluorescent and absorption imaging diagnostics are used for probing the atomic sample along two separate directions. The apparatus was designed to give a large amount of optical access, in order that a high numerical aperture lens can be mounted near to the atoms; this lens can be used for high-resolution imaging and dipole trapping (using additional laser beams).

### 3.2.4 The cooling sequence

The science MOT, in the lower pressure section of the vacuum system, was loaded with atoms from the pyramid MOT, situated in the higher pressure section. After the number of atoms in the science MOT reached a certain value (around  $5 \times 10^8$ ), the pyramid MOT was shut off. A CMOT (compressed MOT) stage was used to increase the density of the

atomic sample, by using a higher magnetic field gradient and larger frequency detuning of the cooling beams. The magnetic field was then shut off, and optical molasses were used to cool the atoms using polarisation gradient processes for around ten milliseconds.

Immediately after the molasses stage, the atoms were optically pumped into the lower hyperfine level, and were quickly caught by a weak magnetic trap whose potential was matched to the temperature and size of the atomic cloud in order to minimise loss of phase-space density. All laser beams were shut off, and the magnetic trap was tightened in order to promote rethermalisation in the subsequent evaporation. Evaporation was performed by selectively transferring higher energy atoms, using a radio-frequency transition, to an untrapped state. This process of removal of the higher energy atoms, together with continuous rethermalisation, was enough to bring the remaining atoms into a state of quantum degeneracy.

### 3.3 Reaching quantum degeneracy

After the apparatus was built there was a substantial amount optimising and troubleshooting to be done before the apparatus before we reached the nanokelvin temperatures needed to reach quantum degeneracy. Some of the many facets of the apparatus and the experimental sequence which had to be investigated and optimised before Bose-Einstein condensation was possible are recorded here for future reference.

The stability of the laser lock, for both the cooling and repumping lasers, was critical to the success of the magneto-optic trapping, optical molasses and probing stages of the experiment. Many different considerations go into achieving the most stable lock, as summarised here. The intensities of the pump and probe light used in the sub-Doppler laser locking apparatus need to be optimised to produce the narrowest and sharpest spectrographic signal possible, as this directly translates into the effectiveness of the electronic feedback. This may be further optimised by changing the temperature, and so and vapour pressure, of the rubidium cell. The suppression of any reflections back into the laser diode chips is vital to avoid competition between optical modes; this suppression is largely performed by the optical isolators (see Fig. 3.2). On the electronic side, the properties of the feedback photodiode should be chosen to maximise the signal-

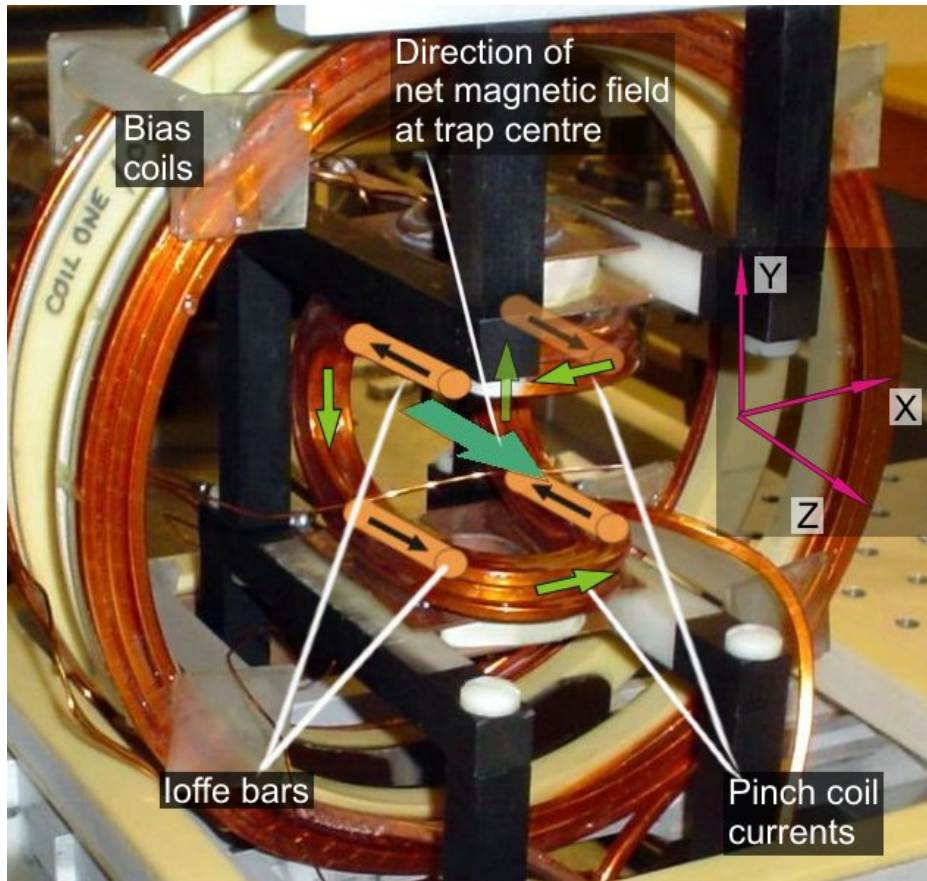


Figure 3.1: The coils of the magnetic trap, showing the relation between the baseball and Ioffe-Prichard traps. The baseball coil, named as the shape resembles the seams on a baseball, can provide all the magnetic field gradients needed for confinement of ultracold atoms. Near the centre of the trap, the magnetic fields  $B_x$  and  $B_y$  take the form  $B_x(x) = B'x$  and  $B_y(y) = -B'y$ ; this is effectively the field generated by the Ioffe bars marked in orange [52]. The currents depicted by the light green arrows are equivalent to the pinch coil currents of the Ioffe-Prichard configuration. At the trap centre, they result in a large bias field (marked by the large green arrow) plus a smaller quadratic term:  $B_z(z) = B_0 + B''z^2$ . The resultant magnetic potential has a minimum at the trap centre; with a large bias field, this minimum is broad (see Sect. 3.2.2). To achieve tight confinement, a requirement for more efficient evaporation, the bias field generated by the baseball coil is almost cancelled out using additional bias coils, which are the large circular coils shown in the picture. These produce a uniform field in the centre of the trap which opposes the baseball bias field  $B_0$ . The coils used to generate the magnetic quadrupole field for the MOT are visible sandwiched between copper sheets above and below the baseball coil.

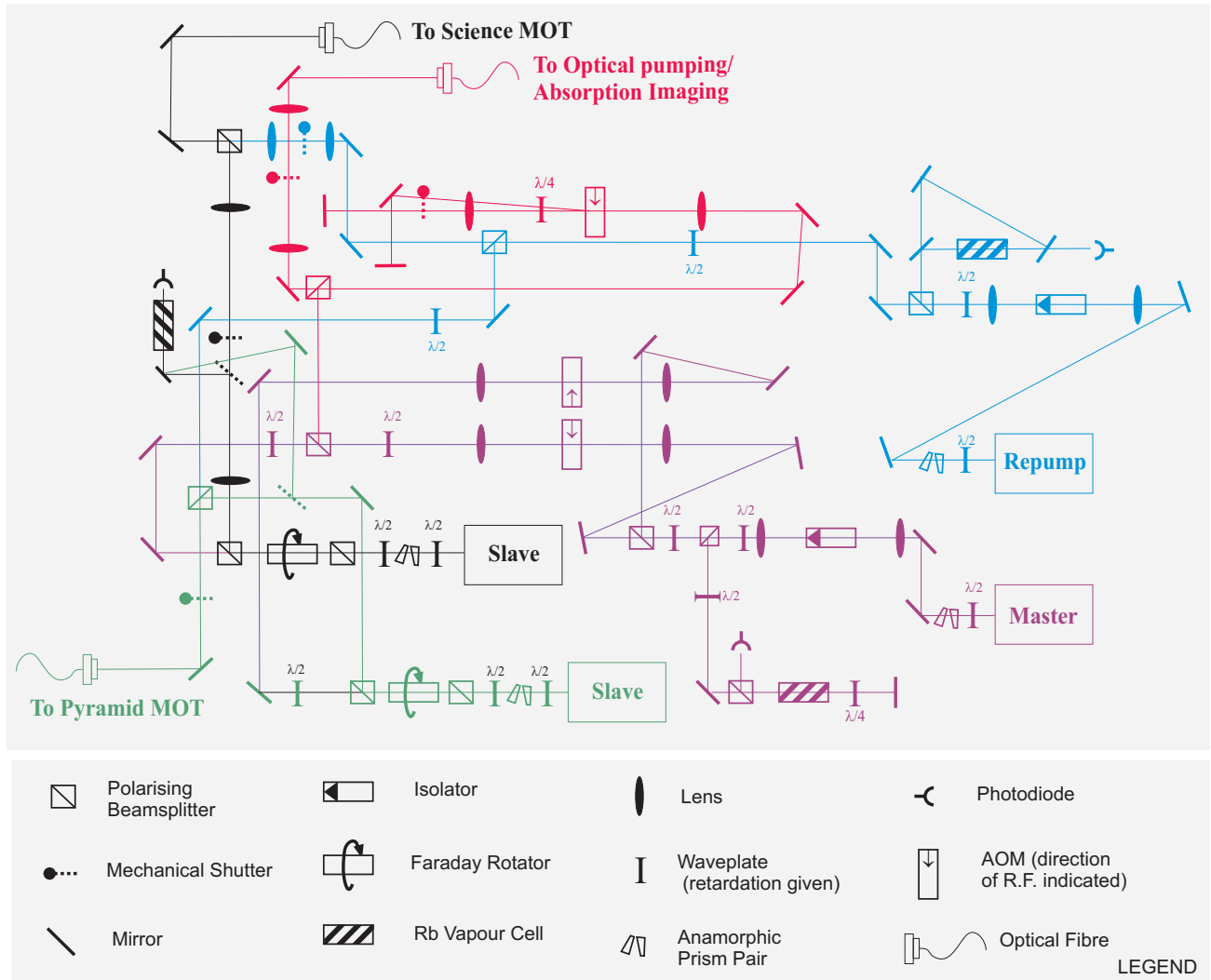


Figure 3.2: A schematic of the optical bench on which the cooling, probing, and optical pumping beams were generated. We locked the master cooling (purple) and the repumping (blue) lasers on sub-Doppler features of the spectra of two rubidium vapour cells. The master laser, after passing through an acousto-optic modulator (AOM), was injected into the slave lasers (black and green) in order to generate enough optical power for both MOTs. A small admixture of ‘repumping’ light was added to the cooling light, to pump stray  $F = 1$  atoms in the two MOTs back into the  $F = 2$  cooling state. The master laser was also used to generate probing light for absorption imaging (red). With the acousto-optic modulators tuned to a frequency different from that used for the probing light, the same path was also used for optical pumping light, which optically pumped atoms from the  $F = 2$  level to the  $F = 1$  level prior to capture by the magnetic trap.

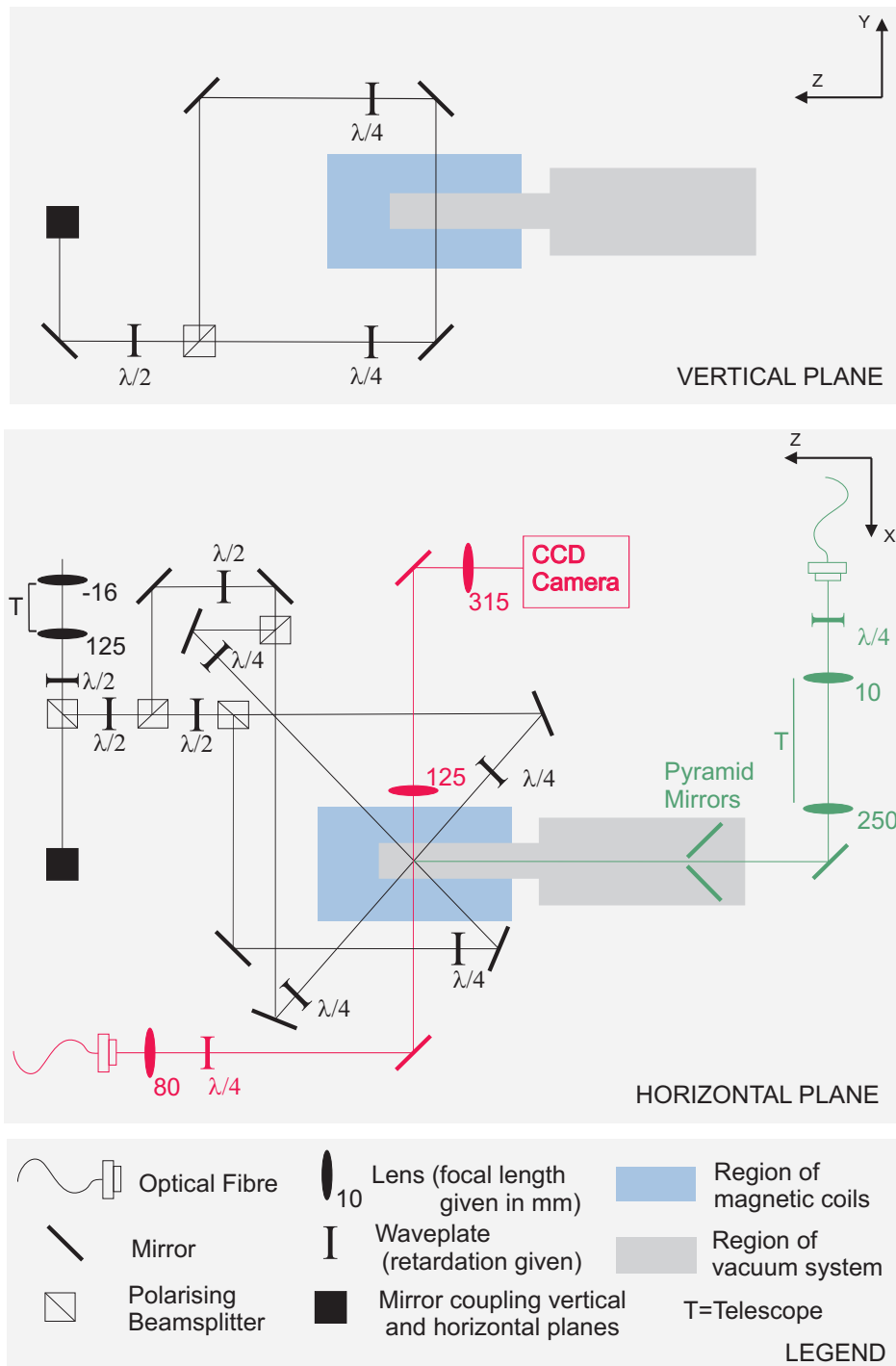


Figure 3.3: A schematic of the optical layout around the magnetic trap and vacuum system, as used to produce and probe BECs. The black lines indicate the laser beams and optics used to form the science MOT, by the use of six counter-propagating laser beams. The pyramid MOT is formed by a single wide cooling beam incident to the pyramid retro-reflector; this is indicated by the green beam and optics. The red line indicates the beam used for optical pumping, and for absorption and fluorescent imaging of the atomic distribution.

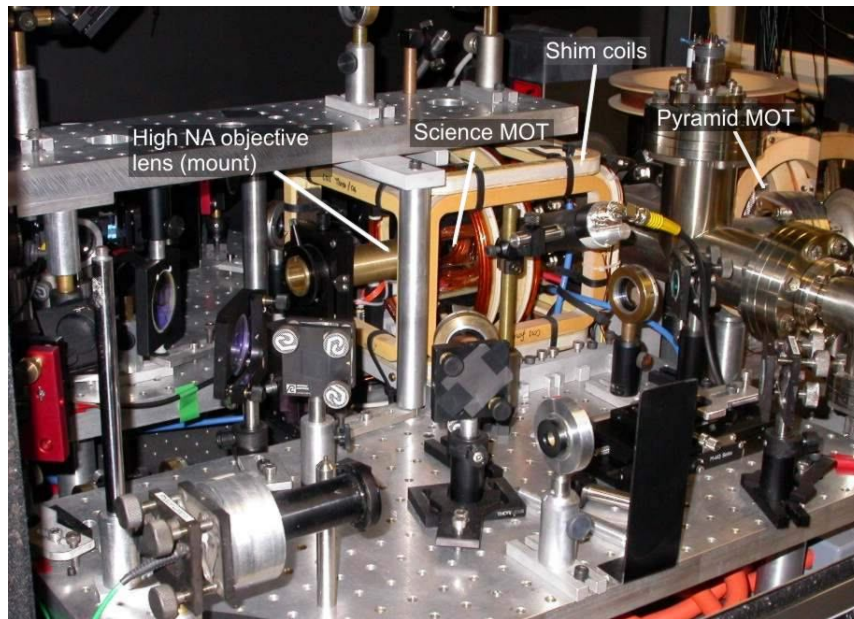


Figure 3.4: A photograph of the apparatus surrounding the vacuum cell which contains the BEC. The magnetic coils, optics, and vacuum system (in the upper right hand portion of the picture) are visible. The shim coils (clad in yellow) are used to cancel out stray magnetic fields and to provide small bias fields during various stages of the experimental sequence. The high numerical aperture (NA) lens is used for fluorescent imaging and dipole trapping.

to-noise ratio and response time. The parameters of the amplifier and the lock-in circuits of the phase-sensitive detector need to be adjusted to optimise the frequency stability of the laser. The acoustical and vibrational environment of the extended laser cavity must also be kept as noise-free as possible in order to that the laser lock remained stable. After these the laser lock was optimised, the measured frequency fluctuations were well under a megahertz<sup>1</sup>, with the laser staying locked to the transition for many hours before the lock needed to be reset.

The stability of the current flowing in the magnetic coils is also a major consideration; current fluctuations are a major source of heating of magnetically confined atoms. The heating can be suppressed by keeping the coils in series, as described above, driven by a highly stable current source. For our experiment a custom-built high-current (280 A) feedback stabilising circuit was used; closed circuit Hall probes were used as the sensors, and banks of metal oxide semiconductor field effect transistors (MOSFETs)

<sup>1</sup>By way of comparison, the  $D_2$  rubidium line width is 6 MHz.

were used as the actuators. Once the parameters of the feedback circuit were optimised the measured current stability was below  $10^{-5}$ .

A considerable part of our time was spent optimising the alignment and powers of the laser beams, for each of the cooling, repumping, optical pumping and probing beams; for example, the efficiency of the polarisation gradient cooling in the molasses stage was particularly sensitive to beam misalignment and imbalance (as well as any residual, stray magnetic fields). Methods were developed to achieve this alignment most efficiently.

Finally, the strengths, tunings and timings of the magnetic fields, lasers, and radio-frequency fields needed to be optimised for each stage of the experiment. This was typically done using measurements of the phase space density of a cold atom cloud, probed at the end of the experimental sequence, as each of the many parameters used throughout the sequence were varied. Some parameters needed to be optimised to different values at different stages of the experiment.

After optimisation of the experimental sequence we were able to reach quantum degeneracy. Quantum degeneracy was confirmed by measurements of the density and temperature of the final atomic sample (see Figs. 3.5 and 3.6) and by the coherent nature of the atomic dynamics in subsequent experiments.

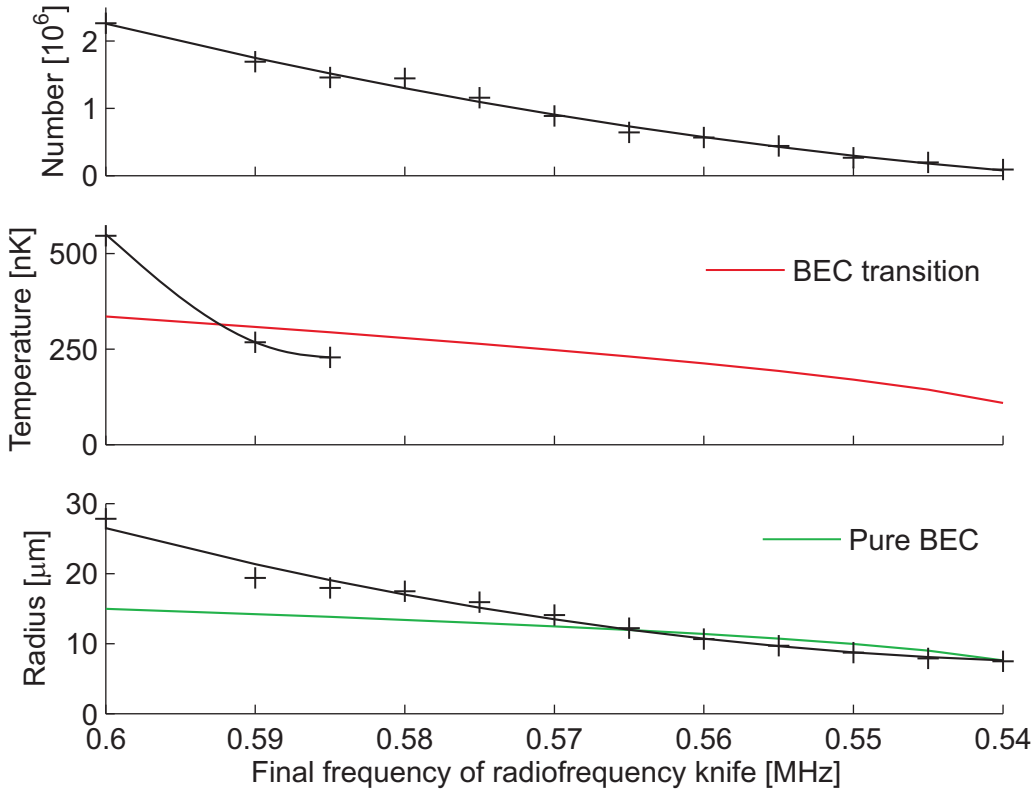
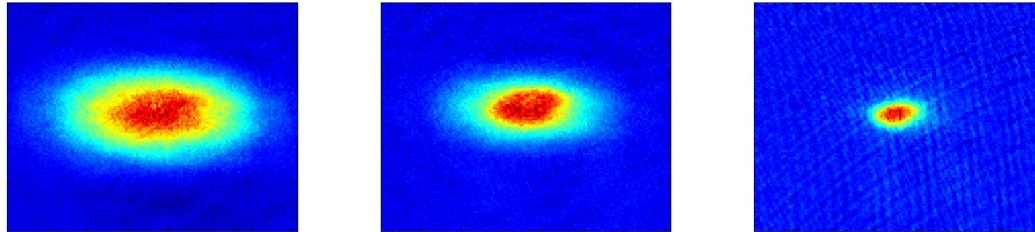


Figure 3.5: The formation of a Bose-Einstein Condensate. It is possible to assess the degree of quantum degeneracy present in the sample using measurements of the density and temperature of the ultracold atoms. These data are derived from absorption images of cold atomic clouds such as in Figure 3.6; images are taken after 18 ms of ballistic expansion from the magnetic trap. Each data point in the above graphs is taken on a separate, consecutive run of the experiment. The number of atoms in the sample (top graph) can be estimated by the total absorption cross section of the atomic cloud. The temperature of the sample (middle graph) can be measured from the rate of expansion of the cloud; this measure becomes inaccurate once the cloud becomes degenerate, so only the first few points are shown. The radius, as plotted (bottom graph), is the geometrical mean  $(r_1 r_2 r_3)^{\frac{1}{3}}$  of the inferred cloud radii in the magnetic trap. It is possible to predict both the BEC transition temperature, and the spatial extent of a pure BEC, for a given number of atoms in the atomic sample, using known parameters of the magnetic trap; these are plotted against the measured quantities. As the final frequency of the radio-frequency evaporation is lowered, it can be seen that the cloud temperature falls below the transition temperature, after which the sample composition will be a mixture of superfluid and thermal components. As the final RF frequency is lowered further, the thermal component is preferentially evaporated, and the spatial extent of the cloud approaches that of a pure BEC. In this data set there are 1.5-2 million atoms at the BEC transition point, and 500,000 atoms in the pure BEC.



(a) Thermal Cloud (0.60 MHz) (b) BEC & Thermal Cloud (0.575 MHz) (c) Pure BEC (0.545 MHz)

Figure 3.6: The phase transition to BEC. Figures (a) to (c) show absorption images from different runs of the experiment. The images have been taken after evaporative cooling to different depths. Red regions contain the most atoms; dark blue regions the least. These images are taken after 18 ms of free expansion. From left to right, the spatial size of the atom cloud becomes sharply smaller as the frequency of radio-frequency (RF) evaporation is lowered; however, the central column density of the sample does not decrease. For such a cold cloud, this behaviour is indicative of a phase transition to BEC; this is confirmed by more detailed calculations. These images are part of the data set of Fig. 3.5.

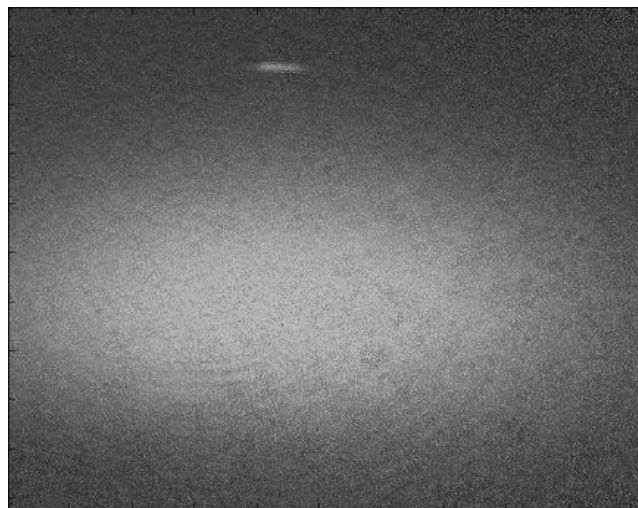


Figure 3.7: Absorption image from our experiment of atoms loaded into a highly focused laser dipole trap. The atomic sample trapped at the focus of the laser beam is shown as the small light region in the upper portion of the picture. The larger light region shows the remainder of the atoms, which are falling freely away under gravity.

# **A NOVEL TECHNIQUE TO PROBE STRONGLY INTERACTING ULTRACOLD ATOMIC SYSTEMS AT HIGH SPATIAL AND SINGLE ATOM RESOLUTION**

This chapter outlines the accordion and imaging lattice techniques. These techniques are designed to probe ultracold atomic samples at half-wavelength, single atom resolution. These techniques will be modelled and further developed in subsequent chapters.

## **4.1 The criteria for observation of individual atoms within a periodic optical potential**

Direct mapping of the distribution of ultracold atoms within an optical lattice, to probe strongly interacting quantum dynamics in detail, requires that a number of basic criteria are met:

1. The detected signal from single atoms must be sufficient to be distinguishable from noise.
2. The signal from each individual lattice site must be resolvable.
3. Every lattice site within a certain volume should be detectable.
4. The atoms must stay at the original lattice site during the measurement process.
5. The detection efficiency for each atom must be close to 100%.

Only when all of these criteria are met can an accurate reconstruction be made of the spatial distribution of atoms in strongly interacting quantum systems in periodic potentials.

## **4.2 Comparison of techniques**

This section will review existing single atom techniques, which have been described in Section 2.4, in terms of these criteria.

### **Absorption imaging**

Absorption and fluorescent imaging use resonant laser light to measure the spatial distribution of an atomic sample. Absorption imaging measures the decrease in the intensity of the laser light as it traverses the cloud; the profile of the atomic sample is imprinted as a shadow. The great majority of ultracold atom experiments use absorption imaging, as the signal-to-noise ratio is better than for fluorescent imaging of large atoms clouds; this is because every scattered photon counts towards the total signal. However, for low atom numbers, the noise of the laser beam dominates the absorption signal; although absorption imaging at the level of individual atoms is possible in principle, it is technically very demanding to get a smooth and stable enough laser profile to be able to carry out this kind of measurement; the lowest number of atoms detectable by absorption imaging in a typical experiment is in the range 100-1000.

### **Fluorescent imaging**

Fluorescent imaging is the counterpart of absorption imaging, in that it detects laser light resonantly scattered by the sample to measure the atomic spatial distribution. The technique whose development is described in this thesis is at heart a fluorescent imaging technique; see the next section (Section 4.3) for a detailed discussion of the above criteria in this case.

**Optical cavity detection**

Detection of single atoms is possible when they are in a mode of a high finesse cavity. In an experiment probing a cold, coherent atomic state [95] the detection efficiency was around 20%; if atoms can be reliably confined at the centre of the cavity mode, the detection efficiency can be expected to be nearer 100%. However, the spatial resolution, which is determined by the volume of the cavity mode, is poor, so this method is unsuitable for the situation under consideration.

**Metastable helium incident on a microchannel plate**

Experiments with metastable helium can achieve detection efficiencies approaching 100% [85, 46]. However, this method is only available in time-of-flight to specific ultracold species, and has very poor horizontal positional resolution (around 250  $\mu\text{m}$ ).

**Electron beam ionisation and ion detection**

Electron beam ionisation has the capability to resolve single atoms at individual lattice sites [26]. However, the major drawback of this method for the situation under consideration is that the detection efficiency for each atom is only about 10%, both due to detector inefficiencies, and other collisional channels. The theoretical maximum efficiency possible with this method is around 40-50%. Furthermore, it is hard for such experiments to take 3D images, which will be needed for mapping the distribution of 3D optical lattices.

**Photoionisation and ion detection**

The method of photoionisation and ion detection [92, 54] works similarly to electron beam ionisation. There are two main differences. Firstly, the maximum possible detection efficiency approaches 100% for photoionisation as opposed to between 40-50% for electron beam ionisation. Secondly, the maximum spatial resolution is limited to around 1  $\mu\text{m}$  for photoionisation as opposed to about 100 nm for electron-beam ionisation. Both would be largely limited to 2D atomic samples.

### 4.3 Fluorescent imaging and the criteria for the observation of individual atoms in a strongly interacting quantum system

Fluorescent imaging samples the resonant light scattered by the atomic sample. Compared to absorption imaging, there is less signal per atom as each scattered photon does not necessarily contribute to the detected signal; but on the other hand the signal-to-noise ratio is much greater for each atom, as the laser beam itself is not incident on the CCD camera. This makes it the imaging method of choice for low atom numbers. One disadvantage of fluorescent imaging is that, because of this low signal per atom, the exposure time to laser light must be relatively long. This makes it unsuitable for time-of-flight imaging, the usual mode of imaging for ultracold atoms.

There are three substantial problems which arise when naïvely using fluorescent imaging carry out the type of measurements we require; these are outlined in the following sub-sections.

#### 4.3.1 Resolution, distinguishability and spatial period

To properly map the atomic distribution, each well must be well resolved by the measurement—the second criterion in the list above. The systems in which strongly interacting quantum dynamics have been observed to date almost all have well separations of 370 – 400 nm, at half the wavelength of the optical lattice light. While it should be possible to achieve strongly interacting quantum dynamics in systems with larger well separations (see Section 8.4 for a more detailed discussion), a larger well separation gives a weaker collisional interaction term, making it harder to probe the strongly interacting regime.

During the measurement, the Rayleigh resolving power of a lens of focal length  $f$  and diameter  $d$  is

$$\Delta x_{lim} = \frac{1.22\lambda f}{d} = \frac{0.61\lambda}{\text{NA}} \quad (4.1)$$

as

$$\text{NA} = \sin \theta = \frac{d}{2f}. \quad (4.2)$$

Equation 4.2 assumes the working medium of the lens is air or vacuum;  $\theta$  is the half-angle subtended by the lens at the focal point<sup>1</sup>.

There are relatively few transitions to choose from for resonant scattering, and typically the optical lattice light and the resonant light would both be in the vicinity of the strong alkali D transitions. It is difficult to simultaneously meet the twin requirements of strongly interacting quantum dynamics and resolvable lattice sites.

The experiment described in the preprint [4] comes closest to meeting both criteria. A very high numerical aperture objective lens is used, and lattice sites of a 2D lattice with 640 nm spacing are observed. Strongly interacting dynamics are yet to be seen in this system. Although it is probably possible to observe strongly interacting dynamics with this well separation, lower spatial periods are preferable for strongly interacting dynamics.

It is possible in principle to resolve the sites of counter-propagating optical lattices by using higher-frequency resonant light with a very good microscope objective. For example, for rubidium, using the  $5s \rightarrow 6p$  421 nm transition and a numerical aperture of 0.8, the Rayleigh  $\Delta x$  is 316 nm; the sites of a 400 nm period lattice should be resolvable for one- or two-dimensional geometries. However, with such an experiment it would be very hard to meet the next two criteria (Sects. 4.3.3 and 4.3.2): the same lattice would need to be used for coherent quantum dynamics, which needs a large frequency detuning to suppress scattering, as when imaging takes place, which needs a deep lattice to withstand many photon recoils, and so is typically much nearer the optical resonance. Furthermore, light-assisted collisions (Sect. 4.3.3) and photoionisation (Sect. 7.4.6) would pose significant problems<sup>2</sup>.

Another possible way to get around this problem is to go to a low dimensionality lattice (1D). The small number of nearest neighbours may mean that the occupancy of each well can be inferred by careful processing of the image, even if this well separation is below the diffraction limit. The experiment of Reference [48] has made some progress down this route, with very low density samples. Although the experiment provides

<sup>1</sup>The latter equality of 4.2 holds as the wavefront exiting the lens is spherical rather than planar.

<sup>2</sup>It is possible that variations may be conceived, such as the use of absorption imaging at shorter wavelengths which capable of detecting single atoms.

some evidence that the atomic separation could be inferred below the diffraction limit of the system, to be applicable to strongly interacting systems this technique must be demonstrated in lattices with atomic densities approaching one atom per site. This is a significantly harder experiment, but may be possible with a sufficiently good imaging system and good image post-processing. This technique is limited to low dimensionality systems.

There is not so much interest in probing the spatial resolution of the atomic distribution at resolutions smaller than that of the extent of the lattice site; this is because we assume that the strongly interacting quantum dynamics takes place in the lowest band; this is true in almost all cases of current interest. Instead, to gather information on excitations in higher bands, it would probably be easier to use time-of-flight (TOF) measurements (see Section 7.1).

### **4.3.2 Signal-to-noise ratio**

There must be enough signal from each atom for it to be unambiguously identified. The trouble is, as atoms scatter photons, they heat up due to the recoil from the absorbed and spontaneously scattered photons, gaining on average one recoil energy ( $E_R$ ) per cycle. Once an atom is too hot, it escapes the well. Once it has escaped, it no longer contributes to the identifiable signal of a certain atom at a certain site; it may contribute to background in the rest of the image, or disappear from the imaging region altogether; furthermore, it could undergo a light-assisted collision with an atom in another well (see the next section), with the result that both atoms are immediately lost from the lattice.

Deep optical lattices can have depths of hundreds to thousands of recoil energies, and with typical fluorescent photon detection efficiencies of around 1-5%, each atom would leave a signal of only a few to a few tens of photons, spread over a few pixels of a CCD chip. While for a 1D or 2D sample this may be on the limits of detectability, it is a rather fleeting glimpse of each atom, and is unlikely to be a clear, unambiguous signal, even if all noise sources are carefully eliminated. For a 3D sample, the scattering of out-of-focal-plane atoms obscures any such faint signal.

### 4.3.3 Light-assisted collisions

Lastly, the strong light-assisted collisional atom loss processes must be suppressed to allow the true atom distribution to be measured. Light-assisted collisions are inelastic collisions between atoms which occur in the presence of resonant light. Two possible types of light-assisted inelastic channels are described in Figure 4.1. Both of these channels have large cross-sections when atoms approach each other in an excited state, as occurs in the presence of resonant light.

The effect of these collisions is the transfer of a large amount of internal energy of the excited biatomic system into the kinetic energy in the centre of mass frame of the colliding atoms. This energy is typically much greater than the potential energy needed for the atoms to escape the potential minimum of the optical lattice; as a result, both atoms get ejected from the optical trap with a high velocity.

Two atoms confined in one lattice site have a large wave function overlap integral, and the lifetime of the two atoms in the same well under resonant illumination is very short (sub-millisecond) compared to the exposure time of a fluorescent image (tens to hundreds of milliseconds over which to integrate the low signal from individual atoms). Experiments using fluorescent imaging of atoms in periodic optical potentials, such as those in References [71] and [4], see only the residue left after these collisions have taken place: an even number of atoms initially present at a site will all be ejected; an odd number of atoms initially present at a site will be reduced to a single atom which will fluoresce in isolation and be detected. The number of original occupants of the lattice site is therefore not determined, bar it being an even number (or zero), or an odd number.

Experiments which wish to use fluorescent imaging to look at strongly interacting quantum states should address all three of these problems. The experiments which have come closest to this goal to date (Nelson *et al.* [71] and Bakr *et al.* [4]) overcame only one of these issues (that of the signal-to-noise ratio), though the latter experiment may also be able to demonstrate concurrent resolvability and strongly interacting dynamics.

The technique which is described in this and subsequent chapters relies on flu-

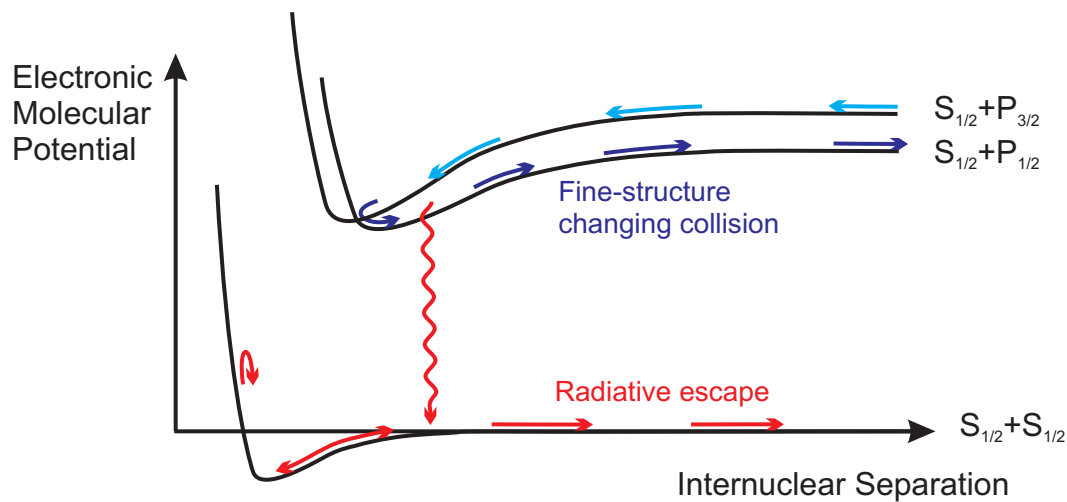


Figure 4.1: Channels for light-assisted collisional loss processes of a pair of neutral atoms. The atoms approach each other with one atom in the excited  $P_{3/2}$  electronic state (blue arrows). The excited molecular states have a wider and deeper attractive potential region due to the  $1/r^3$  form of the resonant dipole-dipole interaction, as opposed to the  $1/r^6$  form of the ground state Van der Waals potential. During the collision one of two inelastic processes may happen. The first mechanism (illustrated by the red arrows) occurs by the decay of a red-shifted photon while the atoms are in the attractive region of the excited molecular potential. This process, called radiative escape, leaves the two atoms unbound in their ground state with substantial kinetic energy, so they fly apart and out of the trap. A second process, a fine-structure changing collision (illustrated by the purple arrows), occurs when other molecular potentials cross the initial excited state molecular potential; there can be coupling between the excited state potentials, so the atoms have a probability of transferring to the other potential. The potential energy released is again manifested as a large increase in kinetic energy leading to the loss of the atoms.

orescent detection. Crucially, it is designed to overcome all three of these problems simultaneously for a lattice of any dimensionality.

#### 4.4 The accordion lattice

To tackle the problem of resolvability of the lattice sites I propose to use an accordion lattice—a lattice with real-time control of the lattice periodicity. The accordion lattice was initially proposed in the article of Li *et al.* [61] and developed further in our paper [99]. I have subsequently developed these ideas further, as described below.

Our design for a 1D accordion lattice is shown in Figure 4.2b. The major benefits of using acousto-optic control of the periodicity over mechanical control [61, 22] are substantially improved response time, reproducibility and precision.

There are a couple of subtleties of the one-dimensional accordion lattice. The first concerns the extent of the lattice, which is determined by the overlap of the lattice beams. It is assumed that the beam is collimated at the AOD, which it more or less needs to be to satisfy the Bragg criteria. For the M1 beam (the red/blue beam of Figure 4.2b) the lenses L1 and L3, when separated by the sum of their focal lengths, form a telescope which magnifies the angle of the beams but correspondingly demagnifies the beam waist size; thus the lattice envelope size is determined by the width of the initial beam through the deflector aperture. Furthermore, it is desirable to make the waists of the two beams equal; this can be accomplished by ensuring that the lengths of BS-M1 and BS-M2 differ by  $2f_2$  (this can be justified by considering that the light field one focal length behind a lens is the Fourier transform of the light field one focal length in front). The coherence length of the laser light must be greater than the difference in path lengths ( $\sim 4f_2$ ); the coherence length of a laser with a Lorentzian linewidth of 1 MHz is around 100 m, so this should not pose a problem for most lasers.

A related subtlety concerns the phase between the beams at the centre of the accordion lattice as the angle  $\alpha$  changes. This can best be understood by considering a point source on the optical axis at the acousto-optic deflector. This point source is imaged onto the centre point of the lattice by both paths; the intensity of this image is given by the relative phases of the two paths, and can be varied by altering the position

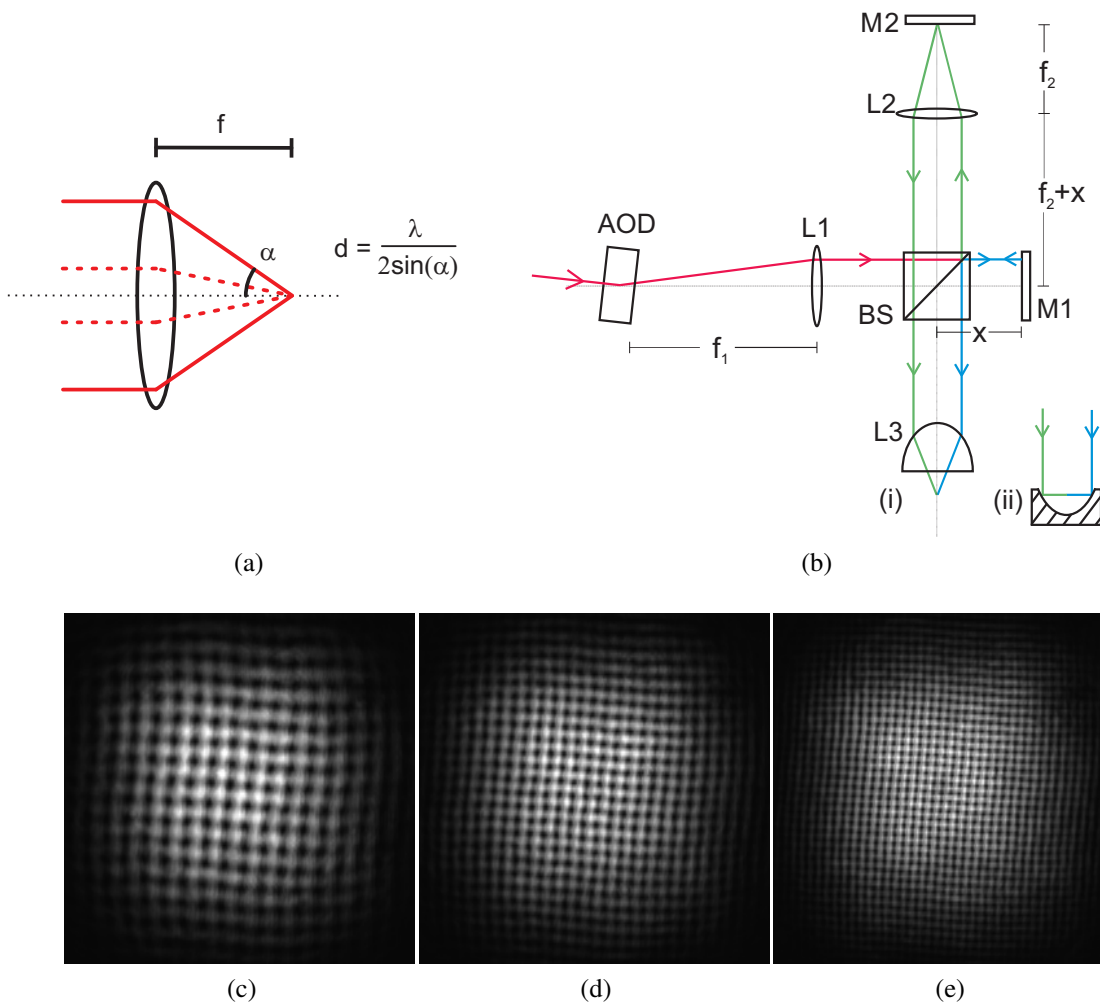


Figure 4.2: The accordion lattice; Figure (a) shows the basic design. A pair of beams enters a lens parallel to the optical axis; the beams interfere in a region around the focal point of the lens to produce a one-dimensional optical lattice. The separation between the potential minima is dependent on the off-axis displacement of the incident beams (see Fig. 2.1). Figure (b) shows a simplified optical layout which can be used to generate a pair of accordion lattice beams. The acousto-optical deflector (AOD) is at the focal point of the first lens; the deflection angle determines the off-axis displacement of the beams. The optical axis after the deflector is set to a non-zero deflection angle. The beamsplitter path M2 produces the second beam by using a lens to reflect the original beam in the optical axis. A two-dimensional optical lattice of this design can also be used as a rotating lattice [99]. Figures (c)-(e) show images of a two-dimensional accordion lattice, with lattice periodicities of (c)  $131 \mu\text{m}$  (d)  $87 \mu\text{m}$  and (e)  $59 \mu\text{m}$ . Large periodicities were used for these images so as to allow the pattern to be easily resolved. Photographs by R. Williams; diagram (b) adapted from our publication [99].

of the mirror M1 on the scale of a wavelength. The shape of the wavefronts at both the source and image are spherical; it can therefore be seen that the phase relationship between rays emitted at different angles from the source is preserved at the centre point of the lattice. In conclusion, small adjustments using a piezoelectric device (and/or a precision translation stage) at the mirror M1 can be used to set the phase at the centre of the lattice or to move the lattice along the lattice vector. The phase at the centre of the lattice is preserved as  $\alpha$  changes (for aligned, aberration-free optics). In practice aberrations in L2 will cause the centre of the lattice to move a little as the period is changed.

The polarisation optics, not shown in Figure 4.2b ensures that the two beams have the same polarisation at the last lens L3 (to produce a lattice with intensity gradients rather than polarisation gradients). This can be done by a polarising element, which would lead to power loss, or by a waveplate positioned so that changes the polarisation of light only on one side of the optical axis.

Two and three-dimensional optical lattices can be formed by using more beams. A simple way to form a square lattice is to use one pair of beams per dimension; the pairs of beams are frequency detuned from each other by at least a few megahertz to avoid cross-terms in the atomic potential. Other lattice geometries can also be made using different beam configurations. A two-dimensional accordion lattice made with a pair of two-dimensional AODs can also be used as a rotating optical lattice [99].

The minimum distance between the lattice sites possible with a convex lens is dependent upon the working numerical aperture NA of the lens:

$$d_{min} = \frac{\lambda}{2NA}. \quad (4.3)$$

A high numerical aperture convex lens may have a vacuum NA of around 0.5, giving a minimum lattice period of around  $\lambda$ . This is about acceptable, but not ideal, for strongly interacting physics in optical lattices. I have therefore designed a method to allow accordion lattices to be used at the ideal spacing of  $\lambda/2$ , whilst still allowing maximum lattice site separations of some microns. The method I propose is the use of *in vacuo* parabolic or elliptical reflectors (Fig. 4.3).

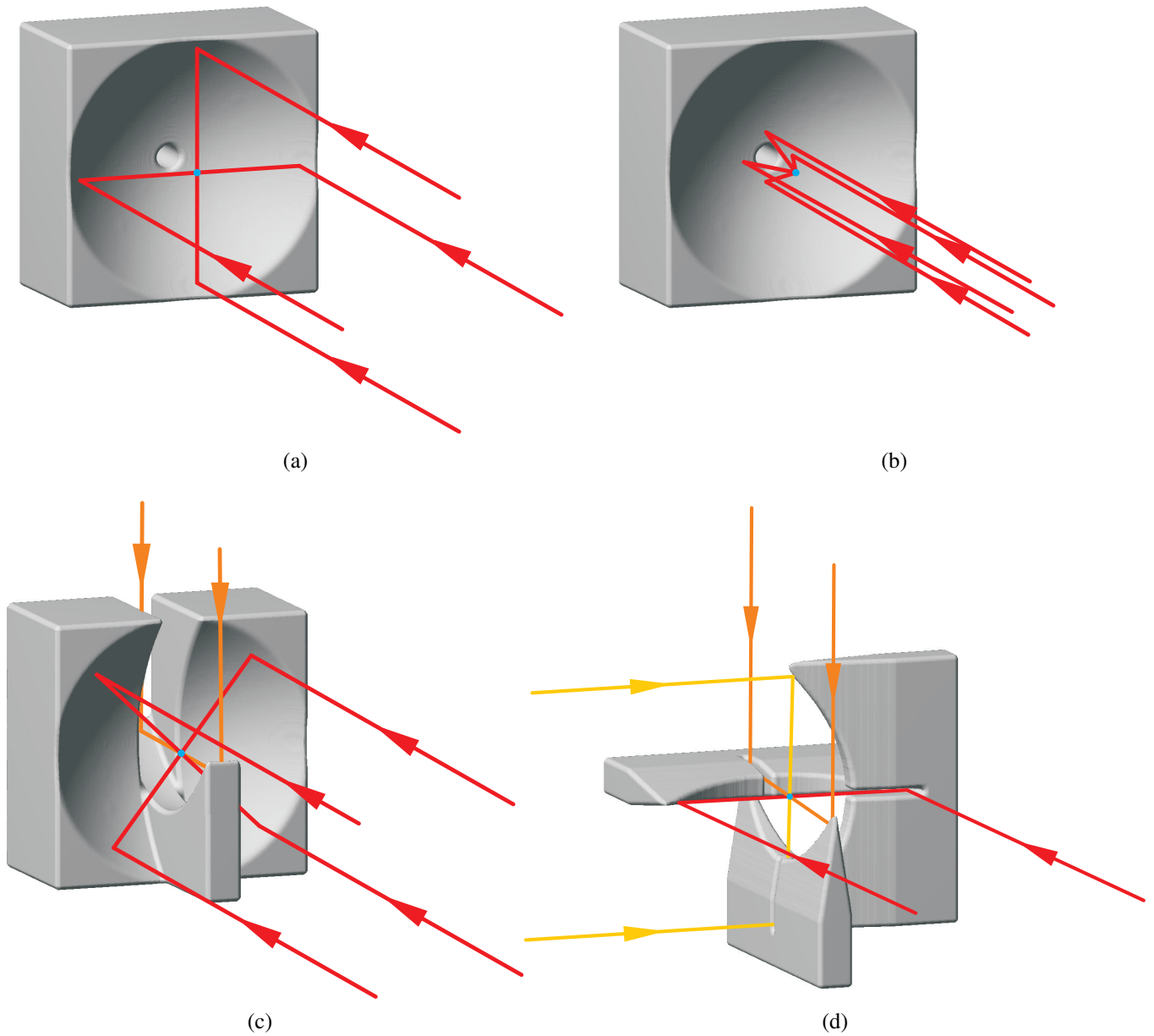


Figure 4.3: The use of parabolic reflectors to make counter-propagating accordion lattices. Figures (a) and (b) demonstrate the variation of the lattice period of a two-dimensional lattice. An optional hole is shown in the centre for optical access to the atoms from the far side of the mirror. The arrangement shown here is also applicable for a rotating optical lattice. Figure (c) shows one possible arrangement for a 3D parabolic accordion lattice. A variation of this arrangement allowing for better optical access is shown in Figure 7.2. Figure (d) shows another configuration; in contrast to Figure (c), each set of beams enters the region from a different direction, at the expense of a more intricate design.

Two-dimensional counter-propagating accordion and rotating optical lattices can be made (Fig. 4.3a) with a single parabolic reflector inside the vacuum system. The mirror configurations for three-dimensional counter-propagating accordion lattices are a little more complex, as shown in Figures 4.3c and 4.3d; for example, a central slice is ‘cut’ from the reflector and turned  $90^\circ$  (Fig. 4.3c).

Counter-propagating accordion lattice designs using elliptical mirrors are also possible. These would differ from the parabolic arrangements by the addition of an extra lens before the mirror; this lens would pass (the centre of) all accordion lattice beams through the secondary focus of the ellipse; these would then be reflected to the primary focus of the ellipse, the position of the atoms.

Expansion or contraction of the accordion lattice will potentially heat the atoms, with higher heating rates likely further from the centre of the lattice. This is a consideration if the lattice period is required to be changed during coherent quantum evolution. However, the effect of heating will be negligible if the expansion occurs before imaging, providing that the expansion keeps each atom its original well. For example, consider atoms at a site of a counter-propagating lattice with vibrational frequency 30 kHz; during the expansion of the accordion lattice let us say that it travels a distance of  $100\ \mu\text{m}$  in 10 ms as it expands to 10 times its original period. Assuming periods of constant acceleration and deceleration, the maximum site displacement due to this acceleration would be less than 0.5% of a lattice period; the added energy this perturbation would give the atoms would be negligible compared to the lattice depth.

#### 4.4.1 Collimation of lattice beams for the counter-propagating accordion lattice

The accordion lattice beams should be collimated at the position of the atoms in order to provide a uniform lattice. This can be arranged easily if all focal surfaces are planar, as is approximately the case with well-chosen transmission lenses, as described above. However, the parabolic surface manifestly does not have a planar focal surface (see Fig. 4.4). Using geometric optics, the focal point for a small bundle of collimated rays

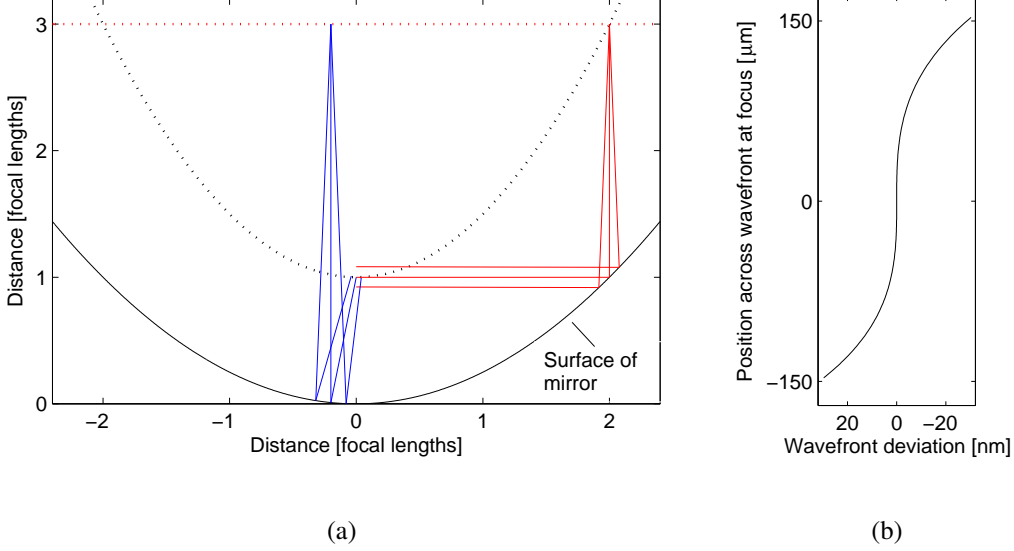


Figure 4.4: Lattice beam collimation for the parabolic imaging lattice. It is desirable to have a collimated lattice beam at the focus of the parabola; this occurs when the focus of the incoming beam (propagating parallel to the axis of the parabola) lies on the black dotted line. It is suggested that the focal surface of the penultimate lens (shown as the red dotted line) should be chosen to intersect this surface at the point when accordion lattice beams counter-propagate (the red beams). The residual wavefront distortion at the atoms with this configuration is shown in Figure (b), for a parabola of focal length 7.5 mm with a beam diameter of  $300\ \mu\text{m}$  at the atoms. Smaller angle configurations (the blue beams) will have different widths and curvatures at the atoms; however, with these it is not so critical that the lattice is uniform.

passing through the focus of the parabola can be found to lie on the surface

$$y_F = \frac{x^2}{4f} + \sqrt{x^2 + \left(f - \frac{x^2}{4f}\right)^2} \quad (4.4)$$

for the parabola  $y = x^2/4f$ .

In principle it should be possible to design an optical system to have a focal surface that matches this surface, so that the accordion lattice beams are collimated no matter what period the lattice has. In practice, this is probably more complex than is needed for many experiments.

For many accordion lattice experiments, the counter-propagating accordion lattice configuration is likely to be the only configuration in which coherent quantum tunnelling is required to occur. In all other configurations, all that is needed is that the atoms

are confined to a particular well as they are transferred to the large-period configuration of the accordion lattice. Therefore we can optimise the accordion lattice collimation for the counter-propagating lattice, in which the quantum dynamics occur, and can make do with imperfect collimation for other lattice periods; in the case of imperfect collimation, the lattice envelope will be a different size, and the lattice itself will be slightly distorted over long distances.

To analyse this in more detail, the residual wavefront distortion has been modelled for the counter-propagating configuration, in which the lattice beam is focussed at a distance of  $2f$  above the mirror surface (see Fig. 4.4b). The residual wavefront distortion at the position of the atoms is much less than a wavelength for typical experimental parameters. When this lattice is expanded into the large-period configuration, the beam is not collimated at the atoms, but is focussed a distance  $f/2$  above the atoms; the beam waist at the atoms is half of the beam waist at the counter-propagating configuration<sup>3</sup>. This should not pose a problem as long as the beam waist is sufficiently wide when the beams are counter-propagating. This argument has been for one dimension, but also works for a parabolic mirror with cylindrical symmetry.

The above discussion is to some extent also applicable to accordion lattices using a (probably aspherical) transmission lens as the last lens (M3 of Fig. 4.2b). The focal surfaces of such a lens will not be truly planar; again, the accordion lattice collimation can be optimised for the most critical lattice period.

It is worth noting that, even with the mirror made from a large block of substrate as in Figure 4.3c, the optical access is actually not that restricted; all beams which are parallel to the axis of the parabola and focussed on the surface given by Equation 4.4 will intersect the atoms, and be approximately collimated at the atoms. In effect, angles of the incident beams at the atoms within one half hemisphere are mapped to displacements from the axis of the parabola.

---

<sup>3</sup>This assumes that the focal plane of the previous part of the optical system lies in a plane as described by the red dotted line of Figure 4.4a; if this surface is not planar, these figures are a little different.

#### 4.4.2 Maximum distance between accordion lattice sites

It is important to consider which factors affect the maximum distance between lattice sites since this affects the design of the imaging lenses and the measurement of three-dimensional samples (see Sect. 7.2). For accordion lattices generated with a high numerical aperture transmission lens there is not any particular restriction on the maximum period of the lattice; nearly co-linear beams into the final lens will generate an intensity pattern with an arbitrarily low number of minima across the beam envelope; for example, it would be possible to expand such a lattice so that only one site remains.

For many designs of parabolic counter-propagating accordion lattices it is convenient to have a hole at the centre of the mirror. The maximum site spacing in these cases is by the size of the hole (or slice) and the waist of the incoming laser beams; for typical parameters, this maximum spacing will be many microns, large enough to be easily resolvable upon measurement. An experiment with an accordion beam diameter of  $d_b$ , and a parabola of focal length  $f$  and central hole diameter  $d_h$  will have a maximum site separation of around

$$d_{max} = \frac{f}{d_h + d_b} \lambda . \quad (4.5)$$

If there is no hole at the centre of the mirror, the maximum separation between lattice sites is determined only by the width of the atomic sample and the accordion lattice beams (the criterion being the prevention of multiple beam overlaps at the region of the atomic sample). An experiment with an atom sample of width  $d_a$  will in this case have a maximum site separation of around

$$d_{max} = \frac{f}{d_a + d_b} \lambda \quad (4.6)$$

along these directions. For example, this is  $30\lambda$  for  $d_a = 50\mu\text{m}$ ,  $d_b = 200\mu\text{m}$  and  $f = 7.5\text{ mm}$ .

#### 4.5 The imaging lattice

The accordion lattice overcomes the problem of resolvability. We now turn our attention to the suppression of light-assisted collisional losses (Sect. 4.3.3). If resonant light is used to probe the sample, the only truly effective way to suppress light-assisted collisions during long measurements would seem to be the mutual isolation of all the fluorescing atoms. This is difficult for atoms in standard counter-propagating optical lattices of  $\lambda/2$  period, as it is hard to find a method to divide up each lattice site; however the use of an accordion lattice suggests a clear solution.

The idea is to use an additional optical lattice, which I call the imaging lattice, while the atoms are fluorescing. Let us assume that the quantum dynamics of interest have taken place in the accordion lattice, whilst it is in the counter-propagating configuration. The accordion lattice then expanded into the large-period configuration; the imaging lattice is turned on. The imaging lattice is formed by three sets of counter-propagating laser beams in three orthogonal directions, giving a 3D lattice of period  $\lambda/2$ , which is substantially smaller than the spacing of wells in the expanded accordion lattice at the time of imaging. Therefore each well of the wells in the large-period accordion lattice is subdivided into many smaller wells within the imaging lattice. The ratio of the densities of wells in the accordion and imaging lattice is given by

$$\frac{D_i}{D_a} = \frac{1}{\sin^3 \alpha} \quad (4.7)$$

with  $\alpha$  defined in Figure 4.2a; subscripts  $a$  and  $i$  are taken to refer to the accordion and imaging lattice respectively. For example, with  $\alpha$  equal to 0.1 radians ( $\sim 6^\circ$ ), this ratio is  $10^3$ .

In typical situations of interest, the atomic occupation  $n_a$  is less than 10 atoms per site of the original lattice. As the imaging lattice is switched on, these atoms divide amongst the many wells of the new lattice; due to the ratio of the well densities of the imaging and the large-period accordion lattices, the atoms have a high probability of being isolated from each other in the imaging lattice. Taking the density of atoms in the original accordion lattice site to be  $\rho_a(\mathbf{r})$ , the average number of atoms at an imaging

lattice site  $i$  is

$$\langle n_i \rangle = \frac{\lambda^3}{8} \rho_a(\mathbf{r}_i) \quad (4.8)$$

If we assume that the atoms are evenly distributed within a volume  $V$ , then  $\rho_a = n_a/V$  and  $\langle n_i \rangle$  is found to be in the region of  $10^{-2}$  for typical parameters. A more accurate calculation would use the spatial distribution of non-interacting bosons with a finite temperature  $T$ ; assuming that the atoms are distributed between enough quantum states to neglect Bose correlations, and using a semi-classical approximation for the isotropic harmonic oscillator, this is ([77] p29)

$$\rho_a(\mathbf{r}) = \frac{n_a}{(\pi R^2)^{\frac{3}{2}}} \exp\left(-\frac{r^2}{R^2}\right) \quad (4.9)$$

with  $R^2 = 2k_B T/m\omega^2$ .

Neglecting collisional dynamics and quantum correlations, this division is a individual particle probabilistic process. The original occupancy probabilities for site  $i$  of the imaging lattice are given by

$$P(n_i) = \frac{n_a!}{n_i! (n_a - n_i)!} \left(\frac{\langle n_i \rangle}{n_a}\right)^{n_i} \left(1 - \frac{\langle n_i \rangle}{n_a}\right)^{n_a - n_i}. \quad (4.10)$$

This binomial distribution tends to a Poissonian form as the number of wells becomes large. In the event that this is the limiting factor on the imaging fidelity, as is likely to be the case if background gas collisions can be ignored (see Sects. 6.3 and 7.3.4), the fidelity may be found to be

$$F = \frac{\text{Average number observed}}{\text{True number}} = \frac{\sum_i \langle \tilde{n}_i \rangle}{n_a}. \quad (4.11)$$

where  $\langle \tilde{n}_i \rangle$  is expectation value for the number of atoms at site  $i$  after light-assisted collisions remove atom pairs. This is

$$\langle \tilde{n}_i \rangle = \sum_{n_i \text{ odd}} P(n_i) = \frac{1}{2} \left(1 - \left(1 - 2\frac{\langle n_i \rangle}{n_a}\right)^{n_a}\right). \quad (4.12)$$

For  $\langle n_i \rangle \ll 1$  the fidelity reduces to

$$F = 1 - \frac{n_a - 1}{n_a^2} \sum_i \langle n_i \rangle^2, \quad (4.13)$$

and for atoms evenly distributed amongst  $M$  imaging lattice sites this further reduces to

$$F = 1 - \frac{n_a - 1}{M}. \quad (4.14)$$

An interesting observation is that this is an unusual situation where heating of the atomic sample is actually desirable. Before the imaging lattice is switched on, by heating the atoms trapped in the large-period accordion lattice, or by decreasing the intensity of the accordion lattice (but either way not enough to allow the atoms to hop between sites), the atoms can be made to occupy a larger volume at each site. This will mean that it is even more likely that they will be isolated from each other after the imaging lattice is loaded resulting in higher measurement fidelity. For example, a way to achieve this in practice would be to displace the accordion lattice site by around a sixth of a spatial period on a time scale quicker than the lattice frequency, before waiting a the length of time needed for a few rethermalisation collisions. With the use of such a technique, the fidelity is around 99% for typical parameters<sup>4</sup>.

#### 4.5.1 Practical considerations

The imaging lattice will need to be deep enough (hundreds of  $\mu\text{K}$ ) to reliably contain the atoms as they fluoresce. Lattices of these depths may most conveniently be formed by using light which is relatively near the atomic resonance i.e. frequency detuned by a few tens of gigahertz, where less laser power is needed than further off resonance. The lattice light will scatter from the atoms, but this does not matter as long as this remains a small fraction of the overall scattering rate. It would be somewhat preferable to use blue frequency detuned light for the imaging lattice, as there will be a little less scattering, and less offset between the ground level substates. If the energy offset between the ground level substates is too large, the polarisation gradient cooling process becomes

<sup>4</sup>Typical parameters in this instance are a few rubidium atoms per site of an accordion lattice of final period  $7 \mu\text{m}$ , with the atoms occupying around  $(1/3)^3$  of the total volume of the site.

disrupted; this sets a lower limit on the frequency detuning of the imaging lattice from resonance.

There is a significant practical advantage to using a different optical resonance for the imaging lattice than for the fluorescent signal, as stray light from the lattice can be easily filtered from the signal. For example, for alkalis, one may use the D2 resonance for fluorescence, and the D1 resonance for the imaging lattice.

As is standard practice, each pair of imaging lattice beams should be frequency detuned by a few tens or hundreds of megahertz from the other pairs. The polarisation of the beams of the imaging lattice should be linear to reduce the energy difference between the ground state sublevels.

Tunnelling between the lattice sites is completely negligible in the deep imaging lattice, unlike for lattices of lower depths, in which tunnelling is a major factor in the atomic dynamics. The intensity ramp during the switch-on of the imaging lattice should be slow enough to make sure that the temperature of the atoms at the end of the ramp is a reasonably small fraction of the final lattice depth. The deep potential and high frequencies of the imaging lattice means that this can be rather fast in comparison to the time needed to turn on other types of optical lattice; furthermore, the intensity increase need not be adiabatic.

#### **4.6 Cooling while detecting in the imaging lattice**

As discussed in Section 4.3.2, the atoms will unavoidably be heated as they fluoresce due to recoil from the emitted photons. Without a means of cooling the atoms, they would quickly be lost from the sample, and consequently the total detected fluorescent signal from each atom would be very low.

This section will discuss and contrast several laser cooling methods appropriate for use on lattice-confined atoms. Each method involves the scattering of spontaneously emitted photons; these photons, which are a side effect of the cooling, can be used to image the atomic distribution. One of these methods will be chosen to take forward in the subsequent detailed analysis of the imaging lattice technique.

#### 4.6.1 Outline of cooling methods

##### Raman sideband cooling of lattice-trapped atoms

The Raman sideband cooling method uses transitions between magnetic sublevels to cool the confined atoms. There are two parts to the Raman sideband cooling process. Firstly, the atoms are transferred by a Raman transition from one quantum state to another; the second quantum state has a different internal angular momentum, and a vibrational state which is less than the first state. The atom is then optically pumped by another laser beam, within this vibrational level, to restore the original magnetic sublevel. The process can then be repeated.

A magnetic field is typically used to tune the energy difference between magnetic substates to be the same as the energy difference between the vibrational levels of the well. Raman transitions can therefore occur between near-degenerate states without additional frequency differences in the laser light. For three-dimensional cooling, the vibrational sidebands are made to be approximately degenerate.

The matrix element of the Raman transition must be non-zero; this is the case if the optical lattice already has polarisation gradients, and the frequency detuning of the lattice is much less than the fine structure frequency separation [51]. If the polarisation of the lattice is uniform, additional Raman beams must be used to introduce polarisation or intensity gradients to induce Raman coupling between vibrational states [34].

The final (ground) state is usually chosen as a dark state to minimise the final temperature of the atoms.

##### Swept sideband Raman cooling

The Raman cooling technique as described in the previous section is dependent upon the ability to tune the energy difference of the sublevels due to the magnetic bias field to be the same as the frequency difference between the vibrational atomic levels. The separation of vibrational levels is constant with increasing energy for a parabolic potential, but the optical lattice only approximates a parabolic potential locally at the lattice sites. Therefore the hotter the atoms are, the less efficient the technique becomes, and will break down completely for atoms with energies near the continuum. A potential way

to extend the cooling range of this technique is to sweep the frequency of the Raman frequency detuning. In this way, the technique becomes somewhat similar to free-space Raman cooling [49]. However, if the sidebands are swept, the time needed for a single cooling stage increases.

### **Dissipative optical lattices**

Atoms can be polarisation gradient cooled using optical molasses. The molasses beams interfere and form a near-resonant optical lattice at the atoms. If the parameters of the molasses beams are chosen carefully, a stable optical lattice may be formed, and for some parameters the atoms can be localised within the wells of the lattice [79, 50].

### **Polarisation gradient cooling of lattice cooled atoms**

In contrast to dissipative optical lattices, polarisation gradient cooling can also occur when atoms are held by a separate potential. This is the method used in previous experiments which have been able to detect individual atoms in optical lattices [71, 4].

#### **4.6.2 The choice of cooling method**

A choice will now be made of which cooling technique is best for the situation at hand. It is clear that each of these techniques is able to cool the atoms within the imaging lattice. By alternating periods of fluorescent scattering with any of these techniques, it will be possible to prolong the lifetime of the atoms at a single site of the lattice, and so increase the fluorescent signal at the detector. However, to pick the cooling technique used in the further analysis of the experimental proposal, the technique will be chosen which seems to be best suited to give maximum fidelity for the fluorescent measurements. This means that the atoms should be confined at a single site of the lattice for as long a time as possible, and that the atoms must fluoresce as much as possible, to maximise the detected signal.

It may well be that having the best cooling possible is somewhat of an overkill for some experiments; for example, the detection of the distribution of a small two-dimensional sample by a high numerical aperture lens will likely only require a short

exposure time. However, I would like to look towards the more powerful potential applications of this technique; for example, the detection of tens of thousands of atoms in many layers of a 3D sample. The total exposure time needed for such measurements may be many seconds as various portions of the sample are sequentially brought into the focal region of the imaging system.

This choice is not based on an exhaustive study of each of the above cooling techniques, as the time needed to do each technique justice is beyond the time available. Instead, broad arguments will be used which indicate that one particular technique has advantages over the rest. The excellent properties of this technique found in the subsequent analysis give a retrospective justification for this choice.

To maximise the lifetime of atoms in the lattice it is necessary to maximise the lifetime of atoms at a particular site. If atoms can hop between sites they will eventually meet each other and be lost in light-assisted collisions; furthermore, the spatial resolution of the measurement is degraded. To maximise the lifetime of atoms at a particular site, it seems sensible to pick a cooling technique can cool the atoms in every bound vibrational state. It is desirable for the cooling technique to cool even those atoms which have energies greater than the depth of the lattice; these atoms will have a good probability of being recaptured before leaving that lattice site, or being captured by a close neighbour.

These considerations make sideband Raman cooling, discussed above, seem less appropriate for very long lifetimes; the cooling method decreases in efficiency as the motional energy of the atoms becomes greater. Furthermore, the time needed for Raman cooling as used in previous experiments is relatively slow (1-10 ms [34]) compared to polarisation gradient cooling (10-100  $\mu$ s [79]); faster cooling will mean that the scattering can occur at a faster rate, and so greater signal can be collected in a certain period of time. While it should be possible to speed up the Raman cooling process, polarisation gradient cooling does seem to have the advantage. The capture range of the Raman cooling technique can be extended by sweeping the energy difference of the two internal states involved in the cooling process, however this decreases the cooling rate even further.

From the above arguments it therefore seems that polarisation gradient cooling methods have the advantage. The question remains as to whether to use a separate lattice potential for atomic confinement. One advantage of using a separate lattice potential is that the cooling process is more amenable to optimisation. The intensity of the cooling light and the depth of the confining lattice are the two critical parameters relating to the atomic lifetime at a site (see Sect. 6.4), however the intensity of the cooling light in a dissipative optical lattice is inextricably linked with the lattice depth. By being able to adjust the intensity and frequency detuning of the cooling light independently of the depth of the confining lattice, these two critical parameters can be adjusted separately to enable longer site lifetimes. Another consideration is that a separate optical lattice can confine all magnetic sublevels of the ground state at each site; the sites of a dissipative optical lattice typically confine some magnetic sublevels, but not others. To decrease the hopping rate between sites, it is desirable to confine all the magnetic sublevels together.

The above considerations suggest that polarisation gradient cooling, using a lattice separate from the cooling light, is the best option. This is the method used in the two most relevant experiments to date [71, 4]. Furthermore, almost every ultracold atomic experiment uses magneto-optical trapping; the cooling light needed for the polarisation gradient technique is therefore already present in the vast majority of ultracold atomic experiments.

#### **4.7 Fluorescent imaging of atoms trapped in the imaging lattice**

This section deals with important considerations regarding the actual imaging of the atoms, as they are fluorescing while trapped in the imaging lattice.

##### **4.7.1 Cooling in three dimensions**

As will be discussed in Section 5.3, it is not enough simply to use three sets of counter-propagating molasses beams for the cooling, as the fluorescent scattering and cooling efficiency would vary substantially according to position of the site.

The methods that can be used to get around this are chopping the cooling light between the three directions, or incorporating a slight frequency detuning between the

molasses beams to cycle the molasses phases at any particular point in space (see Sect. 5.3).

As to which method should the experimenter choose, it can be seen in the results of Section 6.3 that the chopping method works very well; it would be expected that the frequency detuning method (as used in [4]) would also work well in the majority of situations. In terms of experimental implementation, both methods are more or less identical in terms of the apparatus needed, as each molasses direction will need its own dedicated AOM, and it just comes down to what signals are given to the AOM drivers. Very little optical power is needed for the cooling, so that is not an issue.

The effect of the frequency detuning of the molasses beams on the trapped atom is comparable to the atom moving on a path through stationary molasses. Three-dimensional molasses has a complex light-field landscape depending on the 5 relative phases of the beams, and atoms on different trajectories through this landscape do not necessarily display the same dynamics when averaged. The chopping method has an advantage over the frequency detuning method since all parameters are known and do not vary. Although the frequency detuning method will likely work well for most sites in the majority of circumstances, there is the possibility that the phase path traced out is inefficient for cooling at some subset of sites in the lattice; this may lead to atom hopping and loss, or perhaps a lower fluorescent signal from these sites. As for the chopping method, each site is made nearly identical, and the probability of having anomalously bad cooling (or lower fluorescence) at a certain site is substantially less.

In practice, this difference between the methods will depend on the exact experimental parameters, and may be negligible. Nevertheless, since it is no more effort experimentally to use the chopping method than the frequency detuning method, I would suggest that the chopping method is somewhat preferable, for the reasons stated.

#### 4.7.2 Shared or separate optical elements

It is possible use optical elements for the detection which are shared with or separate from the accordion lattice. In the case that the accordion lattice is generated using a high numerical aperture objective lens, it is preferable to use the same lens system for detection. Accordion lattice light and fluorescence light of different frequencies may be separated by using a dichroic beamsplitter. However, in the setup using *in vacuo* mirrors, the decision is not so straightforward. The parabolic (or ellipsoidal) surface does have a very large aperture for good fluorescence collection, and a corresponding small diffraction limit; however, off-axis aberrations, particularly coma, are a major drawback; these will severely limit the field of view. There are two options in these cases; either the aberrations could be (partially) corrected by further optics, or a separate lens could be used to image the atoms.

If the mirror itself is used for imaging, it is likely that only some portion of the total mirror aperture can be corrected, with the remainder discarded. A useful guide when designing a compensation system is the use of the optical symmetry principle [31]; for example, a second, identical, parabolic mirror could be used as part of the imaging system to cancel out aberrations which depend on odd powers of the field variables, which include coma. This still leaves distortion due to astigmatism, but the removal of coma will improve the image quality significantly, and the remaining aberration could be minimised by other optical elements.

If a high quality separate lens is used, the aberrations in the image will be a lot less, and the field of view a lot greater than the uncompensated parabolic mirror. However, the numerical aperture of this system, and the orientation of the focal plane, may not be so optimal. It may be convenient to mount this lens inside the vacuum system together with the accordion lattice mirrors. Although all the in-vacuum optical elements should ideally have coincident foci, this criterion does not have to be exact as long as the foci are separated by a distance much less than the waist of the accordion and imaging lattice laser beams<sup>5</sup>.

---

<sup>5</sup>For example, the position of the sites of interest within the imaging lattice can be shifted into the focal region of the imaging lens.

### 4.7.3 Translation of the imaging lattice and three-dimensional imaging

The imaging lattice should have the ability to translate the lattice sites in three dimensions; this is, of course, especially important for 3D imaging. The necessary shift can be accomplished by introducing a small, tunable frequency difference between the pairs of counter-propagating imaging lattice beams (or alternatively, by using retro-reflecting mirrors mounted on precision motorised translation stages).

In this way, three-dimensional imaging is possible by sequentially changing the sites within the focal plane of the imaging system. A series of exposures should be taken, each with atoms from different planes of the original lattice. Using an imaging system with high numerical aperture makes the depth of focal region short; it is a requirement that this should be less than the separation between atoms along the line of sight. The calculation of the depth of field is relatively involved (for example it depends on the relative proportion of coherent and incoherent fluorescent scattered light), but a reasonable approximation is

$$\text{Depth of field} = \frac{1}{(\text{NA})^2} \lambda . \quad (4.15)$$

For example this depth is around  $4\lambda$  for a numerical aperture of 0.5. This method of three-dimensional imaging has been successfully implemented for a lattice of  $5\ \mu\text{m} \simeq 7\lambda$  period, by the use of a lens of numerical aperture 0.55 [71].

### 4.7.4 Fluorescence from out-of-plane atoms

We have so far assumed that the atoms undergoing fluorescence only lie within the focal plane of the imaging system. For extended three-dimensional samples this is not the case, and we must consider the effects of these out-of-plane atoms. If the atomic sample is thin along the line of sight of the imaging system, the combination of a shallow field of view of the imaging system and good separation of the accordion lattice sites (both in and perpendicular to the imaging plane) is likely to be enough that the diffuse signal from the out-of-plane atoms can easily be distinguished from the atoms in the focal plane.

To take the example of the experiment described in Reference [71], the sites of

a three-dimensional lattice with  $5\ \mu\text{m}$  period were filled with around 250 atoms. The atoms within each layer were able to be clearly resolved from the background fluorescence of atoms from layers of the lattice outside the focal plane using a lens of numerical aperture 0.5.

However, if more atoms are present in the sample the background fluorescence will increase and it will become harder to pick out the signal from the atoms which are in focus<sup>6</sup>. In this case I suggest one of two measurement techniques which are a little more complex, but will greatly improve the signal-to-noise ratio of the measurements of large three dimensional samples; these are described in Section 7.2.

#### **4.7.5 Coherence and reabsorption of scattered radiation**

Once there are more atoms in the sample we must consider whether reabsorption of radiation is significant. This would potentially diminish the scattered signal and cause extra heating. It is shown in Section 6.3.5 that this is not a great issue, as the reabsorption from the size of the samples that we are interested in is weak.

Another potential complication is the coherence of the scattered radiation. Clearly the fluorescence light from two atoms well separated in the imaging plane will not interfere, but if there are two or more atoms to an accordion lattice site then we must consider the effect of this coherence on the scattered signal. In Section 6.3.4 it is shown that when the lattice is being imaged as it is being cooled, the scattered signal in a particular direction is potentially able to display some variation, depending on the relative positions of the atoms in the imaging lattice within the same original accordion lattice site. This variation will not be enough to cancel out the signal from that lattice site, but this behaviour would potentially break the linear relationship between the observed fluorescence and the number of atoms at that site, and so would make the interpretation of the image harder. A partial solution can be found by introducing a small frequency difference between each cooling or probing beam (Sect. 6.3.4). A more comprehensive solution is found by the use of a radiative cascade (Sect. 7.2), or other equivalent method.

---

<sup>6</sup>Coherent effects will also redistribute this background somewhat.

---

# THEORETICAL AND COMPUTATIONAL METHODS USED TO MODEL THE IMAGING LATTICE TECHNIQUE

This chapter describes the physics of polarisation gradient cooling both in free space and for confined atoms. An analytical treatment of polarisation gradient cooling is given which forms the basis of the numerical simulation of the imaging lattice technique. Furthermore, I have devised an extended form of the Monte Carlo technique in order to extract from the simulation the information which is of particular interest.

## 5.1 The mechanisms of polarisation gradient cooling in free space

Polarisation gradient cooling is class of laser cooling processes which exploit the polarisation gradients of light fields to cool atoms, potentially to temperatures much lower than the limiting temperature of Doppler cooling. The polarisation gradient cooling methods rely on transitions between ground-state sublevels, which can occur on a longer time scale than the excited state lifetime of the atoms. Purely on dimensional grounds, it can be argued that this longer internal time scale can make the cooling more sensitive to lower velocities. In this argument, the spatial variation of the laser beams varies on the order of  $\lambda$ , so for the dynamics to be non-adiabatic, the velocity of the atoms at least be large enough so that it travels this kind of distance before the internal states equilibrate,

i.e.  $v_{min} \sim \lambda\Gamma'$ , where  $\Gamma'$  is the minimum time scale of the internal dynamics. This internal time scale is the natural lifetime for an atom with no ground state structure, but is the optical pumping time between sublevels for an atom with multiple ground-state sublevels. With longer internal lifetimes, lower velocity atoms can potentially be cooled.

There two specific types of polarisation gradient cooling which were analysed in detail in a seminal paper by Dalibard and Cohen-Tannoudji [18]; these occur in the one-dimensional  $\text{lin} \perp \text{lin}$  and  $\sigma^+ \sigma^-$  configurations. These configurations consist of two equal intensity counter-propagating laser beams. With the cooling light propagating along  $\hat{z}$ , the electric field of the cooling light for 1D molasses has the Cartesian form

$$\mathbf{E}^+(\mathbf{z}) \propto (\cos \theta \hat{x} + i \sin \theta \hat{y}) e^{i(kz+\phi)} + (\sin \theta \hat{x} - i \cos \theta \hat{y}) e^{-i(kz+\phi)}. \quad (5.1)$$

### 5.1.1 Orthogonal linear polarisations

The  $\text{lin} \perp \text{lin}$  configuration has these laser beams as having perpendicular linear polarisation, i.e.  $\theta = 0$ . The positive component of the electric field is then

$$\mathbf{E}^+ \propto \cos(kz + \phi) \mathbf{e}_{-1} - i \sin(kz + \phi) \mathbf{e}_{-1} \quad (5.2)$$

where we have introduced the unit vectors  $\mathbf{e}_{\pm 1} = \mp (1/\sqrt{2})(\hat{x} \pm i\hat{y})$ . The light consists of alternating standing waves of  $\sigma^+$  and  $\sigma^-$  light.

We consider for simplicity the atom with a ground state of spin  $J_g = 1/2$ . The  $\sigma^+$  couples more strongly to the  $m_J = +1/2$  state, and the  $\sigma^-$  light couples more strongly to the  $m_J = -1/2$  state. The ground-state sublevel light shifts of the two states therefore oscillates according to the polarisation of the light at that point (see Fig. 5.1(a)), which is opposite for the two states. Furthermore, the  $\sigma^+$  ( $\sigma^-$ ) light will tend to pump the atoms towards the  $m_J = +1/2$  ( $m_J = -1/2$ ) state, which for negative laser frequency detuning, lies below the original state.

The motion of the atom is therefore described by a loss in translational energy as the atom climbs the lattice potential, followed by optical pumping from a peak to a trough in the lattice potential accompanied by a much smaller recoil momentum exchange (see Fig. 5.1(a)). This process is dissipative, and may laser cool atoms a long way below the Doppler cooling limit.

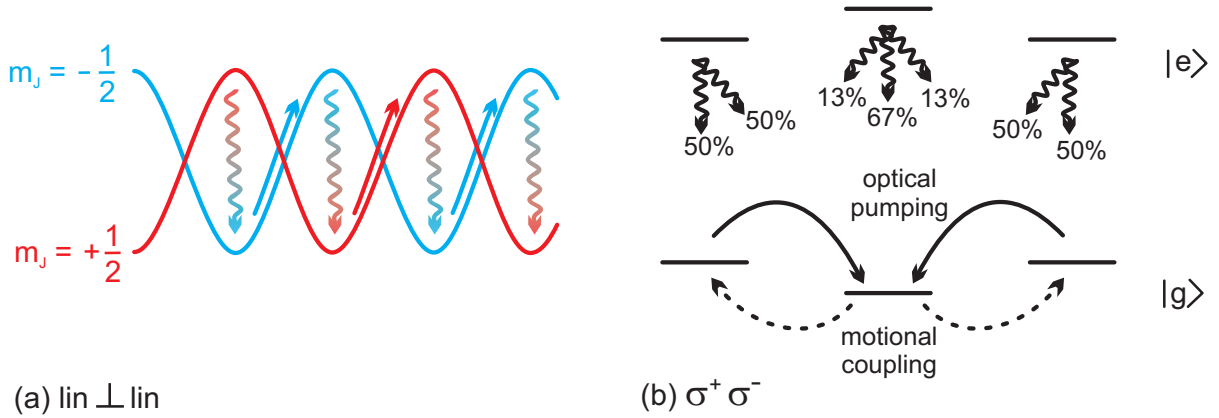


Figure 5.1: (a) The  $\text{lin} \perp \text{lin}$  configuration for  $J_g = 1/2$ . The atom loses kinetic energy as it climbs the potential; near the top of the potential, it is optically pumped to the other ground-state sublevel, which has a lower potential energy. The atom loses energy as the process is repeated. (b) The  $\sigma^+ \sigma^-$  for  $J_g = 1 \rightarrow J_e = 2$ . The upper  $m_J = \pm 2$  states are not shown as they are not involved. The excitation rates to the upper states (not shown) are in the ratio  $3/4 : 1 : 3/4$  for the three lower states. Taken together with the decay branching fractions which are shown, these optically pump atoms from  $m_J = \pm 1$  to  $m_J = 0$ . Motional coupling between of an atom originally in the  $m_J = 0$  state will add an admixture of the  $m_J = \pm 1$  states, which will increase the potential energy  $\langle E_P \rangle$ , and so generates a force which opposes the atomic motion. The net effect is to cool the atomic sample.

### 5.1.2 Orthogonal circular polarisations

The laser beams have opposite circular polarisations in the  $\sigma^+ \sigma^-$  configuration ( $\theta = \pi/4$ ). The positive component of the electric field is then

$$E^+ \propto \cos(kz + \phi) \hat{x} - \sin(kz + \phi) \hat{y}. \quad (5.3)$$

This polarisation is always linear, but orientated at an angle which is proportional to  $z$ . In the following discussion, it is useful to think of an atomic orientation axis which is always parallel to the electric field. In this way, the light is always  $\pi$  polarised with respect to the atom, however the basis eigenfunctions are now (in the laboratory frame) a function of  $z$ . There is therefore no gradient in the light shifts of any atomic state. However, these light shifts are not equal for atoms with spin  $J_g \geq 1$ ; the Clebsch-Gordan coefficients are such that, with the laser tuned below resonance, the light shifts give the lowest  $|m_J|$  state the lowest energy, with the energy offset of the other states increasing monotonically with  $|m_J|$  ( $J = 1/2$  has equal light shifts due to symmetry).

We now need to consider optical pumping. The simplest atomic structure which can be cooled by this mechanism is an atom with  $J_g = 1$  (see Fig. 5.1(b)). It can be found by the principle of detailed balance that excitation of the  $J_g = 1 \rightarrow J_e = 2$  transition leads to a total steady-state population in the  $m_J = \pm 1$  levels that is less than the steady state population in the  $m_J = 0$  level (by a factor of 8/9 in this case).

Now we need to consider what happens when the atom moves. As we have chosen an atomic orientation basis which is a function of position, we see that, as the atom moves, the atomic state in the local basis must be different to that of the original basis. If, in the original basis, the atom is in the  $m_J = 0$  state, as the atom moves it smoothly mixes in the local  $m_J = \pm 1$  states. This therefore increases the expectation value of the atomic energy,  $\langle E_P \rangle$ , as the  $m_J = 0$  energy lies below the  $m_J = \pm 1$  energies.

In the semiclassical approximation, which is still a reasonable approximation at these energies (see Section 5.6 for a more detailed discussion), the force on the particle is proportional to the gradient of the expectation value of the potential energy. We can therefore see that there is a force which opposes the motion an atom which is initially in the  $m_J = 0$  state. The argument is closed by the observation that atoms are preferentially pumped to the  $m_J = 0$  state from the other states; it is therefore more probable that the force opposes the atomic velocity than otherwise, and the atomic sample is also polarisation gradient cooled by this laser configuration.

## 5.2 The mechanisms of polarisation gradient cooling of confined atoms

For atoms confined within a region which has linear dimensions of less than a wavelength, it is clear that the nature of these polarisation gradient cooling processes is modified. In this section we assume that the atoms are confined by an additional, off-resonant, optical lattice potential. It is important that this additional potential is far enough away from resonance that the scattering rate from this additional lattice potential is much less than the scattering rate from the cooling light. When this is the case, the additional potential only slightly changes the atomic internal eigenstates from what they would be if without this additional potential; we can then make the approximation that we can use the same internal eigenbasis as in free-space cooling. We also assume that this additional

lattice potential is state-independent (or nearly so). This is the case if the frequency detuning of the additional lattice is much greater than the width of the hyperfine structure of the excited state.

The additional lattice potential is characterised by its depth and phase with respect to the cooling light. In the case that the period of the additional optical lattice is different from  $\lambda/2$  of the cooling light, as is the case generally, this phase is a function of position.

### 5.2.1 Orthogonal linear polarisations

#### Effect of relative phase

The lin  $\perp$  lin configuration induces a state dependent lattice potential with period  $\lambda/2$ . The additional applied lattice potential may be in phase (Fig. 5.2(a)) or out of phase (Fig. 5.2(b)) with the lattice potential produced by the cooling light. These two situations lead to very different cooling properties, shall now be explained.

Let us define our axes so that the extra lattice potential has a minimum at  $z = 0$ . For the case of  $\phi = \pi/4$ , there will be equal intensities of  $\sigma^+$  and  $\sigma^-$  light at this point; however, the gradient of the intensities of the  $\sigma^+$  and  $\sigma^-$  light are equal and opposite. This means that the potential minima for  $m_J = \pm 1/2$  are equal in energy, but offset from each other in position (see Fig. 5.2(b)). For laser light negatively frequency detuned from atomic resonance, it can be seen that we still get optical pumping from the upper potential to the lower potential. For the case of  $\phi = \pi/4$ , the atoms can be polarisation gradient cooled reasonably efficiently at low energies, as the optical pumping direction reverses near the potential minima, meaning that multiple cooling cycles can be performed.

For the case of  $\phi = 0$ , however, the optical pumping changes sign half way up the lattice potential. This means that the majority of atoms always reside in the lower potential, and the first-order Sisyphus effect cannot cool low energy atoms. There is, however a less efficient cooling process. A double transition, from the lower ground-state potential to the upper ground-state potential and back again after a certain delay, will tend to cool the atoms. This is because the transition from the lower to the excited

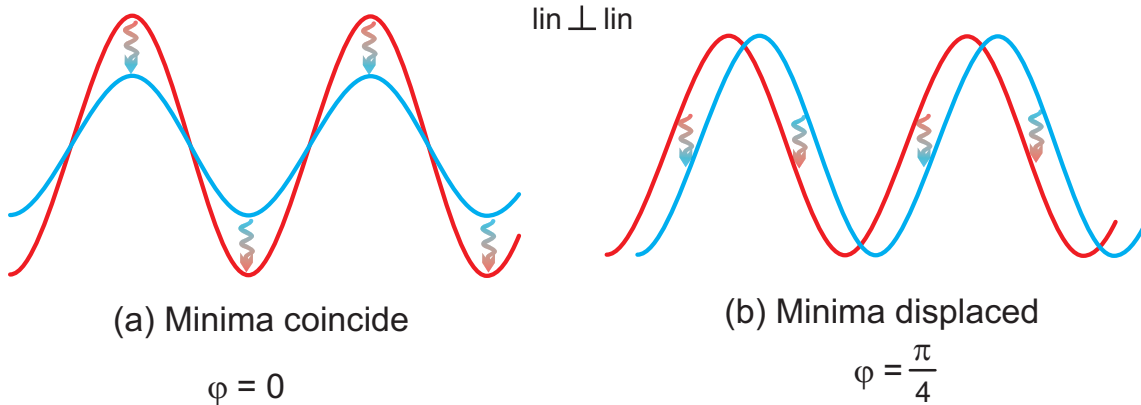


Figure 5.2: Polarisation gradient cooling of a confined  $J_g = 1/2$  atom with the lin  $\perp$  lin configuration. The curves cross and the optical pumping direction reverses at different energies depending on the phase of the molasses relative to the lattice. This affects the cooling efficiency of the confined atoms.

state will tend to happen at higher  $|z|$  than the reverse process, and potential energy will be lost over the complete cycle. Notice, however, that the potential energy lost is proportional to  $(kz)^2$  for low  $z$ ; this will be considerably less efficient for low energies than for the  $\phi = \pi/4$  case, in which the potential energy lost is proportional to  $kz$ . Furthermore the low rate of the optical pumping from the lower to upper sublevel in the  $\phi = 0$  case makes it relatively unlikely that an oscillating atom will perform a cooling cycle on any particular oscillation. One could describe the less efficient cooling of cool atoms for the  $\phi = 0$  configuration as a ‘second-order’ Sisyphus cooling effect.

### Effect of the frequent changes in direction

Another consideration is that we have another time scale in the situation, the period of the oscillation,  $1/\nu$ . The atom changes direction, and crosses  $z = 0$ , twice per oscillation. If the intensity of the cooling light is such that the optical pumping time is greater than half an oscillation, the atom cannot efficiently optically pump back to the lower energy state during the time that it is in the upper ground-state potential. The cooling efficiency therefore decreases substantially if the intensity of the laser beams are too weak. The decrease in heating from photon recoil does not compensate for the loss of cooling, and substantially higher temperatures will result; this behaviour can be seen in Figure 6.6. The point that this occurs depends on the frequency of the trap, but it is at substantially

higher intensities than the corresponding *décrochage* of polarisation gradient cooling of free space atoms.

This may be thought in terms of transient behaviour. The atom, at a certain position or velocity, will need a certain time for the internal state to relax to near its equilibrium state it is the equilibrium behaviour that we have used in the Section 5.1 to explain the processes of polarisation gradient cooling. It then follows that if the atom changes velocity or position again so that the equilibrium state is substantially different to the state it was previously relaxing to, before the transient behaviour has died down, the atom can never come to a equilibrium state that is local to its position or velocity, and the arguments we used in the Section 5.1 break down.

### 5.2.2 Orthogonal circular polarisations

The  $\sigma^+\sigma^-$  configuration, in one dimension, does not have the same issue with relative phases as the  $\text{lin} \perp \text{lin}$  configuration. The light shift from the molasses is the same everywhere; in fact a change in phase of the molasses is identical to a rotation of the axes; the physical system is the same for a purely one-dimensional potential<sup>1</sup>. This means that polarisation gradient cooling of confined atoms using the  $\sigma^+\sigma^-$  configuration does not depend on this relative phase, which is a substantial simplification of such an experimental arrangement. As with the  $\text{lin} \perp \text{lin}$  configuration, the optical pumping should occur on a time scale shorter than half the period of oscillation for efficient cooling.

### 5.3 Three-dimensional polarisation gradient cooling of confined atoms

The cooling schemes discussed in the previous sections still occur for atoms in 3 sets of counter-propagating laser beams. However, there are differences which significantly affect the cooling of confined atoms. The difference arises as there are necessarily both polarisation and intensity gradients of the cooling light for 3D molasses. The polarisation gradients will still lead to cooling, incorporating some mixture of the above two schemes [83].

---

<sup>1</sup>For 1D cooling of atoms in a 3D confining potential, there is in general a redistribution of the components of spontaneously emitted radiation in the orthogonal directions upon such a phase change, but the effect of this on the cooling dynamics is minor.

Tightly confined atoms only sample the light field in some small part of a cubic wavelength. Thus the intensity and direction of the cooling light that an atom sees varies with position, depending on the five relative phases of the molasses beams. This is a non-ideal situation for the cooling of confined atoms as the efficiency of the cooling in each of the three dimensions will be a strong function of position; while some atoms may be cooled very efficiently, others will be cooled only weakly. Furthermore different atoms at different positions within the molasses will fluoresce at different rates, which is an issue when the number of atoms at each original accordion lattice site need to be counted.

This issue can be dealt with in one of two ways. The way which will be developed is for the molasses beams to be incident along only one direction at a time; they then can be flashed in each direction in turn. Thus each direction is cooled sequentially. Another technique is to detune the molasses in the various directions from each other by some small frequency; the molasses character at any point will then be swept amongst a range of phases. This is the method used in experiments of Reference [4]. The merits of these two methods have been discussed in Section 4.7.1.

## **5.4 Simplification of the simulated system**

As with almost all real-world quantum phenomena, it is necessary to make certain assumptions to make the calculation tractable. This section describes some of these approximations, and more will follow in the course of the discussion.

### **5.4.1 The imaging lattice**

As has been described in Section 4.5, the atoms will be confined by the imaging lattice. This is a deep, tight lattice far enough from the optical resonance that spontaneous scattering from the imaging lattice is negligible compared to the scattering from the cooling light. Furthermore, it is a requirement that this light is linearly polarised.

These twin assumptions greatly simplify the effects of the imaging lattice on the quantum dynamics. With the assumption that the spontaneous scattering from the imaging lattice is negligible on the time scale of the cooling dynamics, the atomic states

in the absence of cooling light can be taken as the eigenstates of the atom in the field of the imaging lattice light. Furthermore, as the imaging lattice light is linearly polarised, the eigenstate of the atom in the field of the imaging lattice light contains only a single magnetic sublevel from the ground hyperfine state. This means that the ground-state sublevels are not coupled by atomic motion. In addition, as the lattice is far-detuned, motional coupling to the excited atomic states is negligible. This means that an atom in a certain eigenstate of the imaging lattice light will move adiabatically along the potential of that eigenstate.

Thus the imaging lattice is manifested as a diagonal, state-dependent potential, proportional to the intensity of the light

$$\mathbf{H}_{IL} = \mathbf{V}_0 \sin^2 kz , \quad (5.4)$$

where the diagonal matrix  $V_{ii}$  can be calculated for a state  $i$  from known parameters of the imaging lattice light and the properties of the atom<sup>2</sup>. A relation such as Equation 2.3 can be used, but for accuracy it is best to include the effect from the different hyperfine excited states separately, as these give very small state-dependent offsets to each of the ground-state sublevels. The origin has been chosen as a minimum of the lattice potential. As the three pairs of beams of the imaging lattice are frequency detuned from each other by many megahertz, the potential from the three-dimensional imaging lattice can be calculated as a sum of the 1D potentials.

As described above, the imaging lattice adds a slight admixture of excited states into each of the ground-state sublevels. In principle, this will alter the matrix elements of the cooling light between the ground and excited states. However, an application of one of the approximations that we have already used—that the amount of mixing of the excited state into the ground state is small enough that scattering from the imaging lattice is negligible—leads one to the conclusion that changes to the cooling transition amplitudes due to the dressing from the imaging lattice light can also be neglected. Thus the Clebsch-Gordon coefficients of the bare transition can, in this approximation, be used as the coupling coefficients of the states, as dressed by the imaging lattice.

---

<sup>2</sup>I shall keep, as far as possible, to the notation that a bold lower case symbol is a vector, and a bold upper case symbol is a matrix.

### 5.4.2 Restricting the number of participating states using repumping

The typical alkalis have non-zero nuclear spin and therefore two ground hyperfine states. The cooling should take place on a closed transition, i.e.  $|g, I + 1/2\rangle \rightarrow |e, I + 3/2\rangle$ . However, the atoms have a probability of being excited to the  $|e, I + 1/2\rangle$  state, which can decay to the lower hyperfine state  $|g, I - 1/2\rangle$ . The atoms will eventually be pumped to this dark state. This behaviour is prevented by the presence of ‘repumping’ light, i.e. light resonant with the  $|g, I - 1/2\rangle \rightarrow |e, I + 1/2\rangle$  transition. Furthermore, it is assumed that this repumping light is of sufficient power that the total residence time in the  $|g, I - 1/2\rangle$  state is only a few times the natural lifetime of the atom in the excited states. As a consequence there is an extremely small population of atoms in the lower hyperfine state at any one time. Furthermore, this means that the time spent in this state is much less than the period of vibration in the lattice, and therefore negligible heating of the atom will occur due to any difference in the imaging lattice potential between the two ground hyperfine states.

The repumping light is off-resonance by some gigahertz from the cooling transition  $|g, I + 1/2\rangle \rightarrow |e, I + 3/2\rangle$ , and as such will only have a very small effect on the dynamics of the atoms within those states. This is ignored in the subsequent analysis. The population of the  $|e, I + 1/2\rangle$  excited state is likewise ignored, as the population of this state is small, and atoms in this state decay on a time scale much smaller than the period of vibrational motion in the lattice.

## 5.5 Quantum description of polarisation gradient cooling

To describe the quantum system of the confined atom in the field of the confining light, it is most appropriate to split the processes into unitary processes (absorption and stimulated emission) and non-unitary processes (spontaneous emission).

### 5.5.1 Unitary quantum dynamics

From the above discussion it can be seen that the motion of atoms in the imaging lattice can be described by the matrix Hamiltonian

$$\mathbf{H}_{IL} = -\frac{\hbar^2 \mathbf{I}}{2m} \nabla^2 + \mathbf{V}_0 (\sin^2 kx + \sin^2 ky + \sin^2 kz) . \quad (5.5)$$

Here  $\mathbf{I}$  is the identity matrix acting on the internal states of the atom, and  $\mathbf{V}_0$  is the diagonal state-dependent potential. The state vector contains components describing the  $|g, I + 1/2\rangle$  and  $|e, I + 3/2\rangle$  states, so the state vector has a length of  $4I + 6$ . The unitary action of the cooling light is added in the rotating wave approximation, so the counter-rotating term can be eliminated; a change of variables used to eliminate the explicit time-dependence. The Hamiltonian describing the interaction of the atom with the cooling light reads

$$\mathbf{H}_{AL} = -\hbar \Delta \mathbf{P} + \frac{\hbar \Omega}{2} \sum_{\varepsilon=-1,0,1} (E_\varepsilon \mathbf{D}_\varepsilon^+ + E_\varepsilon^* \mathbf{D}_\varepsilon^-) . \quad (5.6)$$

In this equation, the matrices  $\mathbf{D}_\varepsilon^+$  ( $\mathbf{D}_\varepsilon^-$ ) are the dimensionless raising (lowering) operators, with coefficients given by the Clebsch-Gordon coefficients. These coefficients are normalised so that

$$\mathbf{P} = \sum_{\varepsilon=-1,0,1} \mathbf{D}_\varepsilon^+ \mathbf{D}_\varepsilon^- , \quad (5.7)$$

in which  $\mathbf{P}$  is the excited state projection operator. The electric field of the cooling light has components  $E_0$ ,  $E_1$  and  $E_{-1}$  in the  $\pi$ ,  $\sigma^+$  and  $\sigma^-$  directions respectively. The normalisations of  $E_\varepsilon$  and  $\Omega$  are taken so that  $E_\varepsilon = 1$  if all the electric field amplitude at a point  $\mathbf{r}$  is concentrated in component  $\varepsilon$ . The parameter  $\Omega$  is therefore the Rabi frequency at  $\mathbf{r}$  if all the electric fields added in phase at  $\mathbf{r}$ , and the Clebsch-Gordon coefficient of the transition equals unity<sup>3</sup>. In the situations under consideration  $\Omega$  is not a function of  $\mathbf{r}$ . The frequency detuning from resonance of the cooling light is  $\Delta$ . The total Hamiltonian describing the unitary evolution of the atomic state is therefore

$$\mathbf{H} = -\frac{\hbar^2 \mathbf{I}}{2m} \nabla^2 + \mathbf{V}_0 (\sin^2 kx + \sin^2 ky + \sin^2 kz) - \hbar \Delta \mathbf{P} + \frac{\hbar \Omega}{2} \sum_{\varepsilon=-1,0,1} (E_\varepsilon \mathbf{D}_\varepsilon^+ + E_\varepsilon^* \mathbf{D}_\varepsilon^-) . \quad (5.8)$$

<sup>3</sup>Note there are many conventions for the normalisation of these parameters in the literature.

The evolution of the density matrix  $\rho$  due to unitary processes obeys the von Neumann equation

$$i\hbar \frac{\partial}{\partial t} \rho = [H, \rho] . \quad (5.9)$$

### 5.5.2 Relaxation mechanisms of the internal states

In addition to the unitary evolution of the quantum state under the action of the Hamiltonian 5.8, there will also be relaxation processes from the excited states. These relaxation processes can be determined from a trace over the ‘environmental’ degrees of freedom of the corresponding unitary processes. In the internal degrees of freedom, the relaxation terms are [14]

$$\left( \frac{\partial}{\partial t} \rho \right)_{sp,int} = \Gamma \left( -\frac{1}{2} (\mathbf{P}\rho + \rho\mathbf{P}) + \sum_{\varepsilon=-1,0,1} \mathbf{D}_{\varepsilon}^{-} \rho \mathbf{D}_{\varepsilon}^{+} \right) . \quad (5.10)$$

The first term corresponds to the decay of the excited state; the second term corresponds to the receipt of these atoms by the ground state. Each term acts on both populations and coherences. These dynamics can be seen to be trace-preserving, as required.

This term does not yet take into account the effect of the photon recoil on the external degrees of freedom. To do this we must add the recoil momentum as exponential operators, and sum over all transitions and polarisations

$$\left( \frac{\partial}{\partial t} \rho \right)_{sp} = \Gamma \left( -\frac{1}{2} (\mathbf{P}\rho + \rho\mathbf{P}) + \sum_{\varepsilon, \varepsilon', \sigma} \int d^2\kappa e^{ik_{R\kappa} \cdot r'} \mathbf{D}_{\varepsilon}^{-} \rho \mathbf{D}_{\varepsilon'}^{+} e^{-ik_{R\kappa} \cdot r} f_{\varepsilon\varepsilon'}^{\sigma}(\kappa) \right) . \quad (5.11)$$

Here  $\kappa$  is a unit vector centred on the origin, and the parameter  $f_{\varepsilon\varepsilon'}^{\sigma}(\kappa)$  describes the angular distribution of the spontaneous emission in terms of the transitions  $\varepsilon$  and  $\varepsilon'$ , the polarisation  $\sigma$  and direction  $\kappa$ . The parameters  $f_{\varepsilon\varepsilon'}^{\sigma}(\kappa)$  are given in Appendix C.1.

### 5.5.3 Explicit retention of the excited states

In many analyses of polarisation gradient cooling [18, 32], at this point the excited states are adiabatically eliminated. This is appropriate for investigations that look to find the lowest temperature of atoms in optical molasses, which for free space occurs at low intensity; at low intensities, the population of the excited states is small, and adiabatic elimination is a good approximation.

However, as discussed in Section 5.2.1, the lowest temperatures of confined atoms occur at substantial optical power, when there is a significant population of the excited states. Therefore, the excited state populations must be retained in the analysis. The retention of the excited states leads to a corresponding slowdown in the computation, as the length of the state vector is increased, and as the highest frequency of the problem must now be taken as the laser frequency detuning (the highest frequency after adiabatic elimination is typically this frequency detuning multiplied by the saturation parameter, which is much less than one). This slowdown in the computation is one of the reasons, although not the foremost, that an extended form of the Monte Carlo technique needs to be used to extract the parameters of interest (see Sect. 5.10).

#### 5.5.4 The Wigner transformation

In anticipation of taking the semi-classical approximation, we would like to express the quantum dynamics of Equation 5.8 and 5.10 in terms of the Wigner function

$$W(\mathbf{r}, \mathbf{p}, t) = \frac{1}{h^3} \int d^3 \mathbf{u} \left\langle \mathbf{r} + \frac{\mathbf{u}}{2} \left| \rho \right| \mathbf{r} - \frac{\mathbf{u}}{2} \right\rangle e^{-i\mathbf{p}\cdot\mathbf{u}/\hbar} . \quad (5.12)$$

The transformation of the kinetic energy operator term is the same as in the standard derivation of the Wigner-Moyal equation [86, 62], which will not be reproduced here. The transformation of the potential energy operator proceeds using the position space representation of the Wigner transformation (Eqn. 5.12); in anticipation of future use we have not fully substituted for  $\rho$ . The result of the Wigner transformation of the unitary dynamics (Equation 5.8) is therefore

$$\left( \frac{\partial}{\partial t} + \frac{\mathbf{p}}{m} \cdot \nabla \right) W(\mathbf{r}, \mathbf{p}, t) = \frac{2\pi i}{h^4} \int d^3 s e^{i\mathbf{p}\cdot\mathbf{s}/\hbar} \left[ \rho \left( \mathbf{r} + \frac{\mathbf{s}}{2}, \mathbf{r} - \frac{\mathbf{s}}{2}, t \right) V \left( \mathbf{r} - \frac{\mathbf{s}}{2} \right) - V \left( \mathbf{r} + \frac{\mathbf{s}}{2} \right) \rho \left( \mathbf{r} + \frac{\mathbf{s}}{2}, \mathbf{r} - \frac{\mathbf{s}}{2}, t \right) \right] \quad (5.13)$$

where

$$V(\mathbf{r}) = \mathbf{H} + \frac{\hbar^2 \mathbf{I}}{2m} \nabla^2 . \quad (5.14)$$

The Hamiltonian  $\mathbf{H}$  is given by Equation 5.8.

The Wigner transformation of the internal dynamics (Equation 5.11) is shown in Appendix C.3 to be

$$\left(\frac{\partial}{\partial t}\mathbf{W}\right)_{sp} = \Gamma \left( -\frac{1}{2}(\mathbf{PW} + \mathbf{WP}) + \sum_{\varepsilon, \varepsilon', \sigma} \int d^2\kappa \mathbf{D}_{\varepsilon}^{-} \mathbf{W}(\mathbf{r}, \mathbf{p} - \hbar k_R \boldsymbol{\kappa}, t) \mathbf{D}_{\varepsilon'}^{+} f_{\varepsilon \varepsilon'}^{\sigma}(\boldsymbol{\kappa}) \right). \quad (5.15)$$

The complete quantum description of the dynamics in terms of the Wigner function is therefore

$$\begin{aligned} \left(\frac{\partial}{\partial t} + \frac{\mathbf{p}}{m} \cdot \nabla\right) \mathbf{W}(\mathbf{r}, \mathbf{p}, t) = & \quad (5.16) \\ & \frac{2\pi i}{h^4} \int d^3 s e^{i\mathbf{p} \cdot \mathbf{s} / \hbar} \left[ \boldsymbol{\rho}\left(\mathbf{r} + \frac{\mathbf{s}}{2}, \mathbf{r} - \frac{\mathbf{s}}{2}, t\right) V\left(\mathbf{r} - \frac{\mathbf{s}}{2}\right) - V\left(\mathbf{r} + \frac{\mathbf{s}}{2}\right) \boldsymbol{\rho}\left(\mathbf{r} + \frac{\mathbf{s}}{2}, \mathbf{r} - \frac{\mathbf{s}}{2}, t\right) \right] \\ & - \frac{\Gamma}{2}(\mathbf{PW} + \mathbf{WP}) + \Gamma \sum_{\varepsilon, \varepsilon', \sigma} \int d^2\kappa \mathbf{D}_{\varepsilon}^{-} \mathbf{W}(\mathbf{r}, \mathbf{p} + \hbar k_R \boldsymbol{\kappa}, t) \mathbf{D}_{\varepsilon'}^{+} f_{\varepsilon \varepsilon'}^{\sigma}(\boldsymbol{\kappa}). \end{aligned}$$

## 5.6 The semi-classical approximation

The full quantum treatment of the problem is very involved; instead, the semi-classical approximation will be used. The form of the semi-classical approximation used is here is that any change in the Wigner function at a certain momentum and position can only be influenced the Wigner functions in the immediate proximity of this point in phase space. Stated in another way, we must recast the equations of motion in a more local form.

This is a good approximation when the width of the ensemble momentum distribution is much greater than the width of the Fourier transform of the potential terms of the quantum Hamiltonian. In the case we are considering here, the Fourier transform of the Hamiltonian is peaked around the recoil momentum. Therefore the semi-classical approximation is appropriate when the typical atomic momentum is much greater than momentum of a single photon recoil. This approximation seems appropriate as it is the highest energies we are most interested in—when the atoms jump from one well to another. The imaging lattice will be of the order of  $10^3$  recoil energies deep.

From the above argument it follows that the potential term on the right hand side of Equation 5.16 should be expanded in a Taylor series around  $\mathbf{r}$

$$V(\mathbf{r} + \mathbf{s}') = V(\mathbf{r}) + \mathbf{s}' \cdot \nabla V(\mathbf{r}) + \frac{1}{2} (\mathbf{s}' \cdot \nabla)^2 V(\mathbf{r}) + \dots \quad (5.17)$$

Low orders of the expansion characterise the behaviour of the Wigner function in the vicinity of  $\mathbf{r}$  and  $\mathbf{p}$ ; higher orders of expansion are only needed to describe the Wigner function outside the immediate region of phase space. Therefore, to make the equation of phase space evolution classical, we terminate such expansion at an appropriate small order to keep only the most local dynamical effects. This can be shown to be equivalent to expanding in orders of  $\hbar$  [86], which is assumed to be a small parameter in the semiclassical approximation.

It can be shown (Appendix C.2) that, in this way, we arrive at the equation

$$\begin{aligned} \left( \frac{\partial}{\partial t} + \frac{\mathbf{p}}{m} \cdot \nabla \right) \mathbf{W} &= \frac{i}{\hbar} [\mathbf{W}, \mathbf{V}] + \frac{1}{2} \sum_i \left\{ \frac{\partial \mathbf{W}}{\partial p_i}, \frac{\partial \mathbf{V}}{\partial r_i} \right\} \\ &- \frac{i\hbar}{8} \sum_{ij} \left[ \frac{\partial^2 \mathbf{W}}{\partial p_i \partial p_j}, \frac{\partial^2 \mathbf{V}}{\partial r_i \partial r_j} \right] + \Gamma \sum_{\varepsilon} \mathbf{D}_{\varepsilon}^{-} \mathbf{W} \mathbf{D}_{\varepsilon}^{+} \\ &- \frac{\Gamma}{2} (\mathbf{P} \mathbf{W} + \mathbf{W} \mathbf{P}) + \frac{\Gamma \hbar^2 k_R^2}{2} \sum_{\varepsilon, \varepsilon', i, j} \eta_{\varepsilon \varepsilon' ij} \mathbf{D}_{\varepsilon}^{-} \frac{\partial^2 \mathbf{W}}{\partial p_i \partial p_j} \mathbf{D}_{\varepsilon'}^{+}. \end{aligned} \quad (5.18)$$

In this equation, the curly brackets are the anti-commutator, and the tensor  $\eta_{\varepsilon \varepsilon' ij}$  is given in Appendix C.1.

If the trace is taken over the internal states and the recoil momentum is set to zero, we find that, as desired, we have the Liouville equation describing classical phase space evolution

$$\frac{\partial}{\partial t} \rho = \sum_i \left( \frac{\partial \rho}{\partial p_i} \frac{\partial H_C}{\partial r_i} - \frac{\partial \rho}{\partial r_i} \frac{\partial H_C}{\partial p_i} \right) \quad (5.19)$$

with

$$H_C = \frac{\mathbf{p}^2}{2m} + \text{Tr}_I \mathbf{V}. \quad (5.20)$$

## 5.7 Conversion to Langevin form

The semiclassical evolution equation as it stands (5.18) still requires substantial computational power to simulate the entire distribution. Therefore we will restrict ourselves to the evolution of a single trajectory; the distribution is then found as the sum over these trajectories. As the evolution is stochastic, the form of our simulation is Monte Carlo.

We first look for a specific trajectory in position and momentum space. By

substituting a trial solution<sup>4</sup>

$$\mathbf{W}(\mathbf{r}, \mathbf{p}, t) = \mathbf{w}(t) \delta^{(3)}(\mathbf{r} - \tilde{\mathbf{r}}) \delta^{(3)}(\mathbf{p} - \tilde{\mathbf{p}}), \quad (5.21)$$

into Equation 5.18, we can find evolution equations for  $\tilde{\mathbf{r}} = \langle \mathbf{r} \rangle$ ,  $\tilde{\mathbf{p}} = \langle \mathbf{p} \rangle$  as a combination of drift and diffusion terms.

Inserting Equation 5.21 into Equation 5.18 and integrating over external co-ordinates gives the equation of evolution for the internal co-ordinates

$$\frac{\partial}{\partial t} \mathbf{w} = \frac{i}{\hbar} [\mathbf{w}, V(\mathbf{r})] + \Gamma \left( -\frac{1}{2} (\mathbf{P}\mathbf{w} + \mathbf{w}\mathbf{P}) + \sum_{\varepsilon} \mathbf{D}_{\varepsilon}^{-} \rho \mathbf{D}_{\varepsilon}^{+} \right). \quad (5.22)$$

The equation of evolution of the external co-ordinates, e.g.  $\tilde{\mathbf{r}} = \langle \mathbf{r} \rangle$ , are found by integration over the internal and external co-ordinates to be

$$\frac{\partial \tilde{r}_i}{\partial t} = \frac{\tilde{p}_i}{m} \quad (5.23)$$

$$\frac{\partial \tilde{p}_i}{\partial t} = f_i = -\text{Tr}_I \left( \mathbf{w} \frac{\partial V}{\partial r_i} \right) \quad (5.24)$$

$$\frac{\partial}{\partial t} \langle (r_i - \tilde{r}_i)(r_j - \tilde{r}_j) \rangle = 0 \quad (5.25)$$

$$\frac{\partial}{\partial t} \langle (p_i - \tilde{p}_i)(p_j - \tilde{p}_j) \rangle = 2D_{ij} = \hbar^2 k_R^2 \Gamma \frac{1 + \delta_{ij}}{2} \sum_{\varepsilon, \varepsilon'} \eta_{\varepsilon \varepsilon' ij} \text{Tr}_I (\mathbf{D}_{\varepsilon}^{-} \mathbf{w} \mathbf{D}_{\varepsilon'}^{+}) \quad (5.26)$$

The  $D_{ij}$  term<sup>5</sup> describes the diffusion of the atom due to the atomic recoil. It is a fluctuating Langevin force with zero mean, and can be incorporated into the motion of a single trajectory in the Itô-Langevin equation

$$dp_i = f_i dt + \sum_k \sqrt{2d_{ik}} dW_k \quad (5.27)$$

in which  $dW_j$  are independent, zero mean, Gaussian-distributed stochastic increments with variance  $dt$ . The quantities  $d_{ik}$  are the components of the  $k$ th eigenvector of  $D_{ij}$ , which is normalised according to its eigenvalue.

<sup>4</sup>Equation 5.21 only makes sense in the semiclassical approximation.

<sup>5</sup>There is potential for the conflict of the standard notations; in this thesis  $\mathbf{D}_{\varepsilon}^{\pm}$ , in bold font with a superscript, will denote the atomic dipole raising and lowering matrices, while  $D_{ij}$ , in normal font with no superscript, will denote the diffusion matrix.

## 5.8 Unravelling the Optical Bloch equations

The equations 5.23 to 5.27 describe the motion of a single atom in the semi-classical approximation. However, the internal dynamics as described in 5.21 still average the atomic evolution over an ensemble, and so are not appropriate to describe a single trajectory. We must therefore unravel the optical Bloch equation 5.21 into the stochastic evolution of a single wave function.

The unravelling is chosen to be that of the quantum Monte Carlo wave function method (QMCW) [70]. The underlying principle of the approach is to evolve the wave function using a non-Hermitian quasi-Hamiltonian with the addition of randomly-occurring discrete quantum jump processes. As relevant to the problem at hand, the method boils down to the following procedure for each time step. Firstly, a random number is compared to the quantity

$$j = 1 - \Gamma \delta t \langle \psi | \mathbf{P} | \psi \rangle . \quad (5.28)$$

If the random number is less than this quantity, the atom has not performed a quantum jump. In this case the wave function is evolved using the evolution operator

$$|\psi(t + \delta t)\rangle = |\psi(t)\rangle - \frac{i}{\hbar} \delta t \mathbf{H}' |\psi\rangle \quad (5.29)$$

where  $\mathbf{H}'$  is the non-Hermitian operator

$$\mathbf{H}' = \mathbf{V} - \frac{i\hbar\Gamma}{2} \mathbf{P} . \quad (5.30)$$

If the random number is more than the quantity  $j$ , the atom undergoes a quantum jump. The nature of this jump is determined by selecting the photon polarisation by the weights

$$p_\varepsilon = \frac{\langle \psi | \mathbf{D}_\varepsilon^+ \mathbf{D}_\varepsilon^- | \psi \rangle}{\langle \psi | \mathbf{P} | \psi \rangle} \quad (5.31)$$

and the new wave function is given by

$$|\psi(t + \delta t)\rangle = \mathbf{D}_\varepsilon^- |\psi(t)\rangle . \quad (5.32)$$

The resulting wave function  $|\psi(t + \delta t)\rangle$  is not normalised in either case, and requires normalisation before further operations are performed. It can be shown that the Equations 5.28 to 5.32 satisfy the Bloch equation (Eqn. 5.22)—see Appendix C.5 for details.

### 5.8.1 Continuous and discrete recoil momentum terms

The quantum Monte Carlo wave function method suggests another way of determining the atomic recoil term, in contrast to Equation 5.26. The QMCW method gives the times and nature of the quantum jumps, and given the angular distribution of the photon momenta, a direction of photon recoil could be picked. Thus the photon recoil would happen at discrete time intervals, instead in a continuous diffusion process. This can be derived from the above analysis by not expanding the photon recoil term of Equation 5.16, then interpreting the recoil term in the unravelling of the optical Bloch equations.

Since, in making the semi-classical approximation, we are already expanding the other parts of Equation 5.16 in terms of small momenta which are about the magnitude of the recoil momentum, it is not expected that keeping the recoil term discrete would make the simulation more accurate. Instead, the two ways to incorporate the recoil momentum could be seen as different forms of the semiclassical approximation. The continuous diffusion form has been used in this simulation, as a momentum which varies continuously is somewhat simpler to deal with when using the extended form of the Monte Carlo technique (Sect. 5.11).

## 5.9 Computational methods

The set of equations 5.23 to 5.26 and 5.28 to 5.32 therefore specify the stochastic evolution of a single semiclassical trajectory; some of the details concerning how the state vector is propagated are now outlined. An explicit third-order Runge-Kutta method is used to propagate the position and momentum components. The coefficients for the method are chosen so that the intermediate evaluation times are  $h/3$  and  $2h/3$ , in which  $h$  is the time step. The internal components of the state vector then can then be advanced at a constant time step  $h/3$ .

For the internal evolution, a method was chosen which conserves the norm of wave functions under Hermitian Hamiltonian evolution; this has somewhat more accuracy than a Runge-Kutta method for the problem at hand. The method uses the Cayley

form of the evolution operator:

$$\left(\mathbf{I} + \frac{i \delta t}{2\hbar} \mathbf{H}'\right) |\psi(t + \delta t)\rangle = \left(\mathbf{I} - \frac{i \delta t}{2\hbar} \mathbf{H}'\right) |\psi(t)\rangle. \quad (5.33)$$

The new wave function can be found efficiently by Gaussian elimination.

### 5.10 Comment on nature of the simulation

The problem under consideration differs from previous analyses of polarisation gradient cooling (e.g. [18, 96]) in a number of respects. The difference which poses the greatest computational challenge is the ratio of the time scales in the problem—between the phenomena that we are interested in, the jumping of atoms between wells, which we would like to take place over tens of seconds or greater; and the smallest time scale relevant to the problem, the period of the beat frequency between the laser and atomic resonance, which will be in the range of 5 – 50 nanoseconds. This means that, on average, one event of interest will occur every  $10^{10}$ - $10^{13}$  time steps. Clearly a straightforward Monte Carlo simulation of these phenomena will be prohibitively slow.

Adiabatic elimination is often used in simulations of polarisation gradient cooling in order to increase the size of the smallest time step (and decrease the size of the state vector). However, this technique can only be used when the saturation parameter is much less than 1, which is not the case for the situations that we wish to simulate (see Sect. 5.5.3). In any case, the gain from this technique would be, at most, two orders of magnitude in the time scale ratio, i.e. interesting events would occur every  $10^8$ - $10^{11}$  time steps; such calculations would still be very computationally intensive.

### 5.11 Extended Monte Carlo analysis

In order to be make the simulation tractable it is necessary to find a Monte Carlo method that is appropriate to studying rare events. This section outlines a method which I have developed for this task by extending the standard Monte Carlo analysis. Although developed for the problem at hand, the method is potentially applicable to Monte Carlo simulations of other systems and as such, it will be described in a system-independent way. Although developed independently, and as far as I know novel in its use for ul-

tracold physical systems, this technique is identical in various respects to previously developed techniques which are collectively known as the ‘splitting’ methods of Monte Carlo simulation [57, 97, 24, 27].

At heart, the idea is to approximately map the non-Markovian system onto a continuous-time Markov process. The analysis as outlined in this section is not designed to be an exact method, but rather is designed to provide an accurate extrapolation of the Monte Carlo dynamics throughout all the regions of interest in phase space. The accuracy of the method was tested both by consistency checking, i.e. making sure that completely different iterations of the simulation produced very similar answers, and by checking this form of extended Monte Carlo simulation against known data (see Section 6.3).

### 5.11.1 The ‘measure’ and ‘events’

Firstly, a quantity should be found that is representative of the aspect of the problem that we are interested in. This ‘measure’ (symbol  $E$ ) is a scalar quantity which is a function of the state vector, and is chosen so that it has two properties in particular:

- The measure  $E(t) \equiv E(\{\phi(t)\})$  varies with time as slowly and as smoothly as possible, i.e. the frequency and size of any discontinuous jumps are as small as possible.
- The system spends most of its time in the region  $E_\alpha < E(t) < E_\beta$ ; however, the events of interest occur exclusively in the region  $E_\gamma < E(t) < E_\delta$ ; these two regions are distinct from each other ( $E_\beta < E_\gamma$  or  $E_\delta < E_\alpha$ ).

The variables  $\{\phi\}$  which describe the state of the system at a point in time could take discrete or continuous values. Although for the subsequent analysis it will be assumed that these variables are all continuous, similar arguments may be developed for sets of discrete variables (or mixtures of the two). The system at a specific point in time has the representation  $\{\phi(t)\}$ , the state vector. In the subsequent analysis it is assumed that the system under consideration is ergodic.

The success with which an appropriate measure can be found will largely determine whether or not this extended form of Monte Carlo analysis will be useful.

Let us now define a set of points along the measure,  $\{E_1, E_2, \dots\}$ , which cover the above regions ( $E_\alpha$  etc.) and the region in between. As a result of time propagation, which we simulate using a standard Monte Carlo method, the system will encounter these points repeatedly as the system evolves<sup>6</sup>. Each time the system encounters one of these points, let us call it an ‘event’. The state vector when events occur will be called ‘start vectors’ for reasons that will become clear.

### 5.11.2 System dynamics when representative start vectors are known

Let us now assume that a representative set of start vectors are known for each point  $E_i$ ; how this can be achieved is discussed in subsequent sections. If we have this representative set, the system dynamics can be found relatively easily over the entire range that we are interested in, albeit under certain approximations.

We assume that we propagate some or all of these representative start vectors until a new event is reached; the index of the new event, and the time elapsed, are recorded. By repeating this multiple times, with separate runs of the simulation for each start vector, and across all start vectors and events, a comprehensive picture will emerge of the system dynamics.

If the measure  $E$  has been chosen so that it varies continuously or undergoes only very local jumps, the number of these runs needed to characterise each starting vector and point is very much reduced, as there are only two possible events that could occur next for every start vector.

With this data, the simplest way forward would be to now make a Markovian approximation; in other words, having generated the data, we assume at this point that the set of state vectors at each point is well labelled by the single quantity  $E$ . Average rates can then be calculated for each point, and the dynamics can be described by a simple matrix equation (see Section 5.12). It is possible to avoid the full Markovian approximation by running a further, simpler, simulation with the data already gathered. This is discussed in Section 5.12.

---

<sup>6</sup>If the state vector of the system undergoes discontinuous jumps, the time and state vector of the system as it crosses a point may need to be extrapolated or approximated. If the number of these extrapolations is too great, then the accuracy of this type of analysis will decrease.

A method to find a set of representative start vectors for each point is now discussed.

### 5.11.3 Finding representative start vectors

A set of start vectors can be said to be representative if it fairly samples the true population of start vectors for a particular point  $E_i$ . If we imagine the population of start vectors for a particular point to occupy a certain volume of phase space, the sample of start vectors should adequately fill that volume, with the density of the sample and the true population being approximately proportional.

However, we also wish to minimise the run time of the Monte Carlo simulations. As some events occur only very rarely, it would be prohibitive to find this sample for all points by means of direct Monte Carlo simulation. We seek a method to balance these two considerations.

As a first stage, let us imagine that we let the simulation run freely from some arbitrary starting point. After a certain length of time we assume that the system settles down into something like its steady state, i.e. well chosen time-averaged quantities tend towards certain values, albeit with fluctuations; these values are independent of the arbitrary starting point. From this time on let us record the state vector every time an event occurs, i.e. every time  $E(t) = \{E_1, E_2, \dots\}$ . Over time, and perhaps over different runs, a representative set of start vectors will be built up for those points in the region  $E_\alpha < E(t) < E_\beta$ , where the system spends most of its time.

We now need to look to extend this coverage to points  $E_i$  which are outside this limited region. To do this we assign a weight  $w_{ni}$  to each start vector, which is in effect an estimate of how representative that start vector is of the general population of start vectors (at all points). After the initial run(s), we can assign an equal weight to each of the start vectors we already have, irrespective of the point they are associated with, as we assume each is equally representative of the general population of start vectors. We can normalise the weights, conveniently

$$\sum_{n,i} w_{ni} = 1 \quad (5.34)$$

where  $i$  represents the point index, and  $n$  labels the particular start vector at that point. The total weight of the start vectors at a particular point

$$W_i = \sum_n w_{ni} \quad (5.35)$$

is related, but not equal, to the probability of finding the steady state system in the environs of point  $i$ .

### **Representative start vectors for a point and between points**

At this stage a subtlety will be outlined which I have encountered while running the simulation. We are looking for the initial set of start vectors to be representative in two ways: firstly that the set of start vectors at each point is representative of the population of start vectors at that particular point, and secondly that the total number of start vectors at a point is representative of how the start vectors are distributed between the points. Unfortunately this is a little contradictory. If we use the above method to generate a set of start vectors, at the edge of the frequented region ( $E_\alpha$  or  $E_\beta$ ) there is likely to be at least one point which is initially populated by only a few start vectors; this will be too few to be an accurate representation of the start vectors at that point.

Retaining these particular start vectors with a full weight tends to decrease the stability of the simulation. My solution was to select a lower bound on the number of initial start vectors that were allowed at any point (about 100) by setting the all the weights of the start vectors to zero at any point with less than this minimum number. Consequently the initial distribution of start vectors between points is not quite representative (by a couple of percent in my case); however, this error is small, and tends to be corrected over time as the start point distribution equilibrates. The benefits of this procedure were found to outweigh the disadvantages for the calculations performed in this thesis. More sophisticated treatments would also be possible, for example by allocating lower but non-zero weights to these particular start vectors.

#### **5.11.4 Several daughters vectors per mother vector**

We now need to find new representative start vectors from those we already have. To do this, consider that a starting vector is picked at random from all the possible start vectors, and is evolved in time until a new event is reached. As we are assuming that the system is ergodic, we can replace the old ('mother') start vector with the new ('daughter') start vector (by assigning the mother start vector's original weight to the daughter and setting the mother's weight to zero), and the overall set of start vectors is still representative of the steady state dynamics of the system.

This in itself is not that helpful, because as this process is repeated, the start vectors will still cluster around the most frequented region. Instead, we wish to find a method which gives a start vector for every possible daughter point which can be reached in one step from a mother vector; in this way the spread of available start vectors is increased as the simulation progresses. To do this, the mother vector is propagated multiple times until all possible daughter points have been reached (only two, if the measure varies continuously in time). We can find a daughter start vector for each of the possible daughter points by random choice among the possibilities that have been found. To find the appropriate weights, enough data should be taken to have a good estimate of the branching probabilities amongst the possible daughter points, and the most representative way to include these new points in the overall set is to divide the mother starting vector's weight amongst these daughter vectors according to the branching ratio (again the mother start vector weight is set to zero).

As the start vectors are iteratively propagated using this method, with the mother start vector randomly chosen by weight, new start vectors are found from the old start vectors. Furthermore, this process is already gathering the data needed for the third part of this simulation process (see Sect. 5.11.2).

The above method, while always acting to increase the spread of start vectors amongst the points, will still lead to most simulation time being spend in the most frequented part of the measure, as the total weight at the points will decrease as the distance along the measure increases. However, we are now in a position in which it is possible to simply simulate the dynamics in the more frequented, known region, in order to con-

centrate the simulation on the less frequented areas; this process is described in the next section.

### 5.11.5 Focussing the analysis on less frequented regions

The number of points  $E_i$  for which there are starting vectors is continuously expanded using the above method. Once we have propagated  $M$  of these mother vectors for a particular point  $E_M$ , we decide that we have gathered enough data to characterise the behaviour of the system around this point. The start vectors at point  $E_M$  are then excluded from being propagated further using the Monte Carlo method; we shall call these points ‘full’ to indicate that we have carried out the maximum number of runs  $M_{max}$  that we are interested from any one point. The choice of mother vector for propagation now determined from the weights of all the start vectors at all points which are not full.

Although there is no need to generate further daughter vectors from this point, weight is still added to this point from neighbouring points which are partially filled; if this goes uncompensated, it will lead to the distortion of the weights between the points, because if the full points were only partially filled, some weight would flow in the other direction. So in lieu of the Monte Carlo propagation, these full points are propagated using a much simpler method. An approximation is made in which we replace the list of starting vectors and weights for that point with a single weight  $W_M$ , representative of the total population of starting vectors at this point  $E_M$ . At this stage it is necessary to use the data which has already been gathered for that point. For the sake of simplicity I will assume that we make an Markovian approximation for this data<sup>7</sup>, although more sophisticated treatments are possible (see Sects. 5.11.2 and 5.12). This Markovian approximation allows a probability to be assigned for a typical start vector at  $E_M$  to go to  $E_{M-1}$  ( $p_d$ ) or  $E_{M+1}$  ( $p_u$ ).

The next start vector for propagation is chosen according to its weight  $w_{mth}$  from all the points  $E_i \neq E_M$ ; the combined weight of the start vectors that we choose from is  $W_N = 1 - W_M$ . We then propagate  $W_M$  to account for all the start vectors we are ignoring

<sup>7</sup>This Markovian approximation is taken *only* for points which already have the required number of propagated mother vectors; this propagation has been carried out using the standard Monte Carlo method, which is *not* a Markov process of the single parameter  $E$ .

at  $E_M$ . Without  $E_M$  being full, the probability of choosing a start vector from  $E_M$  would be  $W_M$ , or from outside  $W_N$ ; therefore, as  $E_M$  is full, the average weight we need to reallocate from  $E_M$  is  $w_{mth}W_M/W_N$ . This weight is reallocated from  $E_M$  to those daughter vectors in  $E_{M-1}$  and  $E_{M+1}$  with a mother vector in  $E_M$ ; this weight is allocated according to  $p_d$ ,  $p_u$ , and proportional to the weight of each daughter vector. We have therefore accounted for any flow of weight from the between the full and partially filled regions.

This procedure only differs slightly when more than one point is full. When these points are non-consecutive, we reallocate  $w_{mth}W_M/W_N$ ,  $w_{mth}W_{M'}/W_N$  etc. to each of the daughters of these points; when these points are consecutive we reallocate the appropriate weight  $w_{mth}W_M/W_N$  to the total weights of the full neighbours, according to  $p_u$  and  $p_d$ .

It can now be seen that we eliminate the most common points  $E_\alpha < E_i < E_\beta$  from the Monte Carlo analysis, in favour of points in the less frequented regions of the measure. As this continues, points along the entire measure will be eventually be characterised, including the regions that we are interested in.

### 5.11.6 The choice of points on the measure

At this point it is worth reconsidering how one would choose the spacing of points on the measure. The simulation time will increase the significantly further apart the point are, as the time taken to go from one point to another increases by more than a linear power (c.f. diffusive processes, which have  $\Delta t \propto \Delta x^2$ ), and furthermore the number of runs to needed characterise the path of each start vector increases due to the increased influence of the drift term (which makes the difference between the branching probabilities greater). However, if the points are too close together, the number of start vectors needed to characterise each point grows substantially. This is because, as the points get closer, the diffusion of the start vectors gets less as they are propagated between points, therefore more starting points are needed to characterise the processes present in that region of phase space. One sign that there is not enough space between points, or that there are not enough start vectors being propagated for each point, is that clusters of points start to develop the further along the measure the simulation is extrapolated.

These considerations mean that there are an optimal number of start points; in the simulation performed in this thesis, this was determined in practice by checking for phase space clustering at the points furthest from the most frequented region, by checking the consistency of the simulation upon repetition, and by checking the results of the simulation against known data.

### 5.11.7 Extended Monte Carlo simulation: summary

1. (a) In the first part of the process, one or more initial standard Monte Carlo simulations are carried out. After the system settles into a steady state, the state vectors are recorded every time there is an event; these form the initial population of start vectors for the extended simulation.
- (b) An equal weight is assigned to each of the initial start vectors at well populated points; start vectors from poorly populated points are ignored.
2. (a) A single start vector (the mother) is chosen randomly from the set of all the eligible start vectors, i.e. those start vectors at partially filled points  $E_i$  (combined weight  $W_N$ ), with a probability which is proportional to the start vector's weight  $w_{mth}$ .
- (b) The (mother) start vector is propagated by Monte Carlo propagation until the next event is reached; this is performed multiple times. The resulting state vectors (the daughters) are categorised by point, and a single daughter vector is saved for each point. The branching probabilities  $p_i$  for that particular start vector are calculated.
- (c) Weights are assigned to the mother and daughter vectors according to  $w_{mth} = 0$  and  $(w_{dt})_i = p_i w_{mth}$ .
- (d) New weights are assigned to each full point (weight  $W_M$ ) as

$$(W_M)_{new} = W_M - \frac{w_{mth} W_M}{W_N}. \quad (5.36)$$

- (e) New weights are assigned from the full point (weight  $W_M$ ) to full point

(weight  $W_{M'}$ ) as

$$(W_{M'})_{new} = W_{M'} + \frac{p_{M'M} w_{mth} W_M}{W_N}. \quad (5.37)$$

where  $p_{M'M}$  are the calculated mean branching ratios from  $M$  to  $M'$ .

- (f) New weights are assigned from the full point (weight  $W_M$ ) to its daughter vectors at partially filled points (weights  $w_{dtM}$ ) as

$$(w_{dtM})_{new} = w_{dtM} + \frac{p_{m'M} w_{mth} W_M}{W_N} \frac{w_{dtM}}{\sum w_{dtM}} \quad (5.38)$$

where the summation  $\sum w_{dtM}$  runs over all the daughter vectors of the point with weight  $W_M$  at this partially filled point, and  $p_{m'M}$  are the calculated mean branching ratios from  $M$  to  $m'$ .

- (g) If the number of start vectors propagated per point reaches the maximum allowed  $M_{max}$ , the weights of all start vectors at this point are summed to give  $W_M$ , and from the collected data, the mean branching ratios  $p_{m'M}$  are found for all relevant channels.
- (h) Part 2 is repeated until data has been taken for all  $E_i$  of interest.

3. In the third part of this simulation process, the results of the second part are processed, either by use of matrix master equations or a further Monte Carlo simulation. See section 5.12.

Figure 5.3 is a pictorial representation of one step of this technique.

This method yields data on the populations and transfer rates in rarely frequented regions of the measure, and provides a set of representative state vectors for this region. These starting vectors may be analysed to study effects which only occur when the system is in this region (the hopping dynamics of the motivative example).

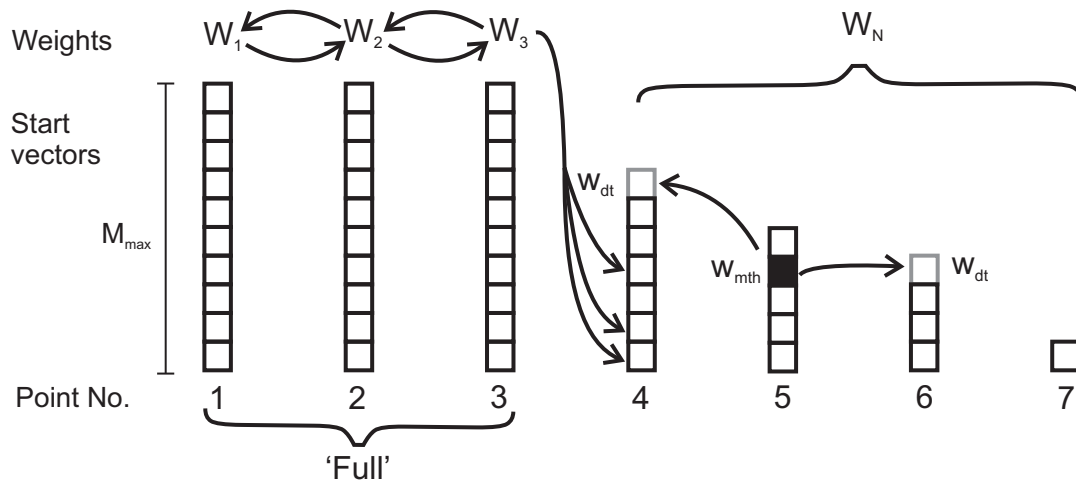


Figure 5.3: Schematic depicting the steps surrounding the analysis of a single start vector in the extended Monte Carlo method. The the open black boxes represent starting vectors; the filled box the current starting vector (the mother), which is evolved multiple times until the next event. The daughter state vectors produced, depicted by the open grey boxes, are saved, and the weights are reallocated along the arrows according to the equations of Section 5.11.7.

## 5.12 Markovian and non-Markovian analyses

### 5.12.1 Markovian probability analysis

The Markovian analysis takes the results of the simulation so far and assigns average probabilities and rates for the system to hop from this point to other points. It is important to emphasise that the processes we are simulating are, by their very nature, not Markovian processes of a single variable; previously in the simulation process we have where possible minimised the use of Markovian approximations<sup>8</sup>. Now that we have a set of representative start vectors, and branching probabilities for each start vector, the approximation can be made that the start vectors at each point form a representative group, with a single label, and their individual behaviour can be averaged across the group.

If each mother start vector was propagated a variable number of times, care should be taken to ensure that selection bias does not affect the assigned branching probability for that start vector. A suitable way would be to reduce the number of propa-

<sup>8</sup>Only used when propagating the weights of the full points, which only affects the selection of start vectors; not used in the standard Monte Carlo propagation.

gation outcomes used in the calculation for each mother vector to  $n_{min}$ , which is the minimum number of times any mother vector was propagated (at that point). Mother-vector branching probabilities should be combined into (mean) point branching probabilities by using the appropriate weight of the mother vector at time of propagation.

### 5.12.2 The Markovian master equation

As the branching probabilities between the points has been found, in this Markovian approximation the population at each point obeys the set of master equations

$$\frac{dN_n}{dt} = \sum_m (r_{nm}N_m - r_{mn}N_n) \quad (5.39)$$

in which  $r_{nm}$  is the rate of transfer from  $m$  to  $n$ , given by  $r_{nm} = p_{nm}/\tau$ , where  $\tau$  is the average time spent in  $m$ . In the steady state this matrix equation yields the populations  $N_n$  across both the well populated and rarely populated regions of the measure  $E$ . Having populations and representative start vectors for the region of interest, the phenomena of interest may then be easily studied using the standard Monte Carlo technique.

### 5.12.3 Outline of non-Markovian treatment

A more general form of assumption would be to allow for some non-Markovian nature in the transfer of population between the groups. This method is in effect a further Monte Carlo simulation, making use of the data gathered so far.

In this method, we propagate one or many instances of the system using only the results of the data gathered in the second part of this simulation. We consider only those mother vectors which have daughters. Starting from a particular mother vector, to carry out a single propagation step we choose a daughter vector of that mother vector. We record the time taken to go from that mother to that particular daughter vector, and randomly choose a new mother vector from the same point  $E_i$  as the daughter. Repeated, the cumulative total time measures the population in the various groups<sup>9</sup>.

<sup>9</sup>As before, time should be allowed for the system to settle into a steady state before the population data is recorded.

With each daughter vector chosen randomly from the entire selection of daughter vectors at the current point  $E_i$ , this method is non-Markovian only in the sense that the time elapsed at a point can be correlated to the subsequent daughter point  $E_i$  (the average time elapsed at a point would be independent of the subsequent point for a discrete-variable, continuous-time Markov process). In addition, it is possible to choose the daughter vector while taking into account some of the history of the trajectory. To do this a memory is assigned to each start vector which consists of the  $n$  last points encountered by the trajectory generating this start vector. There is then a series of sub-groups, sharing a common memory, within the group of start vectors at a particular point; the daughter vector would be randomly chosen from the sub-group sharing the same memory as the trajectory currently being simulated. The longer the memory, the less the reliance on a Markovian approximation, but on the other hand the amount of data which must be taken to properly characterise the system scales as a power of the length of the memory  $n$ .

### 5.13 Implementation of the extended Monte Carlo algorithm for the imaging lattice technique

In the situations of interest, the vast majority of the atomic population will have kinetic and potential energies much smaller than that required to hop between sites; as such it seems a clear choice of the ‘measure’ of the extended Monte Carlo technique. However, it is not that simple; the semi-classical potential energy is defined as the expectation value of the potential energy,  $\langle V(\mathbf{r}) \rangle$ , in which  $\mathbf{r}$  is the semi-classical position of the atom, and as such, it does not satisfy the two conditions outlined in Section 5.11.1. This is a consequence of the presence of quantum jumps which are a result of the spontaneous emission of radiation; these jumps lead to substantial jumps in the expectation value  $\langle V(\mathbf{r}) \rangle$ , and (in this case much smaller) jumps in the kinetic energy due to photon recoil. Furthermore, the link between the expectation value of energy and the probability of hopping is complex (consider the case of an excited state atom stationary at a lattice minimum).

To find a variable that is appropriate as a measure for the extended Monte Carlo

simulation, we instead look for an energy-type measure, a pseudo-energy, with the required properties. The most obvious choice is to instead take the expectation value  $\langle V(\mathbf{r}) \rangle$  using the lowest energy ground-state sublevel wave function instead of the real wave function. The time evolution of this quantity is continuous rather than taking the form of discrete jumps; further, when added to the kinetic energy it correctly accounts for the combination of velocity and position needed to differentiate the main population of atoms from those which hop between sites. The choice can be further justified by noting that atoms undergoing polarisation gradient cooling in the lattice tend to be optically pumped to this lowest energy ground-state sublevel (see Sects. 5.1 and 5.2).

Having chosen a measure, the spacing of points along this measure must be determined. For the imaging lattice simulation, this was determined by trial and error to be about 30-35 points spread over the energy range  $0-1.5V_0$ . This approximately minimised the amount of computational time needed to compute consistent dynamics; if more points were chosen, the consistency of the results would go down due to insufficient diffusion in the system phase space (see Sect. 5.11.6), and if the points were too far apart, the time needed to propagate an atom from one point to another would rise substantially, and it would take longer to get sufficient statistics to characterise each point. Although the simulations described in this thesis used equally spaced points, looking back I think there is a good case to find an algorithm, whether recursive or extrapolatory, to determine these points so that the simulation spends approximately the same time with each; this should further optimise the efficiency of the simulation. An appropriate number of start vectors to propagate from each point was determined, which in the optimal cases varied according to the position of the point. The typical number of start vectors propagated was 200, rising to ten times this number at important points such as near the depth of the lattice. Symmetry arguments were also used to reduce the number of unique cases which must be modelled.

---

# THE SIMULATED PERFORMANCE OF THE IMAGING LATTICE TECHNIQUE

The results of the modelling of the imaging lattice technique are presented. The major aim of this chapter is to confirm that atoms can be confined in specific wells of the imaging lattice for a very long time (many seconds) as they fluoresce; this provides a set of parameters around which experiments using this technique can be designed.

## 6.1 Consistency testing

Before using the theoretical and computational techniques developed in Chapter 5 to examine the imaging lattice, a number of simpler scenarios were simulated to check the consistency of the model.

The most basic checks were done on characteristic phenomena of laser-atom interactions, such as the fluorescence and optical pumping of a stationary atom, the dipole force induced by a laser beam, and the heating due to photon recoils. The results were compared to simple analytical calculations. These tests will not be described in detail as the physics is relatively trivial; nevertheless, they were a valuable tool in determining the internal parameters and increasing the efficiency of the simulation.

A more severe test was applied in which a one-dimensional simulation was carried out of polarisation gradient cooling in a dissipative optical lattice. The simulation was set up to replicate the results of previous simulations which were performed using adiabatic [78] and non-adiabatic [47] semiclassical models and a quantum

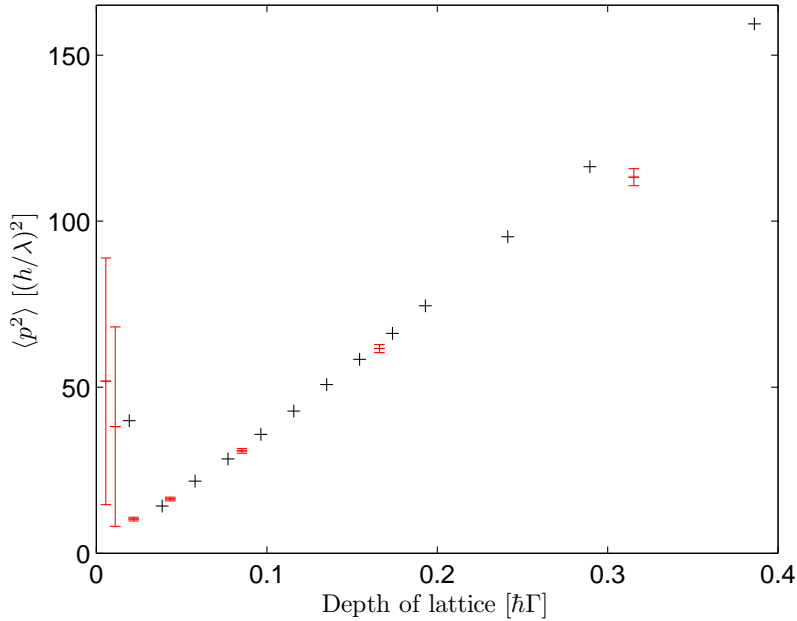


Figure 6.1: A comparison of the model described in this thesis (red) against the non-adiabatic semi-classical method of Reference [47] (black). The simulation is of caesium in a 1D dissipative optical lattice. The depth of the lattice as defined is for the lowest adiabatic state. The momentum variance is proportional to the temperature of atoms in the lattice. The data for the non-adiabatic model is taken from Figure 2 of Reference [47].

band model [8, 78]. The atomic species used in the simulation was caesium, with the cooling beams in the  $\text{lin} \perp \text{lin}$  configuration. The results of such calculations are shown in Figure 6.1. This data was taken using the standard Monte Carlo technique.

The comparison of the model with the non-adiabatic semi-classical method of Reference [47] is interesting as it shows the difference between the semi-classical method as developed in this thesis, and previous work. The most prominent difference in the present method, when not using the extended form of the Monte Carlo technique (Sect. 5.11), is the explicit retention of the excited states (Sect. 5.5.3), which is necessary at the high cooling intensities required for atoms trapped in very deep lattices.

There is excellent agreement between the models in the intermediate depth regime ( $0.05 - 0.2\hbar\Gamma$ ). For deeper lattices, with higher saturation of the cooling transition, the two methods start to diverge. This is to be expected, as the adiabatic elimination of the excited states is only possible when the saturation parameter  $s \ll 1$ ; for  $0.32\Gamma$ , the ex-

cited state has 6.4% of the total population, and it is clear that the adiabatic elimination approximation is breaking down. The method which retains the excited states is the more accurate method for this parameter range, which is the range of interest for the work described in this thesis.

At low intensity the method which retains the excited states correctly predicts the *décrochage*—the increase in temperature at the lowest cooling intensities due to a substantial population of atoms outside the velocity capture range of polarisation cooling. However, this method has substantial statistical uncertainty in this region. This is due to two factors. The first is the form of the momentum distribution in this region; there are two distinct populations of atoms, one with very low energy which undergo polarisation gradient cooling, and the other with large kinetic energy, outside the capture region of the polarisation cooling [21]. These hotter atoms have a very high proportion of the kinetic energy, even as they constitute only a very small proportion of the sample; a lot of data needs to be taken to accurately calculate the momentum variance  $\langle p^2 \rangle$  of the sample. The second reason is that the sample takes a longer time to come into a steady state at low cooling intensities. Adiabatic elimination enables a large increase in the speed of the calculation in this region, and so is desirable to gather good statistics for atoms undergoing low-intensity polarisation gradient cooling.

The above tests confirm the accuracy of the standard Monte Carlo method as used in this thesis. The accuracy of the extended form of the Monte Carlo technique is tested by comparison with the standard Monte Carlo method; this is discussed in Section 6.3.

## 6.2 Frictional energy loss

To compare polarisation gradient cooling in free space and for lattice-confined atoms it is instructive to compare the form of the frictional force in the two situations. The usual way of describing the dissipative effects of polarisation gradient cooling is by a graph of force versus velocity [18, 32]. This is appropriate for cooling in free space, but not so applicable for the cooling of confined atoms where the velocity of the atoms oscillates. Rather than looking for the average force on a path of constant velocity, the average energy loss on a path of constant energy would seem the most appropriate measure. In other words, the polarisation gradient frictional force is usually measured as the force on a test particle being dragged through the light field at a constant velocity; instead we drag the test particle on a trajectory that keeps the sum of the kinetic and potential energies constant<sup>1</sup>.

### 6.2.1 Free space

For polarisation gradient cooling in free space, the force versus velocity graph (Fig. 6.2a), here for  $^{87}\text{Rb}$ , takes the well known form [18]. The  $\text{lin} \perp \text{lin}$  configuration results in a greater force in the low velocity sub-Doppler region whereas the  $\sigma^+ \sigma^-$  configuration is stronger at the high velocity Doppler regime due to the larger Clebsch-Gordon coefficient.

When the low-velocity portion of this data is converted into a graph of energy loss versus energy the same relationship can be seen (Fig. 6.2b). One feature which is perhaps surprising is the shape of the  $\text{lin} \perp \text{lin}$  curve, which is not completely smooth but has small rises and depressions. If a  $F_g = 1/2$  atom is simulated with otherwise identical parameters (the blue dotted lines of Figure 6.2b) these features disappear, and so these seem to be a result of the more complex level structure of the  $|F = 2\rangle \rightarrow |F' = 3\rangle$  transition. These features appear outside the  $F \propto v$  region of polarisation gradient cooling, which is to the left of the red vertical line on this graph. The  $\sigma^+ \sigma^-$  configuration does not have such features.

<sup>1</sup>There are different potential energy surfaces for the various internal quantum states and dressings; here, for simplicity, the bare lattice potential for the atomic ground state is chosen.

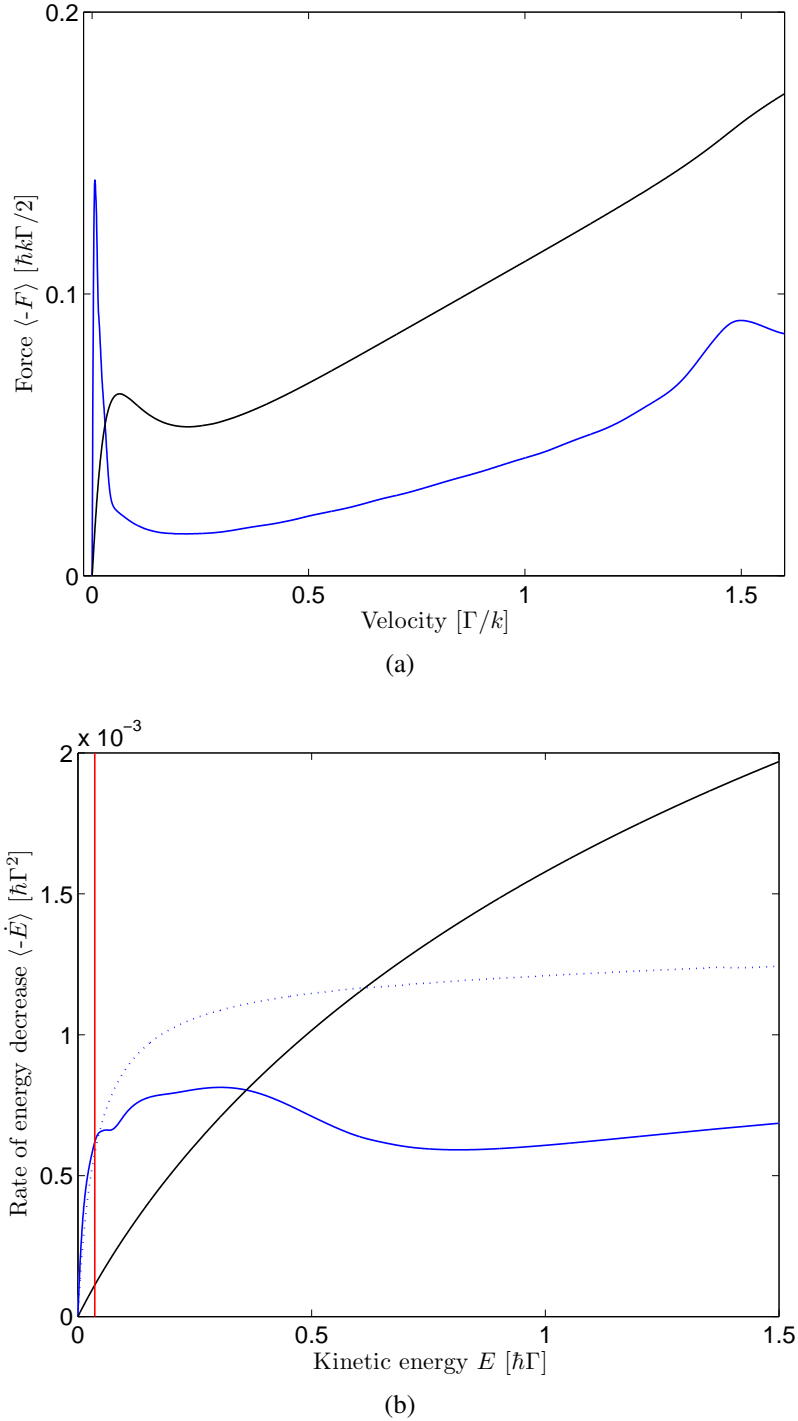


Figure 6.2: Polarisation gradient cooling in free space in one dimension. The  $\text{lin} \perp \text{lin}$  configuration is shown in blue, and  $\sigma^+ \sigma^-$  in black, both with  $^{87}\text{Rb}$ . (a) Force versus velocity. (b) Energy loss rate versus kinetic energy. In Figure (b), the dotted blue line is for a  $F_g = 1/2$  atom in the  $\text{lin} \perp \text{lin}$  configuration, and the red line constitutes the upper limit of the low-energy  $F \propto v$  region for the  $\text{lin} \perp \text{lin}$  configuration, as determined from the data of Figure (a). The intensity per beam is  $10.8 \text{ mWcm}^{-2}$ , and the molasses frequency detuning is  $-4\Gamma$ .

### 6.2.2 Confined atoms

The equivalent graphs for  $^{87}\text{Rb}$  atoms confined in a lattice potential of depth  $1.2\hbar\Gamma$  are shown in Figure 6.3. Here, the velocity shown in Figure 6.3a is the velocity of the atom as it traverses the minima of the lattice potential.

As outlined in Section 5.2.1, the phase of the cooling beams relative to the confining lattice changes the frictional energy loss profile for trapped atoms for the lin  $\perp$  lin configuration, but not for  $\sigma^+\sigma^-$ . As would be expected, this effect is most profound for energies much less than the depth of the lattice.

Another prominent characteristic is the sharp dip at the energy of  $1.2\hbar\Gamma$ , corresponding to the depth of the lattice. This can be attributed to the motion of the test particle; in this small range of energy, the particle spends a large portion of its time near the lattice maxima with very small velocity. As the force and energy loss are time-averaged, they will both fall near this point; in fact, they will tend to zero at  $E = 1.2\hbar\Gamma$ . In Figure 6.3b, the  $\sigma^+\sigma^-$  energy loss curve, and most of the lin  $\perp$  lin curves, lie under the corresponding curve for free atoms (Fig. 6.2b). This can again be explained in terms of the time averaging; the confined atoms on average have less kinetic energy and so tend to have less frictional damping than the free atoms. As in Figure 6.2b, the lin  $\perp$  lin curves exhibit some oscillatory structure; this again seems to be a consequence of the degree of multiplicity of the ground state, as the equivalent  $F_g = 1/2$  curve does not display this structure.

At energies substantially higher than the lattice depth, the shape of the force versus velocity curve for the atoms traversing the lattice (Fig. 6.3a) and in free space (Fig. 6.2a) are broadly similar. The increased force with the lattice present is due to lattice potential decreasing the frequency detuning to atomic resonance, as a blue frequency detuned lattice is used for these calculations. Quantum effects such as Bragg reflection are not modelled in this semi-classical analysis.

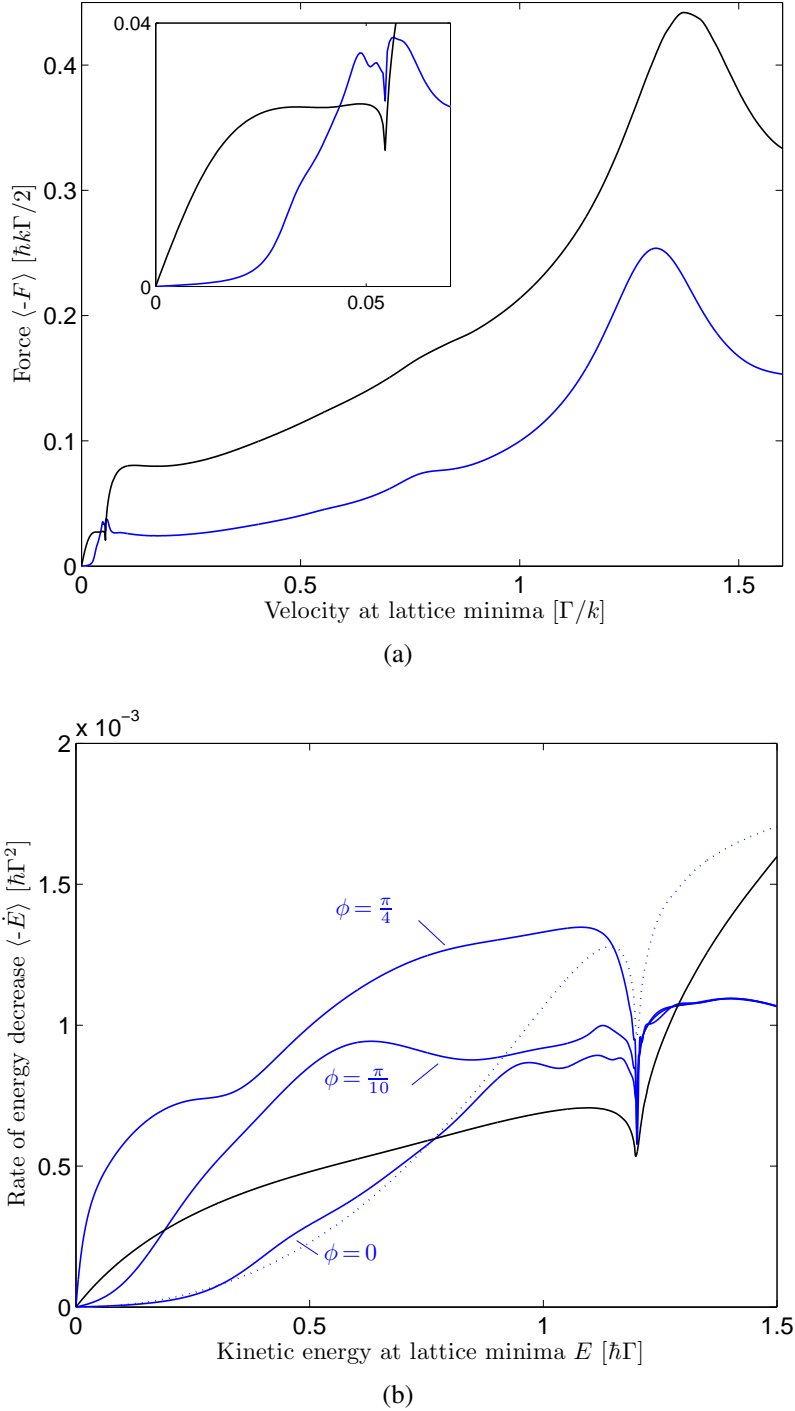


Figure 6.3: Polarisation gradient cooling for confined atoms in one dimension. As before, the lin  $\perp$  lin configuration is shown in blue, and  $\sigma^+ \sigma^-$  in black, both with  $^{87}\text{Rb}$ . The confinement is due to a lattice potential of depth  $1.2\hbar\Gamma$  and period  $\lambda/2$  (as in Table 6.1). (a) Force versus velocity, for  $\phi = 0$ . The insert shows an expansion of the region near the origin. (b) Energy loss rate versus kinetic energy. In Figure (b), the dotted blue line is for a  $F_g = 1/2$  atom in the lin  $\perp$  lin configuration. Three different phases are shown for the lin  $\perp$  lin configuration; the  $\sigma^+ \sigma^-$  configuration is phase independent. The intensity per beam is  $10.8 \text{ mWcm}^{-2}$ , and the molasses frequency detuning is  $-4\Gamma$ .

### 6.3 Specific example of atomic hopping dynamics

#### 6.3.1 Rationale

The primary object of this thesis is to set out the design and make the case for a specific measurement technique. The technique is simulated to determine appropriate parameters which can be used in the experimental realisation. The parameters are chosen so that the polarisation gradient cooling of atoms in the imaging lattice should be such that the atoms are held at specific sites of the imaging lattice for many seconds while measurements are performed.

There is a limiting factor which ultimately must limit the lifetime of atoms in the imaging lattice, regardless of the radiation scattering processes. A collision with a room-temperature background gas particle will inevitably lead to the loss of at least one atom from the imaging lattice. The lifetime due to background collisions will vary by experiment, species, and quantum state, but a typical lifetime due to background gas collisions in a BEC experiment is around  $10^2$  s.

If the lifetime due to radiation scattering processes is greater than around  $10^3$  s, the loss rate due to such processes will be negligible compared to the loss rate due to background gas collisions; we can say that we have an optimal arrangement for polarisation gradient cooling in the imaging lattice. This situation seems to occur for a range of parameters (see Fig. 6.7); any choice of parameters within this range may be regarded as equally good. A particular example will be described in this section for which this is the case; it is emphasised, though, that this set of parameters is not unique, but is one point within an optimal region; other sets of parameters within this region will be equally appropriate for use in an experiment. However, if there is extra heating from an extra process, for example, the boundaries of the this optimal region will change somewhat.

Furthermore, the lifetime which is quoted in this chapter for the radiation scattering process is the average time taken for an atom to leave a specific site from within the lattice. This is related, but greater, than the actual lifetime of the atoms in the imaging lattice; the free atom must either encounter another occupied well, or traverse the lattice, for the atom loss from a specific site to turn into atom loss from the lattice. In fact it

is quite likely that the atom, having left one site, is captured by a nearby site without encountering another atom, and the effects of the atom jumping from the original site are not felt except perhaps in the degradation of spatial resolution of the measurement. Therefore, making the hopping lifetime between sites much greater than the background gas lifetime is a rather conservative overestimate of the effects of the radiation scattering.

In this section an exemplary set of parameters will be put forward in which the hopping lifetime is around  $7 \times 10^4$  s, i.e. well within the optimal region.

### 6.3.2 Parameters used

The parameters used for this example are given in the top part of Table 6.1. The use of the  $\sigma^+\sigma^-$  rather than the  $\text{lin} \perp \text{lin}$  configuration is a consequence of the phase dependence of the latter; controlling the phase of the cooling light at each of thousands of wells is not a viable proposition<sup>2</sup>. The cooling light is flashed alternately along three orthogonal directions, as discussed in Sections 5.3 and 4.7.1. The chop-cycle frequency was chosen to be large enough that atoms are frequently cooled along each direction, but small enough that only a fraction of the flash duration is taken up by the transient optical pumping processes (before the atom settles into an internal steady state, as required for efficient cooling). The intensity and frequency detuning of the cooling light were chosen so that they roughly optimised the hopping rate for this set of parameters. Rubidium-87 was used as the atomic species.

The imaging lattice was chosen (see Sect. 4.5) to be a counter-propagating lattice on the blue side of the D1 line. The frequency detuning of the lattice from the atomic resonance was chosen to be far enough that each internal ground-state sublevel of the atom has approximately the same potential energy (3% difference between the sublevels in this case), but close enough to resonance that a lattice of decent width (hundreds of microns to a side) may be made with the power available in current experiments. The depth of the imaging lattice was chosen to give a long hopping lifetime (see Sect. 6.4).

<sup>2</sup>Alternatively,  $\text{lin} \perp \text{lin}$  could be appropriate if the phase is swept on an appropriate time scale.

Table 6.1: Parameters of the example configuration discussed in Section 6.3. The errors on the calculated parameters are given as the random errors on the mean, and do not include systematic effects.

	Species	$^{87}\text{Rb}$
Imaging Lattice	Line	D1 (794.98 nm)
	Frequency detuning	$-4000\Gamma$
	Intensity per beam	$5 \times 10^4 \text{ mWcm}^{-2}$
	Depth	$1.2\hbar\Gamma$
	Period	397 nm
	Character	1D counter-propagating for each direction (intensities add)
Molasses	Line	D2 (780.24 nm) $F = 2 \rightarrow F' = 3$
	Frequency detuning	$-4\Gamma$
	Intensity per beam	$10.8 \text{ mWcm}^{-2}$
	Flash duration	$18 \mu\text{s}$
	Chop cycle frequency	18 kHz
	Phase swept	No
	Character	1D $\sigma^+ \sigma^-$ Chopped between 3 directions
	Mean time before site hop	$7 \times 10^4 \text{ s} \pm 30\%$
	Temperature	$8.4 \mu\text{K} \pm 2\%$
	Mean scattering rate	$1.88 \times 10^6 \text{ s}^{-1}$
	Scattering uniformity (Direction and Polarisation)	$\sim 99.5\%$

### 6.3.3 Discussion of results

The results of the three-dimensional extended Monte Carlo simulation of the imaging lattice with these parameters are given in Table 6.1 and Figures 6.4 and 6.5. The results give the steady state populations ‘at’ each point, i.e. the proportion of the total population which last encountered that specific point rather than any other.

There is an extremely good fit between the population predicted by the standard Monte Carlo simulation and that predicted by the extended Monte Carlo simulation, in the region in which the standard Monte Carlo simulation can be used<sup>3</sup>. An excellent fit between the two was found on all data presented in this chapter (including the data presented in Figs. 6.7 and 6.7). As the methods by which the populations are calculated

<sup>3</sup>The last point or two of the standard Monte Carlo data is not quite on the line of the others, but this is to be expected from the poor statistics of the Monte Carlo simulation at these energies.

are substantially different, this provides a very good indication that the extended Monte Carlo simulation of this problem is an accurate extrapolation of the standard Monte Carlo technique, the accuracy of which has been tested earlier (Sect. 6.1). Furthermore, as this data was generated using the Markovian master equation treatment, it is suggested that a more involved non-Markovian analysis of the extended Monte Carlo technique (as outlined in Section 5.12.3) is unnecessary in this case.

The population data can be fitted to a temperature once the density of states in the lattice site has been found, by using the equation

$$D(E) = \frac{(2m)^{\frac{3}{2}}}{(2\pi)^2 \hbar^3} \int_{V(\mathbf{r}) \leq E} \sqrt{E - V(\mathbf{r})} d^3 \mathbf{r} . \quad (6.1)$$

The description of the population in terms of a temperature is accurate in the low energy region, but there are substantially more atoms in the tail of the distribution than would be expected for a given temperature. This not unexpected, as the description of the population in terms of a temperature is only valid when the frictional force divided by the diffusion coefficient is a linear function of velocity (as shown by the Fokker-Planck equation—see for example [67] p66). The frictional force is in fact not linear—the slope of the force decreases with increasing energy (Fig. 6.3a), so it is natural that the population in the tail is higher than the temperature of the low-lying atoms would predict. This can be seen as retrospective justification for using the extended Monte Carlo method to find the population in the tail of the distribution rather than merely extrapolating using a fit to temperature.

The population distribution was calculated using the data displayed in Figure 6.4. These figures display the rates of transfer of atoms between the various points, as found in the analysis of the data from the extended Monte Carlo simulation. The rate to decrease in energy is greater than the rate to increase in energy for all but the lowest-lying points; the difference in rates increases with energy, as may be expected, as the frictional energy loss increases with energy throughout this region (see Figure 6.3b). There is some small variation in the rates data at higher energies; this leads to variation in the hopping lifetime between simulation runs, which is reflected in the quoted statistical uncertainty on the lifetime (Table 6.1).

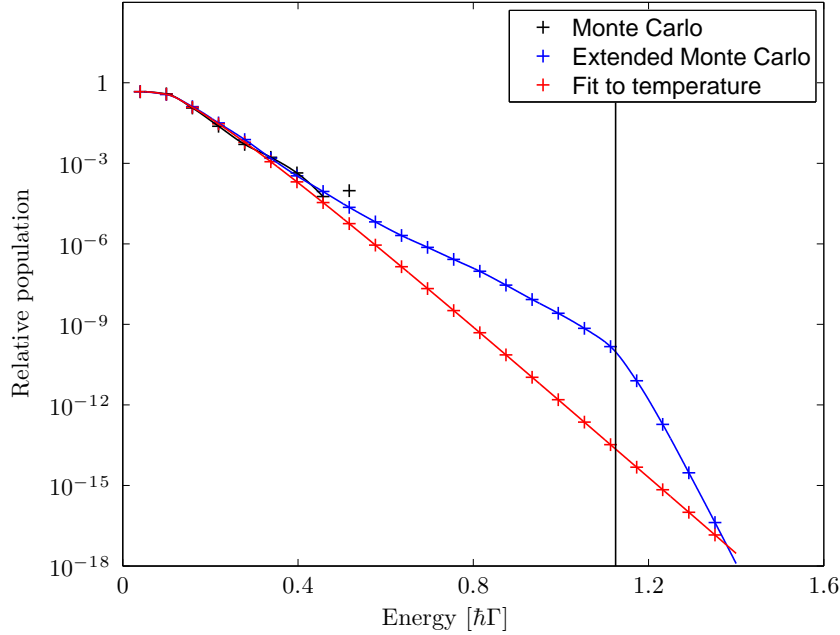


Figure 6.4: Histogram of population versus energy for the imaging lattice parameters set out in Table 6.1. The  $x$ -axis gives the (pseudo-)energy of the points, while the  $y$ -axis gives the proportion of the population which last encountered that energy point. The depth of the pseudo-energy potential is  $1.125\hbar\Gamma$ , which is less than the bare lattice ( $1.2\hbar\Gamma$ ) due to the dressing with the cooling light. The top of the lattice potential is marked with the vertical black line. The extended Monte Carlo populations were calculated from the data of Figure 6.5 in a Markovian approximation.

The ‘jump’ rate is the rate at which the atoms leave the site. Only one site is simulated, rather than the entire lattice, so when the atom leaves the site, it is removed from the simulation; in the master equation analysis, the total population in the well is renormalised to compensate for this loss. For energies greater than the lattice depth, the jump rate between wells quickly dominates the heating and cooling rates. Although there is some cooling of untrapped atoms (see Figure 6.3b), only atoms with an energy slightly above the lip have an appreciable probability of being captured by that site; the atoms with larger energies cannot be cooled in time, and disappear off to another site or out the lattice. The effects of the jump process can be seen in the sharp decrease of the population with energies above the lip of the lattice (Fig. 6.4).

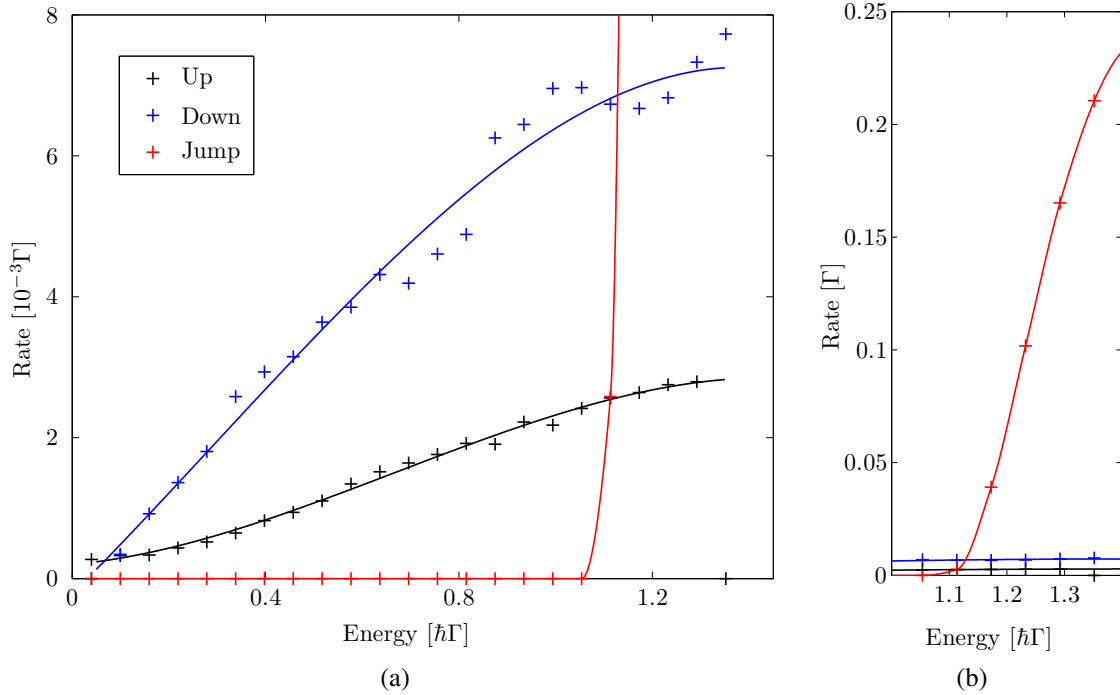


Figure 6.5: The transition rates of atoms between the energy points. These were calculated from the data collected in the extended Monte Carlo simulation, and are used to calculate the population at the points shown in Figure 6.4. There are three alternatives for an atom at a particular point: it can encounter the next point down in energy, or the next point up, or it can leave that lattice site. The rates as shown are the rates for these processes at a particular energy. The depth of the pseudo-energy potential is  $1.125\hbar\Gamma$ .

### 6.3.4 Coherence properties of the scattered light

The coherence properties of the scattered light become relevant when there is more than one atom imaged to the same pixels of the CCD; this is the case when there is more than one atom per original accordion lattice site, as in this case the atoms are separated by a fraction of an accordion lattice period, and we assume that we do not have an imaging system capable of distinguishing the atoms at this small separation. If the atoms scatter coherently, there is a redistribution of the scattered intensity over the unit sphere. If this redistribution is not time-averaged away, the linear relation between the observed signal and the number of the atoms at the original accordion lattice site breaks down to a degree.

We can find the proportion of coherent light by finding the mean dipole of the

Table 6.2: Coherence properties of the fluorescent scatter, for the example configuration discussed in Section 6.3.

Direction	Total scattering rate	Incoherent proportion
$\sigma^-$	$0.0112\Gamma$	$\sim 100\%$
$\pi$	$0.0269\Gamma$	$87\%$
$\sigma^+$	$0.0112\Gamma$	$\sim 100\%$
Total	$0.0492\Gamma$	$48\%$

fluorescing atom. The instantaneous dipole in direction  $\varepsilon$  is  $\langle \mathbf{D}_\varepsilon^+ \rangle$ , and we denote the time average by  $\langle\langle \mathbf{D}_\varepsilon^+ \rangle\rangle$ . We replace the operator  $\mathbf{D}_\varepsilon^+$  by

$$\mathbf{D}_\varepsilon^+ = \langle\langle \mathbf{D}_\varepsilon^+ \rangle\rangle \mathbf{I} + \delta \mathbf{D}_\varepsilon^+ \quad (6.2)$$

where by definition  $\langle\langle \delta \mathbf{D}_\varepsilon^+ \rangle\rangle = 0$ . The decay rate in direction  $\varepsilon$  is then

$$\langle\langle \mathbf{D}_\varepsilon^+ \mathbf{D}_\varepsilon^- \rangle\rangle = |\langle\langle \mathbf{D}_\varepsilon^+ \rangle\rangle|^2 + \langle\langle \delta \mathbf{D}_\varepsilon^+ \delta \mathbf{D}_\varepsilon^- \rangle\rangle. \quad (6.3)$$

In this equation, the first term on the right hand side is associated with coherent scattering, and the second term with incoherent scattering ([15] p. 383)

The results of this analysis are shown in Table 6.2. The data is taken when the light at the lattice minimum is  $\pi$  polarised. As can be seen, the majority of the  $\pi$  fluorescence emitted is coherent, while the other polarisations are incoherent (the mean dipole sums to zero). The scattered light is roughly equally divided between coherent and incoherent components.

A further factor to bear in mind when considering coherence properties is the average spatial deviation of the atom from the lattice minimum; in the case under consideration the root mean square deviation is  $\sim 0.013\lambda$ . This means that the atom is very well localised compared to the wavelength of the scattered light, meaning that it would be possible to see coherence effects.

A mitigating factor is the chopping of the cooling beams between the three directions. This will tend to average out the redistribution of the fluorescence light due to coherence effects. As an additional mitigating measure, a small frequency difference (on the order of a kilohertz) between the cooling beams will sweep the direction of polarisation at all sites. This will sweep the interference pattern from the coherent fluorescence

of atoms from a single accordion lattice site around the axis of these cooling beams. Together with the chopping of the cooling beams between the three directions, any interference pattern will be smoothed, although some residual anisotropy could remain. This is likely to be necessary only when there are more than a few atoms per accordion lattice site, when it becomes more critical that there is a linear relationship between the observed signal and atom number. There are likely to be other way to mitigate the effects of coherence, for example by observation of th fluorescence generated by radiative cascade 7.2.

In summary, with these parameters the scattered light is roughly coherent and incoherent in equal measure. While this means that the scattered signal cannot be completely destroyed by interference, it means that a certain amount of caution is required to correlate the observed signal with the number of atoms originally at the accordion lattice site.

### **6.3.5 Reabsorption**

Reabsorption can potentially affect the process in a number of ways. Firstly, reabsorbed radiation can heat the atoms due to anomalous recoil events. Secondly, reabsorption decreases the intensity of the cooling beams and the imaging signal as the near-resonant light traverses the cloud. Thirdly, the other atoms may induce local phase changes in the scattered signal. These considerations shall be dealt with in turn.

For the calculation of the scattering for a very numerous extended sample, a  $50 \times 50 \times 50$  cubic grid of atoms is used with a  $4\mu\text{m}$  nearest neighbour distance<sup>4</sup>. The effects of the net outward force (such as in a MOT) will be negligible in the lattice; it is the fluctuations of this force which are important. Using the data in Table 6.1, the intensity of the scattered radiation at the centre of the sample is found to be around 4% of the total intensity of the cooling beams. The heating rate from photon recoil will increase in about this proportion. The optical pumping rates between the sublevels also changes by around this proportion, so the steady-state populations and the sub-Doppler force could also decrease by around this fraction. The combination of these effects have

---

<sup>4</sup>This makes 125,000 atoms, significantly larger than the atomic samples which the technique is designed to probe

the potential to increase the temperature by around 5-10%; as can be seen from Figure 6.4, such an increase in temperature corresponds to up to an order of magnitude greater population in the highest trapped levels, and so the loss rates will be around an order of magnitude greater. Although this sounds large, the lifetime of the atoms in a site will still be limited by collisions with background gas atoms rather than this hopping dynamics; furthermore the effects of this level of reabsorption may be completely negated by an increase in the depth of the imaging lattice of 10-15%. I emphasise that the scenario considered here (with 125,000 atoms) is a worst-case scenario for this technique.

The cross-section of the atoms at this wavelength may be calculated using a standard formula, or (taking into account the multilevel system) by using the data in Table 6.1. Using the above data, the atomic cross-section is  $2.2 \times 10^{-3} \mu\text{m}^2$ , so over 99% of the laser beams are transmitted through the large sample we are considering. Thus both the cooling beams and the imaging signal are only weakly affected by reabsorption by the other atoms the sample.

To estimate the dispersive effects of the atoms, the formula for the real part of the refractive index of a two-level system is used [52]

$$n - 1 = \frac{3n\lambda^3\Delta\Gamma}{4\pi^2(\Gamma^2 + 4\Delta^2)}. \quad (6.4)$$

Multiplying  $n - 1$  by the distance through the sample, the average phase retardation compared to vacuum propagation is around 1/100<sup>th</sup> of a cycle. Thus the average phase retardation difference across an extended wavefront is also about this order. Since distortion at least on the order of the imaging wavelength is needed to increase the spot size at the detector, the dispersive effects of this density of atoms will be fairly minimal when it comes to measuring the signal.

### 6.3.6 Summary

In summary, if an experiment was performed with the parameters given in Table 6.5, it is predicted that each atom will have a lifetime at a specific site which is limited by collisions with background gas. Each atom will scatter  $\sim 10^6$  photons per second, which is a substantial signal. For extended samples probed using the accordion and imaging

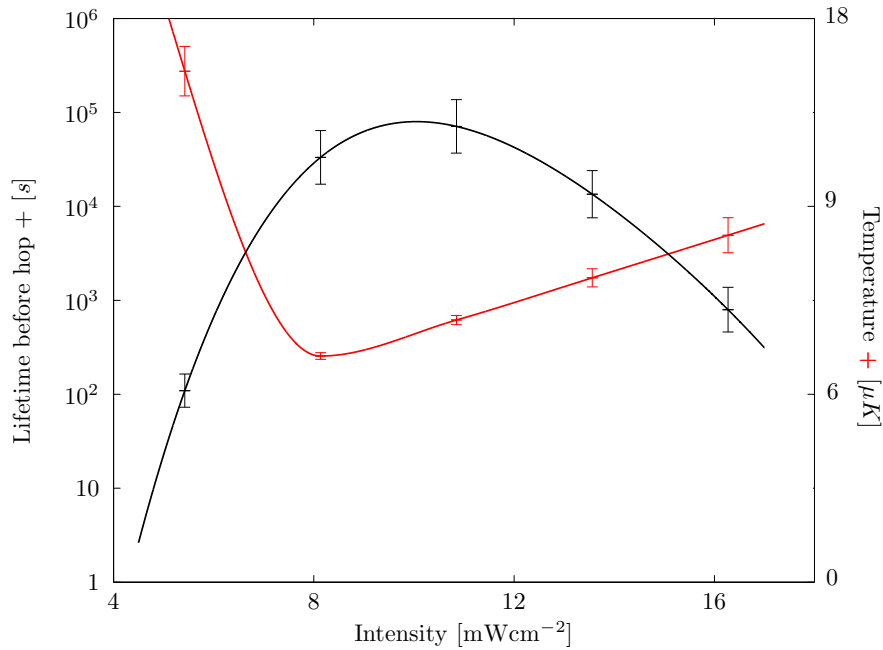


Figure 6.6: The variation in temperature and hopping lifetime in the imaging lattice with cooling intensity. The data used in these calculations is the data of Table 6.1 for all variables other than the cooling intensity.

lattice techniques, reabsorption processes may add a little anomalous heating, but at on a level much less than the diffusion due to photon absorption from the cooling light. The scattered light is approximately half coherent and half incoherent.

#### 6.4 Atomic hopping dynamics over a range of parameters

The hopping lifetime of the atoms is a function of the parameters of the imaging lattice technique. Although I have not yet had the computational resources and time to conduct a comprehensive characterisation of this parameter space, data will be presented for the two most important variables, lattice depth and cooling intensity.

As the cooling intensity is varied (Fig. 6.6), the variation in hopping lifetime correlates reasonably well with the temperature of the atoms at the lattice site. At higher intensities, the polarisation gradient cooling becomes less efficient, and the temperature increases. This behaviour is common to most situations in polarisation gradient cooling (see Sect. 6.1); as the optical pumping time decreases, there is less movement-generated lag in the atomic populations, and the corresponding frictional force is less. At lower in-

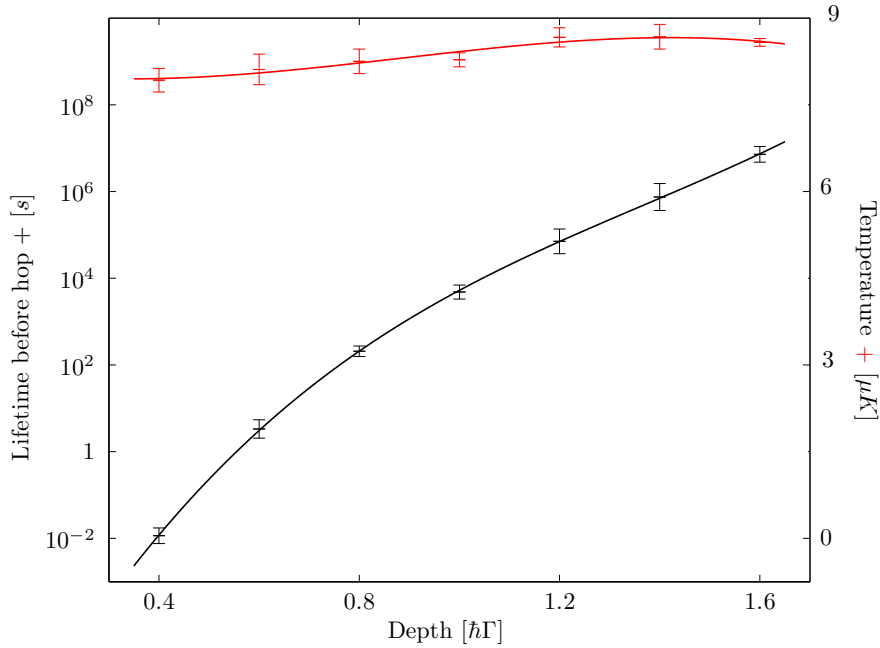


Figure 6.7: The variation in temperature and hopping lifetime in the imaging lattice with lattice depth. The data used in these calculations is the data of Table 6.1 for all variables other than the lattice depth.

tensities, on the other hand, the temperature increases as the optical pumping time takes up an increasingly larger fraction of the vibrational period; therefore it has insufficient time for the internal state to approach a steady state, so less time for efficient polarisation cooling to take place, before the oscillation of the particle changes its velocity, and the internal state must undergo transient behaviour again. The consequence of these two effects is that there is an optimal intensity for the cooling beams of the imaging lattice technique. An additional consequence is that this puts an upper limit on the depth of the lattice in which atoms may be efficiently polarisation gradient cooled; the deeper the lattice is, the faster the oscillation frequency, so the smaller the window in the optical pumping rate in which efficient cooling is possible.

With the parameters currently used, though, the large decrease in the hopping rate as the depth is lowered (due to the near-exponential high-energy tail of the population) greatly outweighs the small increase in the energy due to the increase in oscillation frequency (Fig. 6.7). This shows that the example presented in Section 6.3 is worse than the global optimal parameters by at least a good few orders of magnitude, even though

a lifetime of  $7 \times 10^4$  is substantially longer than we need, i.e. much longer than the lifetime due to background gas collisions. This indicates that, if the parameters are chosen with care, the imaging lattice technique could cope with a substantial amount of anomalous heating before light scattering and light-assisted collisional processes can decrease the lifetime of the atoms in the lattice below the lifetime dictated by background gas collisions.

---

## SUMMARY AND EXTENSIONS TO THE ACCORDION AND IMAGING LATTICE TECHNIQUES; POTENTIAL FOR NOVEL ULTRACOLD PHYSICS

This chapter further develops the accordion and imaging lattice techniques in the light of the preceding chapters. Improvements and extensions are discussed to the basic technique. A summary is made of the basic techniques, and a specific design of apparatus is presented in order to put forward a concrete proposal for an experiment. The prospects for novel physics that such experiments could provide are outlined.

### **7.1 High resolution three-dimensional measurements at the level of individual atoms for arbitrary ultracold atomic configurations**

The motivating reason for the design of the accordion and imaging lattices was to find a technique capable of detailed measurements on strongly interacting physics of ultracold atoms in optical lattices. However, these techniques have a number of characteristics which make them suitable for detailed measurement of a whole range of phenomena in ultracold atomic physics. It is interesting to compare these techniques to standard probing techniques, for example absorption imaging, when used to probe an atomic sample with an arbitrary spatial and momentum distribution, confined in an arbitrary potential, or in free evolution (i.e. in time-of-flight). There are two ways of probing

this arbitrary sample with the above techniques; the imaging lattice and the subsequent cooling and fluorescence imaging can be used with or without the prior capture of the atoms by an accordion lattice.

Consider the case that only the imaging lattice is used, together with the appropriate cooling technique and fluorescent imaging (as discussed in Sect. 4.6 and Chapt. 6). The density and optical depth of the atomic sample are critical factors in this scenario. If the density of atoms in the sample is too great, many atoms will be lost due to light-assisted collisions from multiply occupied wells. Furthermore, if the optical depth of the sample is too great, reabsorption, and consequently extra heating and suppression of the fluorescence signal, will mean loss of atoms and alteration of the observed fluorescence distribution. Both of these effects make the observed fluorescence distribution different to the true atomic distribution. Furthermore, the high atom numbers will mean that measurement of the three-dimensional distribution of atoms in the sample is hard<sup>1</sup>. If these effects can be tolerated, the use of the imaging lattice, together with a lens system of appropriate magnification, is a possible alternative to two-dimensional absorption imaging for BEC-sized samples. However standard absorption imaging is likely to be the better imaging technique for measurements of the overall distribution of large samples, as the exposure time, and so the effect of light-assisted collisions, is much less.

However, at low densities and low atom number the use of the imaging lattice does have significant advantages over absorption imaging. As has already been noted (Sect. 4.1), fluorescence imaging is well known as the imaging method of choice for low atom numbers. The use of the imaging lattice enables the spatial distribution of the sample, in-situ or in time-of-flight, to be locked in place while fluorescent imaging is taking place. The long lifetime of atoms in the imaging lattice will mean that the collected signal from each atom will be large. The use of the imaging lattice, together with a good objective lens, will allow 3D measurements to be made of the spatial distribution of low atom number samples at the resolution of single atoms. As such, the imaging lattice

---

<sup>1</sup>3D images can still be built up by using a separate imaging sheet (see Sect. 7.2), although the resolution will not be very high.

technique is potentially an excellent technique for the measurement of the properties of any ultracold atomic distribution of low atom number.

The use of the accordion lattice prior to the imaging lattice will potentially enable even better measurements of an arbitrary ultracold atomic distribution. The accordion lattice would be used in an extra step prior to raising the imaging lattice; the accordion lattice, in the counter-propagating configuration, would be used to freeze the atomic distribution. The accordion lattice would then be expanded to the large-period configuration. At this point the imaging lattice is turned on, followed by the start of the concurrent cooling and fluorescent imaging.

There are two major advantages in using the accordion lattice in this way prior to the imaging lattice. Firstly, the volume resolution of the technique is now a box of side  $\lambda/2$  (typically around 300-400 nm). This is a linear spatial resolution around an order of magnitude greater than that in a typical absorption image. To emphasise, these measurements can be performed throughout a volume of space, rather than a projection of this volume; the measurements can be carried out at the resolution of single atoms.

Secondly, the expansion of the accordion lattice can reduce the density and number of atoms in the sample by a few orders of magnitude. Therefore it is possible to start from a dense, high number atomic sample and use this technique to probe a certain (small) volume of this atomic distribution at extremely high resolution. The remainder of the atoms will be ejected from the accordion lattice in the expansion process; they should be allowed to fall out of the imaging region before the imaging lattice is turned on. This method is inappropriate for the measurement of overall atomic distributions, as in absorption imaging; instead, it offers a complimentary method of probing for making very detailed measurements of a small portion of a larger atomic distribution. There are undoubtedly many aspects of quantum dynamics which would benefit from this treatment; to put forward a couple of illustrative examples, the spatial structure of a single vortex in a BEC could be probed in three dimensions at very high spatial and number resolution, or the signal from very faint diffraction peaks could be accurately determined.

It is clear from the preceding arguments that this is potentially a very power-

ful technique of measuring the detail of atomic distributions, in three dimensions, at a spatial resolution of a few hundred nanometres, and at the level of single atoms. The downside is that the technique is limited to a low atom numbers (depending on the exact experimental configuration, in the range of thousands or a few tens of thousand of atoms) and a small sampling volume (again, depending on the exact configuration, perhaps  $5\text{-}20\ \mu\text{m}$  on a side).

## 7.2 Minimisation of fluorescence from out-of-plane atoms whilst imaging three-dimensional samples

As has been discussed in Sections 4.7.5, 6.3.5 and 7.1, the fluorescence from out-of-plane atoms starts to become a problem for large three-dimensional samples, as the signal from the in-plane atoms becomes harder to distinguish from this background. With a little more effort, a method can be implemented that would dramatically decrease the signal from these out-of-plane atoms.

It may be thought that the lower hyperfine state can be used to ‘shelve’ the out-of-plane atoms and so reduce this unwanted fluorescence, by means of restricting the beam profile of the repumping beam. However, the scattering from the imaging lattice, while negligible when the atoms are in the upper hyperfine state, will still be present when the atoms are in the lower hyperfine state, and in the absence of the repumping beam the atom will tend to undergo transitions between the two hyperfine levels on a time scale of around a millisecond. Another method which could be used to probe single sheets from a lattice is the application of a magnetic field gradient. However in the case of the imaging lattice the magnetic field would disrupt the polarisation gradient cooling process, and could only be used if it were quickly alternated with cooling periods i.e. periods when the magnetic field was off.

A possible way to get around this issue would be to switch off the repumping beam altogether, and instead use an optical pumping beam (for example, on the  $|F = I + 1/2\rangle \rightarrow |F' = I - 1/2\rangle$  transition) to pump the overwhelming majority of the population into the lower hyperfine level. The profile of this optical pumping beam would be a  $\text{TEM}_{01}$  Hermite-Gaussian mode, with the central minimum forming a sheet which

would be aligned with the imaging plane of the lattice. All the atoms apart from those in the central plane would be shelved; those atoms in the central plane would spend about half the time in the upper hyperfine level, and majority of the fluorescence from the sample would be from atoms in this plane.

There there is the potential for extra heating from these cycles between the ground hyperfine states, as the lower hyperfine state is more confined than the upper hyperfine state by the blue frequency detuned imaging lattice. If the atoms are strongly optically pumped to one of the two hyperfine states, this extra heating is relatively small, as the atoms cannot spend long enough in the other hyperfine state to react to the different potential energy surface. When atoms cycle between the states, as in the case for the atoms in the central plane of the TEM01 optical pumping beam, this becomes more of an issue. Only a small proportion of the atoms (those that are currently being measured) have this anomalous heating.

Another, more promising, technique would be to probe at a different wavelength than the cooling beams. These extra probing beams would propagate in a thin sheet in the focal plane of the imaging system; two counter-propagating beams would minimise the average momentum gain due to photon recoils. A good candidate transition would be the other D line (796 nm for  $^{87}\text{Rb}$ ), with the imaging lattice itself near the D2 line. Unfortunately higher frequency states  $(n + 1)p$ , e.g. the  $6p$  state at 420 nm from the rubidium ground state, will tend to have a fairly large photoionisation rate due to the imaging lattice light [12, 1]. The beams would propagate at the same time as the cooling beams, with the cooling light itself filtered out in the imaging path.

A logical extension to this would be imaging using a radiative cascade. Using a radiative cascade to produce the fluorescent signal would mean that the scattered signal is completely incoherent. The most promising cascade would seem to be from the  $(n + 1)s$  or  $nd$  state, which can be directly excited from the  $np$  excited state of the atoms undergoing cooling. For example, the  $6s$  state of  $^{87}\text{Rb}$  can be excited from the  $5p$  state by a laser at wavelength  $1.37\ \mu\text{m}$ ; it decays with a lifetime of 45 ns back to the  $5p$   $J' = 1/2$  and  $J' = 3/2$  states. Assuming that the imaging lattice is near the D2 transition, the photons which are detected on the D1 transition (or at  $1.32\ \mu\text{m}$ ) will be incoherent,

and can only come from the atoms within the sheet of  $1.37\ \mu\text{m}$  light. Higher-lying states could be used for the cascade, for example  $(n + 2)s$ , at the expense of a larger photoionisation rate.

For either imaging method, small sub-wavelength movements of the imaging lattice parallel the cooling beams can be used rotate the direction of the linear polarisation at the lattice minima, and so remove any anisotropy in the distribution of the scattered signal. This could be used in place of relative phase control of the counter-propagating pairs of cooling beams, which would achieve the same effect, but (as a practical consideration) would need twice the number of AOMs to generate the cooling light.

Even by using one of the above methods, it is likely that not just a single sheet is picked out, but a few sheets are picked out by either of these techniques. To distinguish between these neighbouring sheets of atoms the imaging system would need to have a shallow enough depth of view, and the accordion site separation be large enough, that atoms from neighbouring accordion lattice sites are able to be distinguished, for example as in Reference [71].

### 7.3 Summary of the basic technique

This section provides a summary of the joint use of the accordion and imaging lattice techniques. To do this a single example is picked of the way these techniques may be implemented; in this example we take the atomic species to be  $^{87}\text{Rb}$ .

#### 7.3.1 Capabilities

The techniques analysed show the capability to image the spatial distribution of ultracold in up to three spatial dimensions. The technique is capable of reliably measuring the position of every atom within a small volume (of the order  $10\ \mu\text{m}$  to a side), with a spatial resolution of around  $\lambda/2$  of the resonance wavelength.

The technique can be used either *in-situ* or in time-of-flight. The technique is capable of probing the dynamics within an optical lattice, which is conveniently the accordion lattice itself, or atoms otherwise confined, or in free flight. The technique is applicable for both fermions and bosons (or mixtures).

The primary restriction of the technique is that if the kinetic energies of the atoms are greater than the maximum depth of the accordion lattice, the technique cannot be used. Clearly, if the atoms cannot be sub-Doppler cooled, the technique cannot be used.

If the technique is used without the accordion lattice stage, reabsorption of the radiation will limit the number of atoms that can be usefully probed.

### **7.3.2 An exemplar experimental design**

The basic experimental process is summarised in Figure 7.1. The atoms are captured by the accordion lattice, if they were not already present in the lattice, and the accordion lattice depth is quickly raised to isolate atoms at individual sites. The accordion lattice is then expanded, preferably in all three dimensions, until each site is separated by many microns from its neighbours. The atoms are loaded into the strong imaging lattice potential; each accordion lattice site is divided into hundreds or thousands of imaging lattice sites, with multiple occupation of imaging lattice sites statistically unlikely.

With the atoms isolated and confined in a deep potential, the polarisation gradient cooling commences. This is best achieved with a one-dimensional  $\sigma^+\sigma^-$  configuration, which is flashed (chopped) between three orthogonal directions. The atoms are imaged from the fluorescent light they produce while undergoing cooling.

To efficiently image large three-dimensional samples, an additional sheet of light should be used to illuminate only those atoms in the focal plane of the imaging system. In this example we choose this light to be on the  $5p$  to  $6s$  transition ( $1.37\ \mu\text{m}$ ); we detect the incoherent fluorescence on the D1 ( $796\ \text{nm}$ ) transition.

The imaging lattice is translated to bring different planes of atoms successively into the focal plane of the imaging system; an image is taken of each plane. In this way, a three-dimensional spatial profile of the atoms will be built up. This measurement process may take place over many seconds (the lifetime of the atoms will be predominantly limited by background gas collisions).

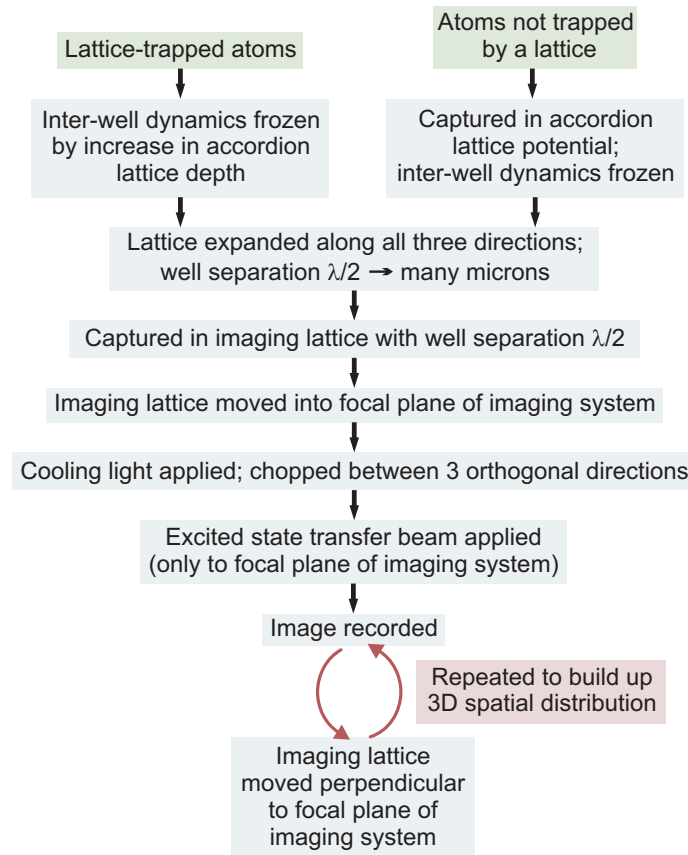


Figure 7.1: A summary of the basic imaging sequence for three-dimensional measurements of the spatial distribution of ultracold atoms at single atom number resolution and  $\lambda/2$  spatial resolution. There are a number of variants on this basic sequence which could be used depending on the circumstance, for example the application of a magnetic field gradient for measurements of the internal state of lattice-trapped atoms, or for long times of flight.

### 7.3.3 Practicalities

The complex part of the apparatus is the accordion lattice itself. Mirrors located inside the vacuum system are needed for counter-propagating arrangements; illustrative designs are given in Figures 4.3 and 7.2. These could be constructed from parabolic reflecting surfaces sectioned and shaped with a precision glass cutting device such a wafering saw.

The optical access around such a mirror arrangement can be improved by removing unwanted parts of the parabolic mirror—those parts not used by the accordion lattice, and too far off axis to be of use in fluorescent detection. Such a design is shown

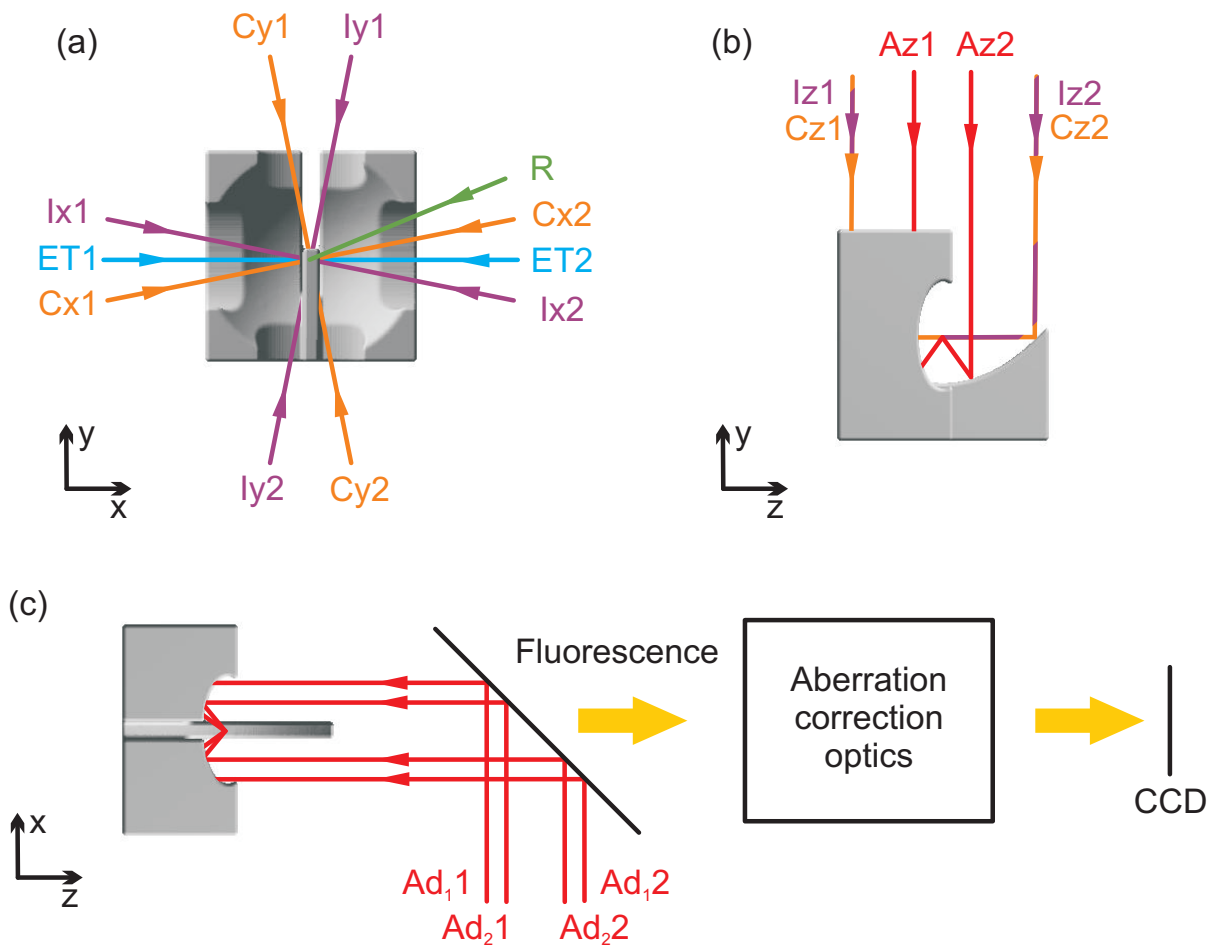


Figure 7.2: The optical layout of an illustrative accordion and imaging lattice experiment. The beams shown are described in Table 7.1, and are colour-coded (red for the accordion lattice, purple for the imaging lattice, orange for the cooling light, blue for the excited state transfer beams, and green for the repumping light). The design shown here uses the inner part of the parabolic mirror itself as the first lens in the imaging system; other designs are possible (see Section 4.7.2). As shown, unwanted outer parts of the parabolic mirror can be removed to facilitate optical access.

in Figure 7.2. The number of laser beams needed for the accordion and imaging lattices makes it desirable to use magnetic transport to move the cold atoms into this region from another section of the vacuum system, where the primary MOT and associated optics can be located separately.

Illustrative beam paths into the region containing the atoms are given in 7.2. This particular design assumes that the parabolic mirror is used as the first element in the imaging system; corrective optics (together with a beam stop) will be needed to compensate for the off-axis aberrations (see Sect. 4.7.2). The fluorescent imaging path overlaps with four of the accordion lattice beams; a dichroic beamsplitter is assumed to be used to combine the two. The parallel beams entering the apparatus vertically also need to be combined using beamsplitters (an appropriate selection of non-polarising, polarising or dichroic is assumed).

A summary of the beams required for the technique is given in Table 7.1. The beams reflecting off the parabolic mirror will be focussed by this mirror; this should be accounted for in the up-stream optics (see Sect. 4.4.1).

Movement of the accordion lattice is most easily accomplished by mounting a particular mirror on a piezoelectric stage (see Sect. 4.4). The imaging lattice can either be translated using a similar arrangement, or by using a AOMs to control the relative frequency detuning of the beams (taking the number of AOMs needed for the imaging lattice from 3 to 6).

#### 7.3.4 Performance

These techniques are designed so that the fidelity of the measurements is very high. The results of Chapter 6 indicate that, for suitable parameters, the atoms remain localised at a particular site until a background gas collision removes the atom from the lattice. Such a long measurement time allows excellent statistics to be built up for the reliable detection of individual atoms; furthermore, the technique is designed so that atoms spaced by more than  $\lambda/2$  in the original sample are resolved.

It is anticipated that the two factors which will limit the fidelity are the statistical loading losses, and background gas collisional losses. Statistical loading losses

Table 7.1: Summary of the beams needed for the illustrative design of the apparatus (as shown in Figure 7.2).

Accordion lattice	Beams (Labels)	6 (A <sub>ij</sub> )
	Frequency	As required (far off resonance)
	Power	As required
	Polarisation	As required
	Waist	A few hundred $\mu\text{m}$ at atoms
	Generation	$3 \times$ AOD with accompanying optics (see Figs. 4.2b and 4.4)
Imaging lattice	Beams (Labels)	6 (I <sub>ij</sub> )
	Frequency	$10^3 - 10^4\Gamma$ blue of the D2 or D1 line
	Power	1-20 mW per beam
	Polarisation	Linear
	Waist	A few hundred $\mu\text{m}$ at atoms
	Generation	$3 \times$ AOMs or $6 \times$ AOMs (without piezos) (see Sects. 4.7.3 and 7.3.3)
Cooling light	Beams (Labels)	6 (C <sub>ij</sub> )
	Frequency	A few $\Gamma$ red of the D2 closed transition
	Power	A few tens of $\mu\text{W}$ per beam
	Polarisation	$\sigma^+ \sigma^-$
	Waist	A few hundred $\mu\text{m}$ at atoms
	Generation	$3 \times$ AOM
Excited state transfer beams	Beams (Labels)	2 (ET <sub>1,2</sub> )
	Frequency	$(5p) \ ^2P_{3/2}  F = 1\rangle \rightarrow (6s) \ ^2S_{1/2}  F = 2\rangle$ (1.37 $\mu\text{m}$ )
	Power	A few $\mu\text{W}$ per beam
	Polarisation	$\sigma^+ \sigma^-$
	Waist	$(5-10 \mu\text{m}) \times$ (a few hundred $\mu\text{m}$ ) at atoms
	Generation	$3 \times$ AOM
Repumping light	Beams (Labels)	1 (R)
	Frequency	D2, $ F = 1\rangle \rightarrow  F' = 2\rangle$
	Power	10-100 $\mu\text{W}$
	Polarisation	Any
	Waist	0.5-1 mm

are discussed in Section 4.5; they occur when more than one atom is loaded into the same imaging lattice well. Assuming reasonable experimental parameters (the critical parameter being the ratio of accordion to imaging lattice well volumes), this loss can be made less than 1%, using a three-dimensional accordion lattice, for reasonably high initial atomic densities (tens of atoms per cubic resonant wavelength).

The contribution of background gas collisions to the fidelity depends on the length of time needed to take the measurements of interest. The fidelity will now be a function of hold time, and will decay according to

$$F(t) = F_0 e^{-\Lambda t} \quad (7.1)$$

in which  $\Lambda$  is the lifetime of the atoms to background gas collisions. This lifetime is on order  $10^2$  seconds for a typical BEC experiment<sup>2</sup>.

The number of (accordion lattice) sites which can be measured predominately depends on the width of the accordion and imaging lattice beams, which for a lattice of a required depth is determined by the available laser power. However, even with conservative assumptions this number will be hundreds, and quite probably thousands, of lattice sites.

## 7.4 Variations on the basic technique

### 7.4.1 Measurement of the internal state of the atoms at each site of the lattice

It should be possible to go further than to simply resolve the atoms at each lattice site—it may be possible to determine the state of the atoms at each of the sites.

To do this the atomic states should be transferred to different magnetic sub-levels with non-equal magnetic  $m_F g_F$  factors (preferably two levels of equal and opposite  $m_F g_F$ ). If a magnetic field gradient is applied to the atoms as they are in the large-period accordion lattice, which has a large period and low trapping frequency, the atoms, trapped at the minima of the combined lattice and magnetic potential, would be

---

<sup>2</sup>It is possible that the excited state fraction of the atomic sample may somewhat alter this lifetime, although this should not be a major factor due to the small fraction of the total time spent in the excited state (see table 6.2).

translated along the direction of the magnetic field with a direction and magnitude depending on the  $m_F g_F$  factor. They should be allowed to move far enough that the two (or more) states can be resolved from each other in the subsequent measurement, but not far enough that the atoms become able to hop into the next site. As the sites of the accordion lattice can potentially be made to be many microns apart, this criteria does not seem to pose a problem. The atoms would then be locked into place during the subsequent measurement by use of the imaging lattice (see Sect. 4.5).

Alternatively, if the accordion lattice confines two species of atom (and the imaging lattices and cooling light each contain the appropriate two sets of wavelengths) the species of atom at each site can be determined straightforwardly by fluorescence at the separate wavelengths.

#### **7.4.2 Lattices and superlattices**

As discussed above, the phase of lattices with parallel lattice vectors, but different spatial periods, should coincide at the centre of the accordion lattice when they are generated by correctly aligned, aberration free optical systems. Even for imperfect optical systems, the phase difference between lattices of different spatial periods should be relatively stable and predictable as the lattices share common optical elements.

This opens up the possibility of using the accordion lattice optical elements to superimpose two lattice potentials of different periods, i.e. a superlattice. This would be formed when two frequencies are used in the acousto-optical deflector. To avoid the heating of atoms due to beating of the light from the two lattices, the difference between the deflection frequencies should be much greater than the characteristic frequencies of the motion of atoms within the lattice; this limits the minimum difference in the spatial periods of the two lattices.

A lattice with a spatial period of half the spatial period of the original lattice will give the combined lattice basis of double wells; a lattice with a spatial period of a third of the original lattice will make a triple well basis, etc. Groups of sites, corresponding to the same basis site, can potentially be manipulated independently [89].

An accordion lattice setup with arbitrary control of the relative phase of lattices

with different periods can be generated by using two acousto-optic deflectors per axis in place of the single one in the original scheme (Fig. 7.3b). Each AOD would generate the beams for one side of the optical axis; control of the relative phases of the radio-frequencies within each AOD would allow arbitrary control of the phase of each component of the superlattice. In this way, a set of lattices with different frequencies and relative phases can be superimposed. The expense of this setup is a more complicated optical system which is potentially less naturally phase-stable without active correction.

### 7.4.3 Generalisation of accordion lattice geometry

Small-period accordion lattices are not limited to square counter-propagating lattice configurations. Figure 7.3 indicates how lattices of other geometries can be constructed. However, these designs shall not be pursued further in this thesis.

### 7.4.4 Using the accordion lattice to prepare a small initial sample of atoms

There may be circumstances in which it is useful to have, prior to the commencement of the quantum dynamics, a small sample of atoms prepared so that they are localised in a particular region of the potential. For example, this would allow measurements of the local quantum diffusion of ultracold atoms in a lattice (this would be particularly interesting, for example, if the potential was disordered).

The accordion lattice can be used, prior to the commencement of the quantum dynamics, to prepare such a small, localised, ultracold atomic sample. When the atoms are initially loaded into the accordion lattice, the lattice potential would be raised to suppress tunnelling, and the accordion lattice expanded (in up to three dimensions). The atoms at the edge of the accordion lattice envelope would fall away under gravity<sup>3</sup>. The accordion lattice would then be contracted back into the counter-propagating configuration. By adjusting the relative phases of the accordion lattice, the localised atomic sample would then be positioned as desired. The accordion lattice would be lowered to allow coherent tunnelling processes and the desired quantum dynamics investigated.

---

<sup>3</sup>The lattice potential could be lowered to promote this process. Tunnelling would be suppressed at this point due to the large lattice period.

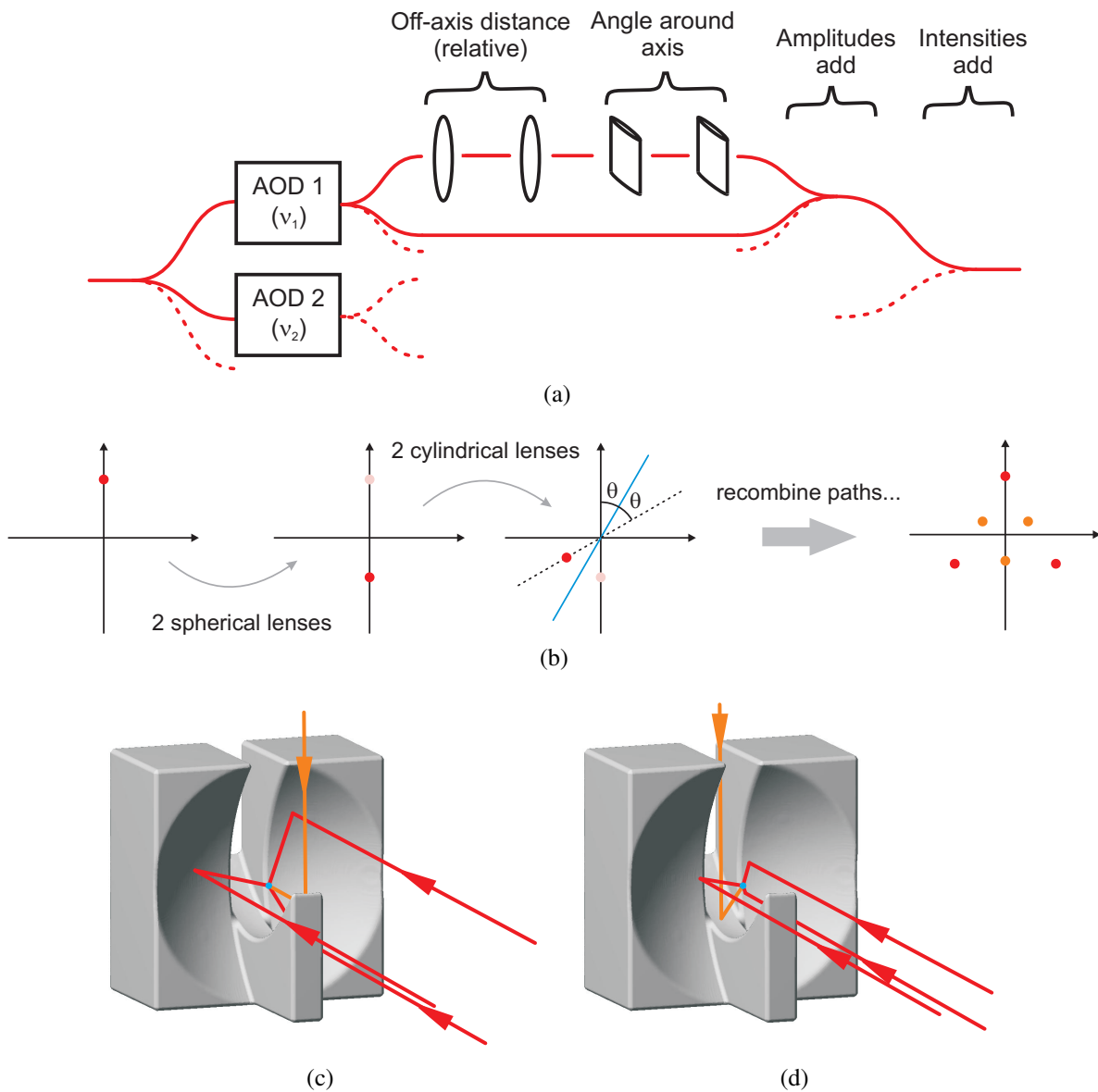


Figure 7.3: Accordion lattices of non-standard geometry. Figures (a) and (b) show a schematic representation of how a general accordion lattice can be generated. The original beam is divided various paths; there can be sets of beams which add in intensity or in amplitude, depending on whether or not they have identical frequencies. The relative off-axis distance of a single beam (and so its angle of incidence at the atoms) can be varied with a pair of spherical lenses. A rotation of a beam around the optical axis can be accomplished with a pair of cylindrical lenses; a rotation of  $2\theta$  is achieved by having the axis of the cylindrical lens making an angle of  $\theta$  with the plane defined by the original beam and the optical axis. Complex 2D lattice geometries can be built by such methods. Figures (c) and (d) show an example of how to use the above method to make a non-counter-propagating 3D accordion lattice. The tetrahedral lattice of Figure (c) is constructed from 3 parallel beams incident on the mirror from one direction, each separated by  $120^\circ$  around the optical axis, with a fourth beam incident from another direction; a single AOD generates all four beams coherently. The lattice can be expanded as shown in Figure (d) for the purposes of measurement. Again, the largest lattice period depends on the width of the slice. The beam colouring is for visual clarity.

Two- or one-dimensional samples can be prepared using a similar method. Using an accordion lattice which is capable of extremely large periods (for example, by using a transmission lens rather than a parabolic surface), and with accurate control over the relative phase at the centre of the accordion lattice, the lattice can be expanded so that atoms in a single accordion lattice plane are retained. Upon contraction of the lattice, a two or one-dimensional sample would result, which would be tightly confined in the orthogonal direction(s).

#### 7.4.5 Longer time-of-flight measurements and higher group velocity samples

The discussion of Section 7.1 neglects considerations of the velocity capture range of the accordion and imaging lattices, which will now be addressed. The initial velocity of the atoms when the first lattice (accordion or imaging) is switched on should be sufficiently low, and the lattice sufficiently deep, that the atoms are captured in the lattice.

This is a fairly easy criterion to meet for the vast majority of coherent atomic dynamics. The maximum horizontal component of the velocity in time-of-flight measurements, for example resulting from diffraction from a lattice, is set by the motional energy of atoms within a low-depth lattice; we have already established that the accordion lattice (and certainly the imaging lattice) should be deeper than these sorts of energies.

The vertical component of displacement and velocity of an atomic distribution after a time of free evolution potentially poses more difficulties. As the atoms accelerate under the influence of gravity, they leave the region of the beams, and furthermore, have a higher kinetic energy when they are captured, which may be above the depth of the lattice. To take a concrete example, the centre of an ultracold rubidium sample after a time of flight of 5 ms will have travelled around  $100\ \mu\text{m}$  vertically; the atoms will have a final kinetic energy of  $0.04\Gamma$  ( $\sim 60 E_R$ ). This will be around the limit for capture in the accordion lattice with typical beam powers and diameters; however, 5 ms is still rather short compared to the typical times of flight used in experiments.

The most straightforward way to look at coherent atomic dynamics after a longer time of flight is to use a magnetic field gradient to suspend, or slow the fall, of atoms

in a particular magnetic substate<sup>4</sup>. This would be an advantage when investigating a mix of atomic substates, as the field gradient would separate the components in time of flight, and could be tuned so that the time-of-flight distribution of a particular magnetic substate could be observed in isolation. Other methods, which may be more appropriate in certain circumstances, would be to position the atomic sample above the accordion and imaging lattice region before release (for example by movement of the magnetic trap), or to give the atoms an upward velocity before releasing them.

There is a relatively simple technique which can be used to compensate for the common (group) velocity and acceleration of a sample. The accordion or imaging lattice can move as it captures the atoms so that the mean atomic velocity is zero in the frame of the lattice while the lattice is being turned on. The accordion lattice can be made to translate by mounting a certain component of the optical system (mirror M1 of Fig. 4.2b) on piezoelectric device or precision motorised translation stage. A similar method can be used for the imaging lattice; alternatively the counter-propagating imaging lattice beams could be slightly frequency detuned from each other. Once captured, the lattice can be decelerated by use of the steepest region of the lattice potential, and the atoms would then be returned to the field of view of the detection system.

#### **7.4.6 The use of shorter-wavelength light**

The discussion of the accordion and imaging lattices has so far assumed that the laser light is in the vicinity of the strong alkali D resonances. The potential for the use of higher-energy resonances is now examined.

A major drawback to using higher-energy resonances is that, for most alkalis, they are much weaker than the D lines (by a factor of around 100 for rubidium, for example). To produce the same depth of lattice with the same laser power the frequency detuning must be divided by this factor; as a consequence, the scattering rate will increase, again by this factor. This will be a problem when coherent quantum dynamics take place in the lattice. For most experiments, it would seem better to use the longer-wavelength alkali D lines for the accordion lattice.

---

<sup>4</sup>A possible disadvantage of this technique is some distortion of the atomic distribution due to non-uniform magnetic field gradients; the gradient should be as even as possible.

For the imaging lattice there is a different issue. The imaging lattice can be brought closer to optical resonance when used near weaker lines, as the increase in scattering is not so important. However, for higher-frequency, near-resonant light, one-colour two-photon photoionisation can become a problem. Taking the example of rubidium again, a beam of  $50 \text{ W cm}^{-2}$  (Table 6.1) which is around 100 MHz off-resonance will photoionise the rubidium at a rate of around  $10 \text{ s}^{-1}$  [12, 1]; this is too fast to be of use for the types of measurements outlined in this thesis.

It could also be possible to use shorter-wavelength light as a fluorescent probe; the shorter wavelength would potentially allow greater resolution of the image. In such a scheme, the shorter wavelength light would be collected for the image at the same time as cooling takes place on the main D transition. This is not necessarily an advantage when both accordion and imaging lattices are used together, as the accordion lattice technique is designed so that the sites are resolvable when imaged using the D transition. Furthermore there are disadvantages, as there would be coherent effects in the fluorescent scattering if a radiative cascade is not used (Sect. 7.2), and furthermore the photoionisation rates may be substantial (from the high-lying excited state via photons from the imaging lattice light). However, if the imaging lattice was used without the accordion lattice, the advantages may outweigh the disadvantages as there would be a greater need of high resolution imaging. For example, an experiment using an incoherent optical lattice (see Ref. [4]) may benefit from an admixture of shorter-wavelength light while the atoms are undergoing polarisation gradient cooling, as long as the parameters are such that the photoionisation rate does not pose a problem.

In summary, although the use of shorter-wavelength transitions leads to the advantages of smaller well volume and better imaging resolution, the disadvantages, of increased scattering and photoionisation, would seem to preclude their use in many situations.

## **7.5 Comparison with the recent experiment at Harvard**

The experiment described in the preprint [4] has the potential to directly image atoms in strongly interacting quantum states, and will now be contrasted with the technique set out in the last few chapters.

A fundamental difference is the ability of technique described in this thesis to eliminate the effects of light-assisted collisions. By dividing up the original sites into hundreds or thousands of new wells, substantial populations of atoms at each site can be isolated from each other while fluorescing. The true distribution of atoms at each site can therefore be determined, rather than just the parity of the atom number.

Another significant difference is the ability to use counter-propagating lattices, generating lattice periods 300-400 nm, substantially lower than the 640 nm of this experiment. As will be discussed in Sections 8.3 and 8.4, the interaction strength of tunnelling atoms increases markedly with decreasing period; one can expect purer strongly interacting dynamics in a counter-propagating lattice.

Thirdly, the technique as described in this preprint is limited to 1D and 2D systems; the technique I propose can be used with 1D, 2D and 3D systems.

An advantage of the Harvard technique over my proposed technique is the use of a holographic mask to generate the lattice. Different masks may be easily substituted to generate different 2D lattice geometries. With my proposed technique, different lattice geometries can only be generated by reconfiguring the optical system.

## **7.6 Outline of prospects for novel physics**

In this section a few examples of the novel physics that could be investigated using the accordion and imaging lattice techniques be will be outlined. This is by no means a complete survey, as there is quite a variety of quantum phenomena which could be explored using these techniques; rather, the object of this section is to present some scenarios which demonstrate the potential power of the techniques.

### 7.6.1 Direct observation

As has been discussed in Chapter 2, the direct observation of strongly interacting physics in optical lattices is yet to be demonstrated. For a quantum system governed by the Bose-Hubbard Hamiltonian, for example, such an observation would provide stark and unambiguous evidence in a single exposure for a quantum phase transition in a bulk sample of ultracold atoms. Although good evidence has previously been presented for such a transition [28], this evidence relies on the excitation properties of the state rather than direct detection of the state itself; furthermore, in these previous experiments, the signal of the phase transition can only be determined from the combined analysis of many experimental runs, rather than from the analysis of a single sample. Direct observation of the physical state from a single atomic sample is a qualitatively different; such an observation would be very clear and almost completely unambiguous.

### 7.6.2 Structure and detail of quantum states

Direct observation would characterise the spatial structure of the state with a half-wavelength resolution at the level of single atoms. To take an example, these techniques could be used to probe the structure of the ground state of ultracold atoms in an inhomogeneous lattice potential, which is expected to take the form of co-existing regions of superfluid and insulator in the vicinity of the phase transition [42]. To take another example, lattices with complex bases (2 site [2], 3 site [84], ...) could be investigated, with the states characterised on a sub-basis as well as an intra-basis level.

Another class of phenomena which would benefit from this type of imaging would be transient phenomena, or phenomena which change during time-of-flight. An example of this would be the quantum turbulence of a BEC; as the condensate expands, the nature of the vortex interactions change, and the vortex tangle could substantially evolve during time-of-flight<sup>5</sup>. The accordion and imaging lattice method offers the possibility of locking the atomic density *in situ* prior to the measurement.

---

<sup>5</sup>In addition, the 3D nature of the measurements will be very helpful when understanding such a vortex tangle.

### 7.6.3 Correlations

The characterisation of correlations of atoms in interacting quantum systems is a very important aspect of their investigation. Correlations are a measure of the departure from a mean-field description of the states. Much of the theoretical interest in ultracold atomic matter is concerned with the investigation of these strongly correlated states; often strongly correlated systems are very hard to adequately model and understand, in particular when using *ab initio* methods.

The techniques as proposed will offer a direct way to measure and characterise such correlations in ultracold atomic systems. For example, it will enable direct measurements of the atomic correlation functions between lattice sites  $\langle n_{i,\dots} n_{i+k,\dots} \dots \rangle$  for lattices of different dimensionalities and bases, for samples of various atomic compositions, whether bosonic, fermionic, or a mixture.

### 7.6.4 Excitations and finite temperature systems

The excitation spectra of strongly interacting quantum states are potentially very complex. The techniques as described will enable various types of excitation to be detected and spatially resolved. For example, the excitation spectrum of an ultracold gas in an inhomogeneous optical lattice could be probed as a function of position. As another example, the characterisation of excitations in lattices with complex bases could be performed with a sub-basis resolution.

The discussion of strongly interacting atomic states in optical lattices is usually limited to the zero-temperature ground states. Quantum systems which have a temperature of the order of the parameters of the quantum Hamiltonian are even more complex. Using the above techniques, finite temperature systems may be studied as a quantum system with a certain population of excitations, which can be counted and characterised. This finite temperature quantum system could be an isolated system (a finite temperature atomic sample) or be composed of many small interacting quantum systems (a grand canonical ensemble).

### 7.6.5 Observation of novel phenomena with few participating particles, low atom densities, or small length scales

These techniques present a means to study phenomena that can only be observed with small atom numbers, with low atom densities or at small length scales. To take an example, the structure of a quantum state in the proximity of a single impurity atom could be studied, even if only a few atoms in neighbouring sites are affected. To take another example, a lattice could be divided up to form a large number of small interacting systems (a simple example would be a lattice of double wells [89]). The dynamics of these small quantum systems could be probed at the level of individual atoms and individual systems.

An illustrative example of a phenomenon which preferentially occurs at low atomic densities is the fractional quantum Hall effect. This can arise in ultracold atomic sample which is experiencing rotation, or some analogue of a magnetic field [43], when the two-dimensional atomic density becomes less than the two-dimensional density of Dirac ‘magnetic’ flux quanta [98, 17]; in the case of a rotating atomic sample, this ratio is given by

$$\nu = \frac{\rho h}{2m\Omega}, \quad (7.2)$$

where  $\Omega$  is the rotation frequency of the atoms. The fractional quantum Hall effect region  $\nu < 1$  occurs at low rather than high atomic densities.

A similar situation, in which low density phenomena are more interesting than high density phenomena, is found with the Tonks-Girardeau gas [76]. Standard methods such as absorption imaging may be substantially inhibited by the low number of atoms in the sample; however, the accordion and imaging lattice techniques would seem ideal to extract data from such diffuse systems.

### 7.6.6 Quantum simulation and computation

The relevance of these techniques to quantum simulation has already been covered in some detail (see Chapt. 2 and above). The question is now addressed of whether the accordion and imaging lattice techniques are useful for the more arbitrary quantum manipulations that are needed for quantum computation.

I think that it is entirely possible to demonstrate a 2-qubit quantum gate using the accordion and imaging lattices. For example, a 2-qubit collisional quantum gate [41] which relies on the exchange symmetry properties of the atoms [35] could be demonstrated in a double-well lattice (such as in [89]); used appropriately, the accordion and imaging lattices would give the ability to resolve and determine the quantum states at the individual lattice sites (see Sect. 7.4.1). It would be possible to develop this strategy further—for example, to make many copies of an isolated system of four qubits, using double well-type lattices in two orthogonal directions. In this way, small quantum computations could be carried out in parallel in a large number of isolated systems.

However, the entanglement of atoms at a single arbitrary site with another single arbitrary site would require some additional technique beyond those which have been presented in this thesis. The issue is that, whilst the accordion and imaging lattice techniques will allow good resolvability in the measurement phase of the experiment, such resolved manipulations need to be made while the quantum dynamics are still ongoing. This is potentially possible with the accordion lattice using a process of lattice expansion, resolved manipulation, and then lattice contraction before resumption of the quantum dynamics. However, the heating that will be incurred during such manipulations, and the comparatively long time needed per manipulation are likely to limit the utility of such a strategy.

---

# NOVEL TECHNIQUES TO PREPARE ULTRACOLD ATOMIC STATES SUITABLE FOR QUANTUM SIMULATION: THE MOTT INSULATOR PHASE TRANSITION AND BEYOND

This chapter presents two experimental techniques which are separate from, but potentially complimentary to, the accordion and imaging lattice techniques. The object of both of these techniques is to decrease the entropy of the starting state for the quantum simulation of a lattice Hamiltonian. Both techniques make use of radio-frequency fields; the first technique uses these fields to combine different potentials, while the second technique uses these fields to evaporate atoms from optical potentials.

## **8.1 Introduction: the importance of a reproducible starting state for quantum simulators**

Experiments to investigate the quantum dynamics of Hamiltonians need the ability to produce simple and reproducible quantum starting states. The properties of the starting state should be known with enough confidence that the properties of the final states can be attributed to the subsequent Hamiltonian evolution, and not variation in the initial state. If the effects of the Hamiltonian evolution cannot be distinguished from the uncertainty in the starting state, the system cannot perform its function as a quantum

simulator. From a quantum information perspective, starting state preparation is equivalent to the initialisation of the quantum array.

Quantum states are naturally very fragile, so it is not usually possible to measure the starting state prior to the Hamiltonian evolution; the measurement itself will typically add significant uncertainty to the state by heating and decoherence processes and so obscure the effect of the subsequent Hamiltonian evolution. Therefore efficient quantum simulation requires the deterministic preparation of a quantum starting state which varies to as small an extent as possible between runs of the experiment. Measurements on copies of the initial and final quantum states can then be performed on different runs of the experiment, circumventing the above issue.

The simplest and most fundamental starting state is a spatially homogeneous zero-temperature state, with the same number of atoms in each well of a lattice. This state cannot be obtained by simply dividing up a non-interacting BEC amongst the wells of an optical lattice: the resulting atom occupancy would be a Poissonian distribution. The Mott insulator is a commonly cited method to obtain a fixed number of atoms in each well of the lattice, since during this quantum phase transition the collisional interactions, which are non-linear in terms of the number of atoms per well, greatly suppress the width of the number distribution in each well.

The experimental process of making the Mott insulator state is not perfect. In any experiment there will be decohering processes, as briefly discussed in Section 8.4, which may stem from noise or jitter of the confining potentials, spontaneous scattering processes from the dipole trap laser beams, or inelastic collisional processes. Furthermore, the atoms loaded into the lattice will have a small thermal component, in addition to the BEC. All of these factors lead to a finite temperature in the Mott insulator, which is manifested as a population of excitations. Analysis of current experiments suggest that this temperature is non-zero and may be up to one third of  $U$  [80, 65]. Clearly, to use Mott insulator states as starting states for quantum simulation, this temperature must be reduced as much as possible, in order to increase the purity and so predictability of the quantum starting state.

The structure of this chapter is as follows. The first few sections discuss the

properties of the Bose-Hubbard Hamiltonian, particularly those of relevance to forming a pure Mott insulator starting state. A novel method is presented which can increase the effect of the collisional interactions in a lattice undergoing the Mott insulator phase transition, and so potentially increase the purity of starting states for quantum computation. The outline of a second novel method is then presented which eschews the Mott insulator transition altogether.

## 8.2 The parameters of the Bose-Hubbard Hamiltonian

The homogeneous Bose-Hubbard Hamiltonian is

$$H = -J \sum_{\langle i,j \rangle} \hat{a}_i^\dagger \hat{a}_j + \frac{U}{2} \sum_i \hat{n}_i(\hat{n}_i - 1). \quad (8.1)$$

In this equation the parameters  $J$  and  $U$ , the magnitude of the site hopping and on-site interaction terms respectively, are described in terms of the Wannier functions  $w(\mathbf{r})$ , the site-localised single particle wave functions, by [42]

$$J = \int w^*(\mathbf{r} - r_i) \left( -\frac{\hbar^2 \nabla^2}{2m} + V(\mathbf{r}) \right) w(\mathbf{r} - r_j) d^3 r \quad (8.2)$$

$$U = \frac{4\pi a_s \hbar^2}{m} \int |w(\mathbf{r})|^4 d^3 r. \quad (8.3)$$

in which sites  $i$  and  $j$  are neighbours. These formulae assume that the collisional interactions do not greatly broaden the Wannier functions, which is largely correct for few atoms per well. For a more accurate calculation, or for larger occupation numbers, collisional broadening must be taken into account, for example by using a variational method [60].

The phase diagram of the Hamiltonian is shown in Figure 8.1. The transition point between the superfluid and Mott insulator phases occurs in the homogeneous case only with commensurate lattice filling ( $\langle n \rangle$  being an integer), and can be calculated in a mean field approximation (Appendix B, [73]) to be

$$\left( \frac{U}{J} \right)_c \simeq \begin{cases} 5.8z & \text{for } n = 1 \\ 4nz & \text{for } n \gg 1 \end{cases} \quad (8.4)$$

with  $z$  as the number of nearest neighbours to each site. This simple mean field approximation is fairly accurate for three-dimensional and to some extent two-dimensional

systems; in one dimension the approximation becomes inaccurate, so other theoretical approaches must be pursued, such as density matrix renormalisation group (DMRG) methods. In one dimension, these methods predict the Mott insulator transition to be at [55]

$$\left(\frac{U}{J}\right)_c = 3.37 \text{ for } n = 1. \quad (8.5)$$

In the case that the ratio  $U/J$  is of order unity, but is not large enough to force the Mott insulator phase transition, the ground state of the Bose-Hubbard Hamiltonian is described as number squeezed. Number squeezing is the reduction in the width of the atom number distribution at each site below the number fluctuations characteristic of uncorrelated atoms in a superfluid. In the pure superfluid phase, in which all atoms are delocalised over many sites, the number fluctuations are Poissonian, of width  $\sim \sqrt{\langle n \rangle}$ . In a pure Mott insulator this fluctuation width is zero. A state is described as number squeezed if the width of the number fluctuations is less than the number width of the pure superfluid phase; the Mott insulator state is the most extreme number squeezed state.

In the inhomogeneous case, the ground state does not go immediately from a superfluid to Mott insulator, but rather has an intermediate region in which both Mott insulator and superfluid phases can co-exist (although neither of these phases will be pure). The ground state of the lattice in a harmonic trap has a characteristic layered (or ‘wedding cake’) structure, which has been probed in recent experiments [7, 23]. Furthermore, the condition on commensurate lattice filling is also lifted, and in the ground state all atoms are completely localised for high enough  $U/J$ .

### 8.3 Calculation of Hamiltonian parameters

The ground state of the Bose-Hubbard Hamiltonian depends crucially on the ratio of the on-site interaction energy  $U$  to the tunnelling parameter  $J$ , as can be seen from the phase diagram of Figure 8.1. With  $U/zJ < 1$ , tunnelling processes dominate, so the atoms are predominately in a delocalised, superfluid state. With  $U/zJ > 1$  the non-linear collisional term dominates, so atoms are increasingly localised to individual wells; the width of the atom number distribution in each well is decreased. At large enough  $U/zJ$  (see Eqn.

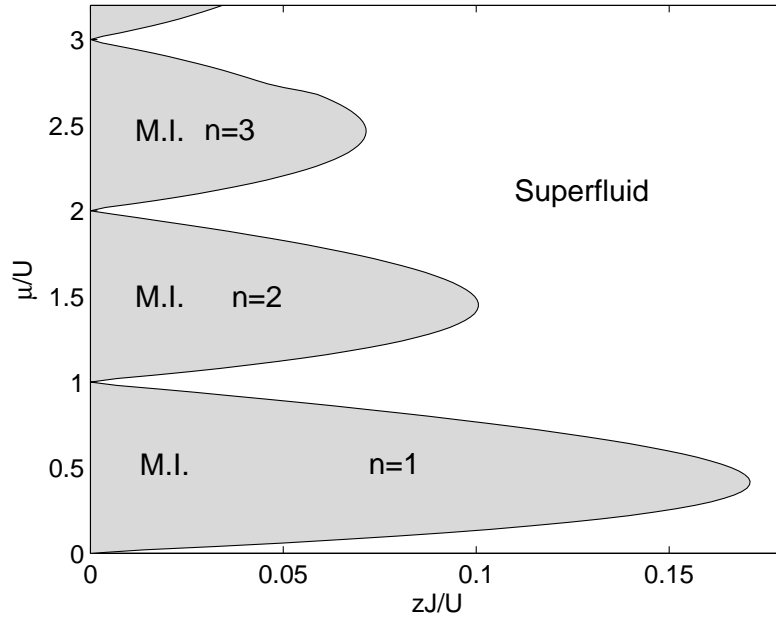


Figure 8.1: The phase diagram of the zero-temperature homogeneous Bose-Hubbard model. At low enough  $J/U$ , there is a phase transition from the superfluid phase to the Mott insulator (MI) phase; here,  $z$  is the co-ordination number. The transition parameter  $J_c/U$  can be seen to be a function of the filling factor  $n$  and the co-ordination number  $z$ . Calculated in the mean field approximation (see Appendix B).

8.4) will the system will enter the Mott insulator phase.

The parameters  $U$  and  $J$  can be calculated from the single particle Wannier functions by using Eqns. 8.2 and 8.3. Alternatively, for a sinusoidal lattice, certain approximations may be used to find an analytic form for these parameters. Whereas the harmonic oscillator approximation can usefully applied to calculate  $U$ ,  $J$  cannot be determined in this way because the harmonic oscillator wave function does not accurately describe the extended tails of the Wannier function. The parameter  $J$  can instead be calculated from the width of the lowest band of the Mathieu equation [104]. These approximations, in the case of a three-dimensional cubic lattice, lead to the analytic expressions

$$J_i = \frac{4}{\sqrt{\pi}} E_{r,i} \left( \frac{V_{0,i}}{E_{r,i}} \right)^{-\frac{3}{4}} \exp \left( -2 \sqrt{\frac{V_{0,i}}{E_{r,i}}} \right) \quad (8.6)$$

$$U = \frac{4a_s}{\hbar} \sqrt{\frac{m}{\pi}} \left( \prod_i V_{0,i} E_{r,i} \right)^{\frac{1}{4}} \quad (8.7)$$

with  $V_{0,i}$  the lattice depth in the  $i$  direction, and  $E_{r,i}$  being the lattice recoil energy in the  $i$  direction

$$E_{r,i} = \frac{\hbar^2 \pi^2}{2m d_i^2} \quad (8.8)$$

where  $d_i$  is the distance between lattice sites. The lattice recoil energy is, in general, different from the photon recoil energy

$$E_{r,phot} = \frac{2\hbar^2 \pi^2}{m \lambda^2}. \quad (8.9)$$

In the following discussion, we assume homogeneity and ignore the subscript on  $J$ .

The formulae of Equation 8.6 are only valid for  $J, U, E_{r,i} \ll V_{0,i}$ . In the case that these conditions is not satisfied, the Bose-Hubbard parameters must be numerically calculated using Eqns. 8.2 and 8.3. The Wannier functions are required for this calculation; they can be found as a sum of the Bloch functions

$$w(\mathbf{r} - \mathbf{r}_C) = \frac{1}{\sqrt{N_q}} \sum_q \phi_q(\mathbf{r}) e^{-iq \cdot \mathbf{r}_C}. \quad (8.10)$$

The Bloch functions, the eigenstates of quasi-momentum  $\mathbf{q}$ , can be found from the single particle Hamiltonian  $\hat{H} = \hat{E}_k + V(\mathbf{r})$  under application of Bloch's theorem

$$\phi_q(\mathbf{r}) = e^{iq \cdot \mathbf{r}} u_q(\mathbf{r}) \quad (8.11)$$

where  $u_q(\mathbf{r})$  is periodic upon translation by any lattice vector. The resulting modified Hamiltonian

$$\hat{H}_q u_q = \left( -\frac{(\hat{\mathbf{p}} + \mathbf{q})^2}{2m} + V(\mathbf{r}) \right) u_q = E_q u_q \quad (8.12)$$

may then be diagonalised in a plane wave basis to find the Bloch functions, and so the Wannier functions, and finally the parameters  $U$  and  $J$ .

Each Bloch function in the summation of Equation 8.10 can be chosen with arbitrary phase; this generates a set of possible Wannier functions. However, only one member of this set is localised around a particular site  $C$ . This Wannier function is called the maximally localised Wannier function (MLWF), which is commonly referred to as 'the' Wannier function, neglecting the rest of the set. In the one-dimensional case, it has been shown that the MLWF may be found by a rephasing procedure on the set of Bloch functions  $\{\phi_q(\mathbf{r})\}$  [66].

If the potential  $V(\mathbf{r})$  is separable, the wave functions factorise, and the problem is reduced to separate one-dimensional calculations. This is the case the situation we consider.

#### 8.4 Discussion of factors which can lead to impurities in the Mott insulator

If the tunnelling of atoms between wells occurs at approximately the same rate as the decohering processes, the wave function ceases to evolve unitarily according to the Bose-Hubbard Hamiltonian. This gives an effective lower limit to the lowest tunnelling rates possible in an experiment. It can therefore be seen (Eqn. 8.4) that to be able to experimentally investigate the strongly interacting Mott insulator region the interaction parameter  $U$  must be as high as possible; furthermore, the atomic density should be in the region of one to a few atoms per well.

Other parameters can determine the observed extent of number squeezing in an experiment. Having a low temperature in the initial superfluid state is important; if the initial temperature is greater than the recoil temperature of the lattice, for example, atoms will thermally populate higher bands of the lattice, and the single band Bose-Hubbard model will be inadequate to describe the atomic dynamics. For this reason, it is helpful to weaken the magnetic trap containing the BEC after the evaporation and before the BEC is loaded into the lattice; the atoms will cool adiabatically as the BEC expands<sup>1</sup>.

The degree of adiabaticity in the number squeezing process is also of great importance. Generally speaking, quantum dynamics will be adiabatic if the greatest rate of change of each Hamiltonian parameter is much less than the energy gap to the nearest neighbouring state  $E_{nr}$

$$\frac{1}{P_i} \frac{dP_i}{dt} \ll E_{nr} \quad \forall P_i. \quad (8.13)$$

Applied within the Mott insulator phase, this condition becomes  $dJ/dt \ll JU$ , as  $J$  will be the (proportionately) fastest varying parameter, and  $U$  will be the excitation energy. A more complex analysis is needed for the superfluid phase [45]; indeed it can be shown that true adiabaticity becomes very hard to achieve as the number of wells in the lattice

<sup>1</sup>This weakening process is needed in any case in order to decrease the offset between sites.

becomes large. The quasi-phonon analysis used by Ref. [45] showed that the parameter that should be minimised when ramping a cold atomic sample in a homogeneous superfluid state is<sup>2</sup>

$$\frac{1}{J\sqrt{JU}} \frac{dJ}{dt}. \quad (8.14)$$

For a lattice contained in a weak harmonic magnetic trap, the smallest Hamiltonian parameter will typically be the vibrational energy of the magnetic trap, which is of the order of a few tens of Hertz. The trap will modify the ground state. In this case, the adiabatic squeezing process will involve a significant mass flow on the scale of the entire BEC. As an additional complication, the value of  $U$  will vary across the lattice due to the profile of the laser beams making up the lattice. Both these effects will tend to push atoms radially from the centre of a blue frequency detuned lattice. It is possible to counteract the mass flow effects by increasing the frequency of the harmonic magnetic trap as the depth of the optical lattice is increased. By cancelling out major mass flow processes during the squeezing process, the degree of adiabaticity in the squeezing transition process can be increased. This method of increasing the magnetic trap frequency during the squeezing process is similar to the method employed by Greiner *et al.* [28], who adjusted the size of the envelope of their red-detuned lattice to reduce these mass flow effects.

Another consideration that will affect the observed extent of number squeezing of atoms in the lattice is the rate of decohering processes, such as spontaneous light scattering events, collisions with background gas atoms, ultracold three-body collisions, or heating due to noise. The rate of these decohering processes must be less than the tunnelling rate  $J/h$  or else the Bose-Hubbard Hamiltonian cannot adequately describe the quantum evolution, and the system can no longer be described as a coherent strongly interacting quantum system. Likewise, if the offset between two neighbouring lattice sites  $\epsilon_{ij}$  becomes of order  $J$ , the lattice bottom potential cannot be considered flat on the local scale, with consequences for the number squeezing dynamics. In a potential with

---

<sup>2</sup>The long phonon wavelength form of Equation 24 of this reference has been used; in some cases the short phonon wavelength form may be more appropriate.

random local disorder satisfying  $\epsilon_{ij} \gtrsim J$ , a Bose glass phase could form [19].

## Summary

To use the Mott insulator phase transition to make the initial state for quantum simulation and computation, care must be taken to decrease the number of impurities present in the final state; these impurities would primarily consist of atoms displaced from their expected position. From the above discussion, it can be seen that both  $U$  and  $J$  should be as large as possible during the phase transition in order to decrease the number of impurities in the final state. Since the phase transition occurs at a certain ratio of  $U$  to  $J$ , this means the value of  $U$  should be as large as possible for a given value of  $J$ .

## 8.5 RF dressing: a technique to increase the interaction strength of tunnelling ultracold atoms

This section sets out a way to increase the on-site interaction energy,  $U$ , while still maintaining slow inter-well dynamics, using the technique of radio-frequency (RF) dressing of optical potentials. The method is appropriate both for optical lattices and arrays of highly focused laser dipole spots.

### 8.5.1 Radio-frequency dressing of optical potentials

RF dressing has been used in a variety of experiments to dress magnetic potentials [37, 16, 36]. Dressing of optical potentials has received much less attention, although recently both theoretical [100] and experimental [64] studies have been carried out. A dominant feature of the recent experiment [64] was high loss rates, attributed to non-adiabatic Landau-Zener transitions [100].

RF dressing uses radio-frequency radiation to couple the magnetic sublevels of an atom. When the frequency difference between magnetic sublevels is close to the frequency of the applied RF field, the sublevels are mixed; as some tuning parameter is swept, there is a classic avoided level crossing.

The energy difference between magnetic sublevels is a function of position if the optical potential is chosen to be spin-dependant, which occurs largely when the laser frequency detuning from the D1 and D2 alkali resonance lines around the same order (or

less) than the frequency difference between the lines. The addition of a radio-frequency dressing field to a spin-dependent potential can radically change the potential. The purpose of the RF dressing field in this case is to reshape the optical lattice potential in order to increase the tunnelling rate  $J$  for a given collisional parameter  $U$ .

For simplicity of exposition, the discussion is limited to an  $F = 1$  lower hyperfine state of a bosonic atom, taken to be  $^{87}\text{Rb}$ . With the magnetic field of the applied RF perpendicular to the magnetic bias field there will be equal intensities of  $\sigma^+$  and  $\sigma^-$  RF dressing fields. A state independent lattice is chosen to confine the atoms in the  $y$  and  $z$  directions (formed with  $\pi$  polarised light, or with large frequency detuning); the difference in energy between magnetic substates is therefore independent of  $y$  and  $z$ . The Hamiltonian for these three substates is

$$H = \begin{pmatrix} V_{+1}(x) + \delta_{+1} & \Omega_{rf}/2 & 0 \\ \Omega_{rf}/2 & V_0(x) & \Omega_{rf}/2 \\ 0 & \Omega_{rf}/2 & V_{-1}(x) + \delta_{-1} \end{pmatrix} \quad (8.15)$$

with  $\delta_{\pm 1} = \Delta E_{\pm 1,0}/\hbar \pm \omega_{rf}$ . The spin-dependent optical dipole potentials  $V_{m_F}(x)$  are given in Equation 2.3.

Using a Born-Oppenheimer-type approximation ([15] p370-2), the internal and external degrees of freedom of the atom can be decoupled as long as the kinetic energy of the atoms is much less than the energy spacing of the dressed levels. This is the case for typical  $\Omega_{rf}$ , although Landau-Zener losses may occur as a result of this condition being weakly violated, will be discussed in Section 8.5.3. Under this approximation, the eigenvalues of the above matrix give the potential energy of the atoms in the corresponding dressed eigenstate. The RF coupling between the magnetic substates gives rise to avoided crossings, as shown in Figure 8.2, which shows three illustrative examples. The first two have the optical light at the wavelength such that  $2\Delta_{D_1} = -\Delta_{D_2}$ , which is 790.06 nm for  $^{87}\text{Rb}$ . This means (see Eqn. 2.3) that the  $m_F = 0$  atoms are unconfined.

The ‘truncated’ sinusoidal potential (Fig. 8.2a) can be formed a high magnetic bias field (to give a substantial non-linear Zeeman effect); the sinusoidal potential of one  $m_F \neq 0$  level is mixed with the flat  $m_F = 0$  state to give a potential sharp minima and broad maxima. The ‘interpolated’ sinusoidal potential (Fig. 8.2b) is formed at a low magnetic bias field. In this case, the  $m_F = \pm 1$  states have approximately equal and

opposite potential profiles. When mixed, they form a lattice with spacing  $\lambda/4$  (c.f. with the standard spacing of  $\lambda/2$ ).

The Gaussian array (Fig. 8.2c) is formed by an array of independently addressable tightly focussed laser beams. The neighbouring dipole traps are chosen so that they have the same intensity but opposite  $\sigma$  polarisation. The RF dressing leads to a considerable barrier between the potential minima even when neighbouring Gaussian spots are optically unresolvable.

For the ‘interpolated’ sinusoidal potential and Gaussian array the atomic spin adiabatically changes when a single atom tunnels from one site to its neighbour, potentially enabling sublattice addressability and readout.

The cases as treated have the spin dependent potential only along one direction of the lattice; dressing a spin dependent potential of more than one dimension tends to lead to structures with extended potential minima [100]. The method described may be used with or without additional tunnelling in the perpendicular directions (along spin independent potentials). A low dimensional lattice can already have a larger  $U$  than a higher dimensional lattice due to tight confinement being possible along the perpendicular directions.

### 8.5.2 Calculation of Hamiltonian parameters

The one-dimensional Wannier functions for the lowest eigenstate of the Hamiltonian (Eqn. 8.15) corresponding to the local ground state of the atoms can be calculated. Firstly, the spatially varying energy of the lowest eigenstate of the Hamiltonian is calculated and the Fourier transform of this potential is taken. This allows the diagonalisation of the Bloch Hamiltonian (Eqn. 8.12) in a plane wave basis. The maximally localised Wannier functions at the lattice sites are found by recursively rephasing the eigenstates [66] before summing over quasi-momentum (Eqn. 8.10). From the lowest band Wannier functions the Bose-Hubbard parameters can be calculated as

$$U = 2a_s\hbar\sqrt{\omega_{\perp 1}\omega_{\perp 2}}\int|w_0(x)|^4dx \quad (8.16)$$

$$J = \frac{1}{N_q}\sum_q E_q e^{iqx_r} \quad (8.17)$$

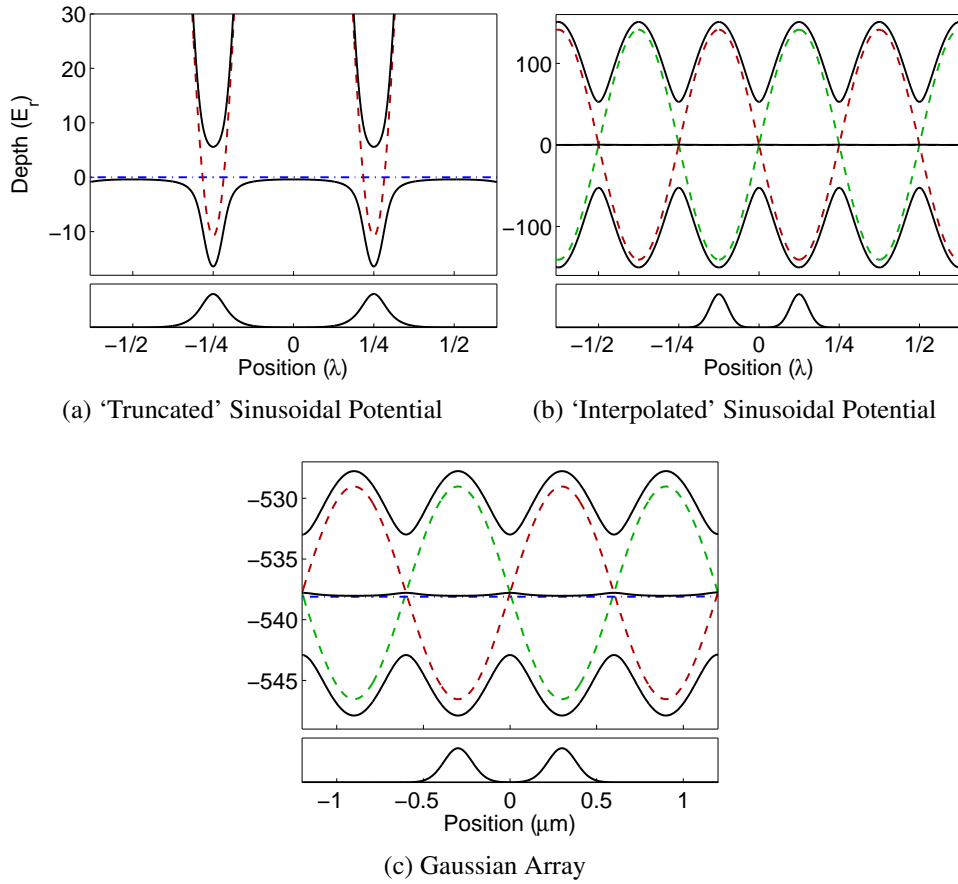


Figure 8.2: The types of RF dressed potentials considered in this section. Dressed potentials are solid black lines, undressed potentials are broken lines [ $m_F = +1/-1$  (green/red dashed), 0 (blue dash-dotted)]. The Wannier functions for the lowest state are displayed below the potentials for two of the wells. The  $m_F = +1$  state of (a) is at an energy substantially higher than the states shown. The optical lattices of (a) and (b) have  $\sigma^+$  polarisation. The recoil energy is defined as  $E_r = \hbar^2/2m\lambda^2$ . Parameters: (a)  $\lambda = 790.06$  nm,  $B_0 = 300$  G,  $\nu_{rf} = 213.65$  MHz,  $\Omega_{rf}/2\pi = 70$  kHz,  $P = 32$  mW,  $w_0 = 50$   $\mu$ m,  $\nu_{\perp 1,2} = 30$  kHz (b)  $\lambda = 790.06$  nm,  $B_0 = 4$  G,  $\nu_{rf} = 3.295$  MHz,  $\Omega_{rf}/2\pi = 270$  kHz,  $P = 35$  mW,  $w_0 = 50$   $\mu$ m,  $\nu_{\perp 1,2} = 30$  kHz (c)  $\lambda = 800$  nm,  $B_0 = 4$  G,  $\nu_{rf} = 2.78$  MHz,  $\Omega_{rf}/2\pi = 25$  kHz,  $P = 25$   $\mu$ W,  $w_0 = 1$   $\mu$ m,  $\nu_{\perp 1,2} = 30$  kHz,  $\Delta x = 0.6w_0$

with  $\omega_{\perp 1,2}$  the trapping frequencies in the perpendicular directions,  $q$  and  $E_q$  the quasi-momentum and energy of the eigenstate,  $x_r$  the separation between neighbouring lattice sites, and  $a_s$  the scattering length in the dressed state (for  $^{87}\text{Rb}$ , approximately equal to the undressed scattering length as  $a_s \approx a_t$  [81]). The photon scattering rate is calculated from the Wannier functions and details of the dressed potential.

The on-site interaction energy is compared, for a certain value of Hubbard  $J$ , between the dressed and undressed potentials. We choose  $J/h = J_{lim}/h = 25$  Hz so that the tunnelling time  $\tau_{tun} = h/2zJ$  is  $\tau_{tun} = 10$  ms ( $z$  being the coordination number). This tunnelling time is chosen so that slow coherent inter-well dynamics still occur on a typical experimental time scale; if  $J$  is decreased much further the phase transition will go from being an adiabatic to a non-adiabatic process because of the increasing role of decohering processes (see Sect. 8.4). When the quantum state decoheres, inter-well dynamics will tend to be inhibited, with the final purity of the Mott insulator depending on  $U_{lim}$ , the value of  $U$  when  $J = J_{lim}$ .

### 8.5.3 Discussion of results

The lowest adiabatic potential of the ‘truncated sinusoidal’ case (Fig. 8.2a) differs greatly from a sinusoidal shape, with ‘pockets’ of strong confinement separated by an almost flat potential. One would expect that this tight confinement would increase the collisions at each lattice site, while also encouraging tunnelling between lattice sites due to the truncated maxima of the potential. The potential is such that there is typically only a single bound state at each site. The enhancement of  $U_{lim}$  for the chosen value of  $J_{lim}$  is given in Figure 8.3a for  $\Omega_{rf} = 2\pi \times 70$  kHz and  $2\pi \times 10$  kHz; the maximum increase in  $U_{lim}$  is around 70% and 80% respectively. The enhancement factor is only weakly dependent on  $\Omega_{rf}$  for a large range of RF power.

The ‘interpolated sinusoidal’ potential (Fig. 8.2b) halves the distance between neighbouring sites of the lattice. The enhancement of  $U_{lim}$  in this potential is given in Figure 8.3b; the typical increase is around 150%.

The for the Gaussian array (Fig. 8.2c), the enhancement of  $U_{lim}$  is shown in Figure 8.3c; the maximum enhancement due to the dressing is around 80%. To use the

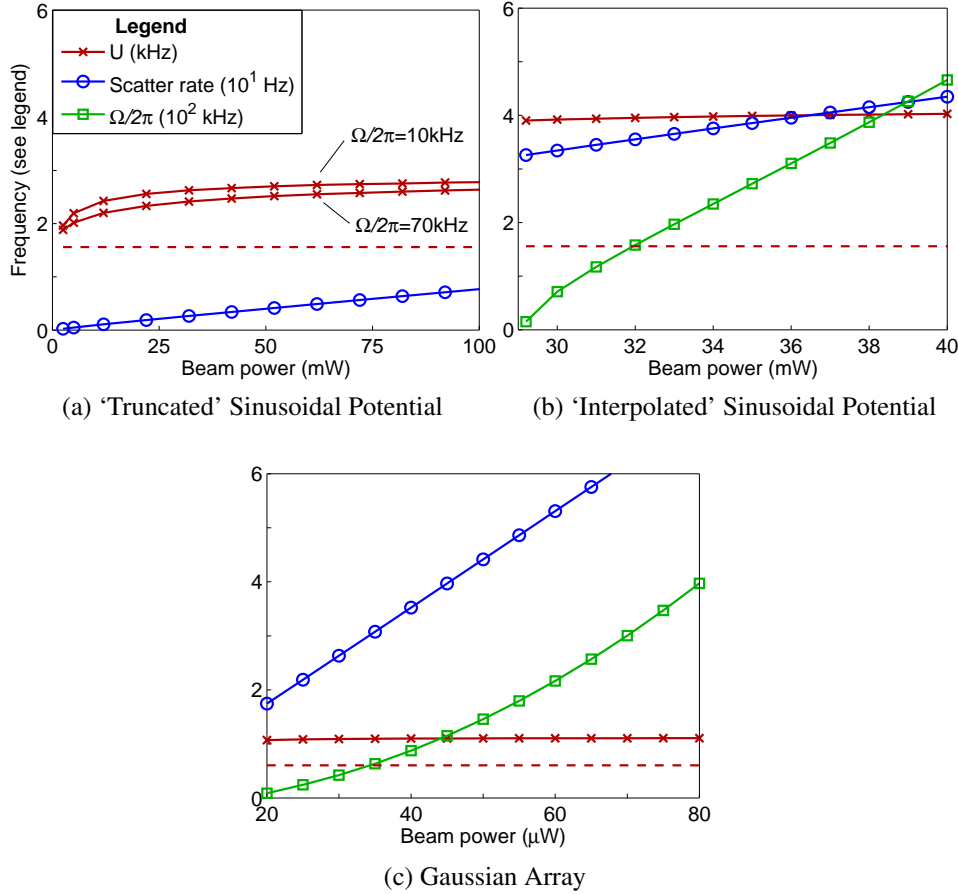


Figure 8.3: Calculated properties of atoms in the ground state of the dressed potentials. The optical power  $P$  is the independent variable; dressing parameters  $\nu_{rf}$  and  $\Omega_{rf}$  are chosen subject to the conditions that the neighbouring wells are the same depth and that the tunnelling parameter  $J/h$  is 25 Hz. These conditions specify  $\nu_{rf}$  and  $\Omega_{rf}$  for (b) and (c). For (a) the conditions only specify  $\nu_{rf}$ , so  $\Omega_{rf}$  can be chosen arbitrarily; two choices are shown. The dashed horizontal line gives the undressed  $U$  for comparison, a single value calculated for  $J/h = 25$  Hz in the undressed  $\sigma^+$  or  $\sigma^-$  potential. The scattering rates are from the dressed lattice beams only. Aside from  $P$ ,  $\nu_{rf}$  and  $\Omega_{rf}$ , the parameters of the potentials are as given in Figure 8.2.

Wannier function method we assume that the region of interest is far enough away from the edge of the array that we can neglect the finite array size.

The results of these calculations show that the dressed  $U_{lim}$  is largely independent of the optical power, but is dependent on the scheme. The results for the ‘truncated’ sinusoidal potential show that radically altering the shape of the periodic potential, to confine tighter while still allowing tunnelling, but without changing the distance between wells, can only increase  $U_{lim}$  by a modest amount. On the other hand,  $U_{lim}$  becomes substantially larger if atoms are confined in the ‘interpolated’ sinusoidal potential, with neighbouring wells separated by  $\lambda/4$ . The interpolation method would therefore seem the most promising way to increase  $U_{lim}$  by RF dressing an optical lattice.

The results show that the on-site interaction energy of atoms confined in a focussed Gaussian array can also be increased by the interpolation technique. The typical values of  $U_{lim}$  in this case are not greatly less, for our chosen parameters, than for atoms in an undressed 3D counter-propagating lattice. This raises the prospect of site-addressable highly number squeezed states in a hybrid focussed Gaussian / 2D optical lattice apparatus, with a comparable on-site interaction energy per atom to that observed in a Mott insulator in a 3D optical lattice [28].

Even a modest increase in  $U_{lim}$  could be useful as the number of imperfections is likely to be a strong function of  $U_{lim}$ . Estimates of the thermal excitations would be  $n_{th} \approx Ae^{-\frac{U}{kT}}$  (the  $J \ll U, kT \ll U$  limit of the Bose-Einstein distribution) and of non-adiabatic excitations  $n_{na} \approx Be^{-CU^2}$ ; the latter from the form of the Landau-Zener avoided crossing transition probability [102] in the limit  $J \ll U \approx \epsilon_{01}$ , where  $\epsilon_{01}$  is the energy difference between the ground and first excited states of the many body system. In both cases, the number of excitations would be exponentially suppressed by the increase in  $U$  at the phase transition.

The loading of atoms into these potentials (when  $J > U$ ) is a bit more complicated than for a standard optical lattice. Adiabatic loading of the ‘truncated’ sinusoidal potential can be seen to be accomplished by simply increasing the RF frequency once atoms are trapped in the bare lattice. Adiabatic loading of the ‘interpolated’ sinusoidal potential and Gaussian array would be accomplished by ramping the laser intensity (with

the RF already on), but the mechanism is less obvious. In effect, during the final stages of the ramping of the lattice intensities, the atoms will adiabatically delocalise between the two sets of potential minima as long as the rate of change of the offset between the two sublattices  $\epsilon_i$  is much less than the other Hamiltonian parameters.

It is important to note that spin-changing collisions and other 2-body collisional loss rates are greatly suppressed for atoms trapped in the lowest eigenstate [69, 93, 37]. This is because a collision which changes the internal states of the atoms needs an input of energy which is significantly greater than the energy available from kinetic or potential energy (of order  $J$  or  $U$ ).

The other possible loss mechanism is Landau-Zener losses arising from atomic motion at the avoided crossings, which have dominated the only RF dressed optical potential experiment carried out to date [64]. However, Landau-Zener losses become negligible when the atoms are trapped in the lowest eigenstate, as the transition from the lower to the upper dressed level needs energy which is required to come from the kinetic energy of the atoms; this kinetic energy  $\sim J$  is typically very much less than  $\Omega_{rf}$ , so Landau-Zener losses can be expected to be negligible for atoms in the lowest trapped state.

A remaining loss mechanism, specific to the truncated lattice, is the coupling of weakly bound states to the continuum. This can only occur when the highest energy state in the lowest band becomes greater than the binding energy of the site. When  $n_i U$  and  $J$  are significantly less than the binding energy of the site, as is the case in the examples given above (assuming around one atom per site), this loss mechanism is, to a large extent, suppressed; however with higher numbers of atoms per site there is a chance that some atoms will be ejected from the lattice.

The calculations shown do not specify whether tunnelling is proceeding in the perpendicular (spin-independent) directions;  $J$  along the dressed lattice direction is independent of  $J$  in the other directions. The lattice parameters in the other directions only influence  $U$  through a multiplicative factor in Equation 8.16. Therefore, when there is tunnelling in all directions in such a lattice, the enhancement factor for  $U$  arising from dressing along a single direction will be the same whether or not there is also tunnelling

in the perpendicular directions. Thus this technique could be used in a 3D lattice (composed of 1D spin-dependent and 2D spin-independent lattices), to enhance  $U_{lim}$  by the same factor as in purely 1D lattices.

If spin-dependent potentials are present along more than one direction, the 2D or 3D RF dressed potential cannot be simply expressed as a sum of 1D potentials; one consequence is that the potential minima occur along lines or surfaces rather than at points; a short discussion is found in Reference [100].

A practical complication with this scheme, in common with other RF dressed optical potential schemes, lies in the use of magnetic field sensitive transitions. The typical magnetic field drift in a laboratory environment is of order  $\sim 1$  mG [6]; this would manifest as a sublattice-dependent energy offset of order  $\sim 1$  kHz. Clearly this site-dependent offset needs to be less than  $U$ ; practically this would mean using a magnetic shielding technique such as mu-metal cladding, which can decrease these ambient fields by a factor of around 100 [75].

In conclusion, a substantial enhancement of on-site interactions can be achieved by RF dressing optical potentials; the purity of the resulting Mott insulator state should be improved by the use of this technique.

There are variety of other methods which can be adapted to increase on-site interactions in a lattice, including tunable scattering lengths and Feshbach resonances [94, 39], and other methods proposed to give sub-half-wavelength structure to optical lattices, for example Raman processes [33, 103].

## 8.6 Inter-line optical trap evaporation

I have been developing a further method to prepare a pure quantum starting state which does not rely on the Mott insulator transition. Instead, it relies on an evaporation process to transfer states with energy over a certain value into untrapped (continuum) states. This method offers the possibility that the quantum starting state can be directly prepared from a cold sample of atoms with non-zero temperature.

The dynamics of the Mott insulator transition rely on atoms being able to tunnel between lattice sites. For tunnelling to occur, it is required that the tails of one Wannier

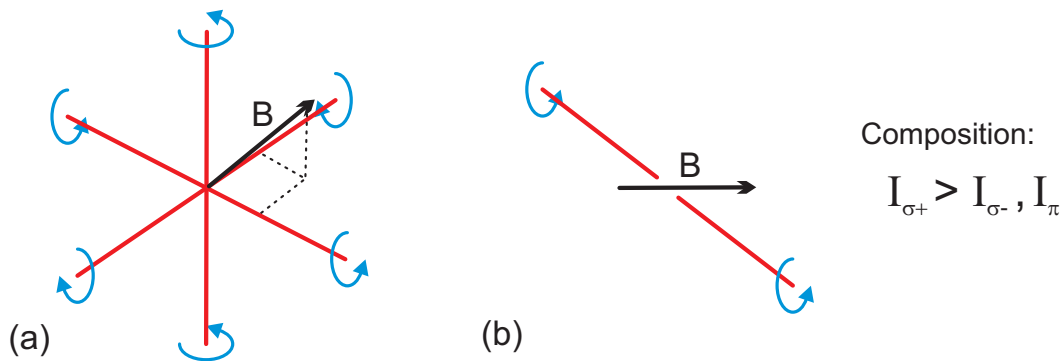


Figure 8.4: Making a spin-dependent lattice suitable for inter-line optical trap evaporation (ILOTE), or an immersed optical lattice [29], in the standard  $\lambda/2$  cubic lattice geometry. Figure (a) shows possible arrangements for the lattice beams and magnetic field; each counter-propagating pair of lattice beams would be frequency detuned from the other pairs, as is standard practice. Figure (b) shows the effective optical fields along the B field (the quantisation axis); the intensity of  $\sigma^+$  in the lattice is greater than the other two polarisations. At the optical frequency such that  $2\Delta_{D_1} = -\Delta_{D_2}$ , the  $\pi$  light does not trap the atoms, and the  $\sigma^-$  light counterbalances an equal amount of  $\sigma^+$ ; the nature of the resultant lattice therefore has  $\sigma^+$  character for all three sets of beams. Other configurations can give the same effect, in particular  $n+1$  beam configurations to form a lattice in  $n$  dimensions.

function overlaps with the Wannier functions of neighbouring sites. This contradicts the requirement for a large collisional energy  $U$ , which is that each Wannier function must have as small a spatial extent as possible. One advantage of not using the Mott transition is that a much tighter optical potential can be used, to confine the atoms tighter and so generate a greater collisional parameter  $U$ ; this would further discriminate against impurities.

Evaporation is not commonly used for atoms in optical potentials. This is because, in general, optical potentials confine atoms in every magnetic and hyperfine sub-level of the ground state manifold, so a transition from a trapped state to a stable continuum state is not possible. However, for a particular wavelength between the alkali D lines, the  $m_F = 0$  states become untrapped whilst the  $m_F \neq 0$  states can still be trapped, as can be seen from Equation 2.3 (and as discussed in Sect. 8.5.1). In the presence of gravity the  $m_F = 0$  atoms will fall away from the trapping region. More detailed consideration shows that such a state-dependent lattice (which can be used as an immersed lattice [29]) can also be constructed in three dimensions (see Fig. 8.4).

Radio-frequency transitions can then be used to selectively transfer atoms to the continuum, based on their energy. This could be used for the classic evaporative cooling process of a thermal sample (Fig. 8.5(a)), in which the atoms in the highest energy states are removed from the well. In the right circumstances, the remaining atoms in the well will rethermalise amongst the available states, lowering the temperature of the remaining atoms; the process can then be repeated. This is analogous to the commonly used technique of evaporative cooling in a magnetic trap. Small optical dipole traps would be much tighter and deeper, giving a much larger level spacing; consequently fewer atoms can be present in the trap, as too many atoms would lead to a large 3-body loss rate.

Besides the evaporation of a thermal sample, this process can be used to select the number of atoms in the vibrational ground state of the well (Fig. 8.5b). The interaction energy of  $N$  bosonic atoms in the ground state of the well is  $UN(N-1)$ ; a state with  $N+1$  atoms has a higher interaction energy than a state with  $N$  atoms. If the radio-frequency intersection is tuned so that the higher energy states have enough energy to escape to the continuum, while the lower energy states do not, then the number of atoms will decrease only if there are greater than a certain number of atoms in the well. In this way, evaporation may be performed to reach a desired number of atoms in the well, as long as there are at least that number of atoms in the ground state of the well to start with. As the process described does not require tunnelling between wells, the lattice potential can be very deep and tight, thus making the collisional energy  $U$  for this process greater than during a Mott insulator transition.

The evaporation rates for one and two identical bosonic atoms at a site can be derived from Fermi's Golden Rule No. 2

$$R_{i \rightarrow j} = \frac{2\pi}{\hbar} |\langle f | V | i \rangle|^2 \rho \quad (8.18)$$

and shown to be

$$\begin{aligned} R_{2 \rightarrow 1} &= \frac{\pi \Omega_{rf}^2}{\hbar} \left| \int \phi_i^*(\mathbf{x}) \phi_t(\mathbf{x}) d^3 \mathbf{x} \right|^2 \left( \int \left| \int \phi_i^*(\mathbf{x}) \phi_u(\mathbf{x}; E, \boldsymbol{\kappa}) d^3 \mathbf{x} \right|^2 \rho(E, \boldsymbol{\kappa}) d^2 \boldsymbol{\kappa} \right) \\ R_{1 \rightarrow 0} &= \frac{\pi \Omega_{rf}^2}{2\hbar} \left( \int \left| \int \phi_i^*(\mathbf{x}) \phi_u(\mathbf{x}; E, \boldsymbol{\kappa}) d^3 \mathbf{x} \right|^2 \rho(E, \boldsymbol{\kappa}) d^2 \boldsymbol{\kappa} \right). \end{aligned} \quad (8.19)$$

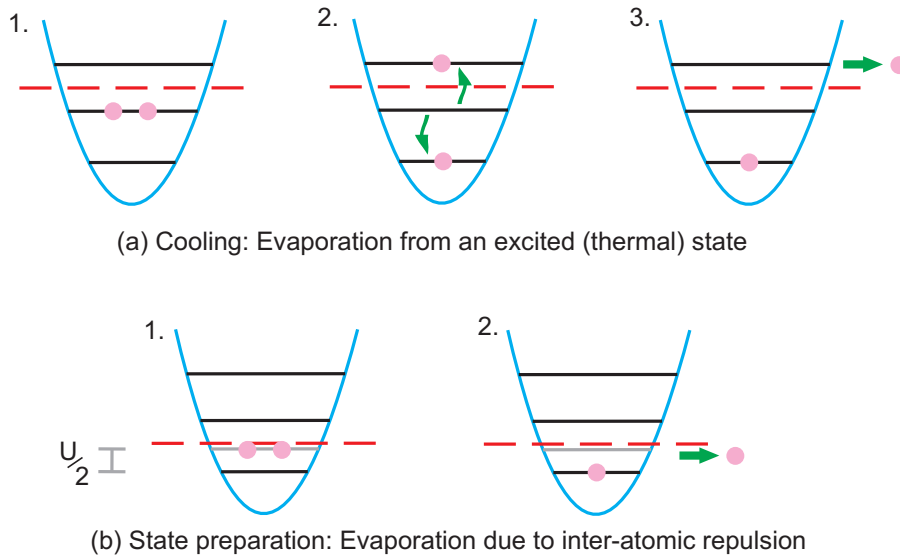


Figure 8.5: The inter-line optical trap evaporation (ILOTE) technique for bosons. Bosonic or fermionic atoms can be used; processes for fermionic atoms in one or two spin states are similar. Single particle energy levels are shown. (a) ILOTE as used to cool an excited state. The two atoms shown are mixed into different vibrational levels by the interatomic collisions. The atom with energy greater than the radio-frequency (RF) intersection can then escape the trap by a transition to the untrapped  $m_F = 0$  state. (The RF intersection corresponds, in the dressed atom picture, to the energy of a stationary untrapped atom.) This is a cooling process as the average energy of the remaining atoms is reduced. Only two atoms are shown participating in this process, but there can be more in the atomic sample. (b) ILOTE as used to prepare a definite number state. The repulsive interaction between the atoms raises the energy of the 2-atom ground state by  $U$ . By placing the RF intersection at an energy between this state and the non-interacting ground state, over time a singly occupied ground state is deterministically prepared. The process can be used to prepare a number state of any number, assuming that at least this many atoms are present in the initial ground state.

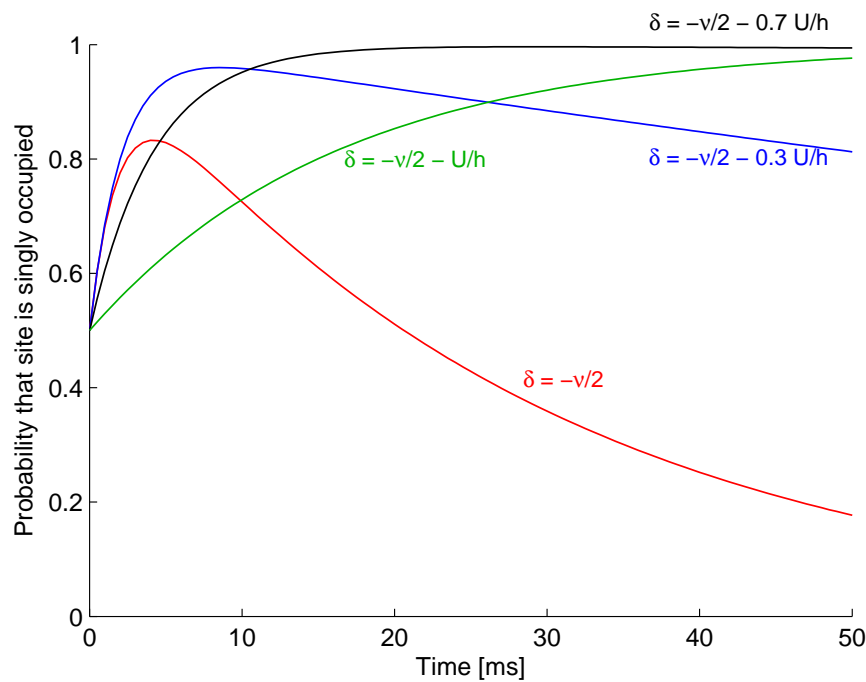


Figure 8.6: The result of the evaporation process as used to purify a mixture state. For this simulation, the starting quantum state is a mixed state containing 50%  $n = 1$  and 50%  $n = 2$  bosonic atoms at a site. The trajectories give the probability of the site having the pure  $n = 1$  state after a period of evaporation. The four trajectories show the outcome of the process using different frequencies of the applied RF; throughout this discussion we define the detuning frequency  $\delta$  as relative to the frequency of the transition  $|m_F \neq 0\rangle \rightarrow |m_F = 0\rangle$  in the absence of any optical potentials. This calculation has been performed in three dimensions, and includes the effect of gravity. The non-zero evaporation rates of the single atom state when  $\delta = -v/2$ , and the double atom state when  $\delta = -v/2 - U/h$ , are due to the effects of gravity; the atom can escape by a downwards quantum tunnelling process. The parameters used for this calculation are  $\nu = 30$  kHz (the vibrational frequency of the trap),  $U = 2$  kHz and  $\Omega_{rf} = 1$  kHz. The effects of exchange symmetry, spin-changing collisions, and the perturbative effect of the trapped atom on the wave function of the untrapped atom are incorporated into these calculations.

Here, the subscripts  $i$ ,  $t$  and  $u$  refer to the initial, final trapped and final untrapped single particle wave functions, and  $\kappa$  uniquely specifies the quantum state of the evaporated atom which has energy  $E$ . The influence of gravity and the effect of interatomic interactions, both inelastic and spin-changing, must be included to calculate an accurate figure for the rates; Figures 8.6 and 8.7 show the results of such a calculation.

It can be seen in Figure 8.6 that there exists an ideal range for the RF frequency detuning  $\delta$ , for which a mixture state of one and two atoms per site is reduced to a nearly pure state of one atom per site on a time scale of 10 ms. Outside this range, if  $\delta$  is too small, the  $n = 1$  state begins to evaporate, too; conversely, if  $\delta$  is too large, the rate of the purification process becomes very slow.

The simultaneous 2 atom escape channel is energetically prohibited (in the absence of gravitationally induced tunnelling) if the frequency of the applied RF is  $\delta < -\nu/2 - U/2h$ . Even if the RF frequency is such that this channel is not energetically prohibited, the rate of such a simultaneous escape is typically much less than the single atom escape due to a smaller overlap integral.

The relative performance of the technique against the frequency of the trap  $\nu$  is shown in Figure 8.7. The data is shown at constant RF Rabi frequency  $\Omega_{rf}$ , and with RF frequency detuning such that  $\delta = -\nu/2 - 0.5 U/h$ . The rate of both transitions falls with increasing  $\nu$ , but the rate of the unwanted transition falls much faster. The decrease in the rate  $R_{1 \rightarrow 0}$  can be simply explained by the suppression of downward quantum tunnelling from the trap at high trap frequencies, due to the decrease in the relative influence of gravity. The rate  $R_{2 \rightarrow 1}$  also decreases with increasing  $\nu$ ; this stems from the decrease in the matrix element of the transition as  $\nu$  is increased, due to the smaller spatial extent of the trapped wave function; this outweighs the increase in the phase space density of the untrapped atom. However, it is still possible to increase the rate  $R_{2 \rightarrow 1}$  as  $\nu$  is increased, by a corresponding increase in  $\Omega_{rf}$ <sup>3</sup>.

Figure 8.7 shows that this technique can produce a pure state from a mixed state in a few milliseconds with a high probability; this would be of use for deterministic

<sup>3</sup>The condition  $\Omega_{rf} \ll 2\pi\nu$  is assumed; if this is violated, the spatial wave function will become perturbed by the RF field, and unwanted transitions may result. Therefore, as  $\nu$  is increased, there is scope to increase  $\Omega_{rf}$  in proportion to  $\nu$ , without increased perturbation of the trapped wave functions.

state preparation. The limitation in this technique lies with the properties of the initial distribution of atoms. As no atoms are exchanged between wells, if the initial state has zero atoms in the well, there will be a defect in the final state. For a Poissonian distribution with mean atom occupation  $\langle n \rangle$  the zero-occupation probability is

$$P_0 = e^{-\langle n \rangle} . \quad (8.20)$$

This technique shows good promise in circumstances in which it can be guaranteed that there is at least a single atom in each well at the start of the process. There are two situations in particular in which this would be the case. The first is if the initial state is a number squeezed distribution (with mean atom number per well greater than one); the ITOLE technique can then be used as a further purification step to remove defects. The second is if the initial state is a (possibly thermal) Poissonian distribution of atoms with high mean occupation number; for example, with  $\langle n \rangle = 9$ ,  $P_0 \simeq 10^{-4}$ , and a quantum state can be prepared with very few defects.

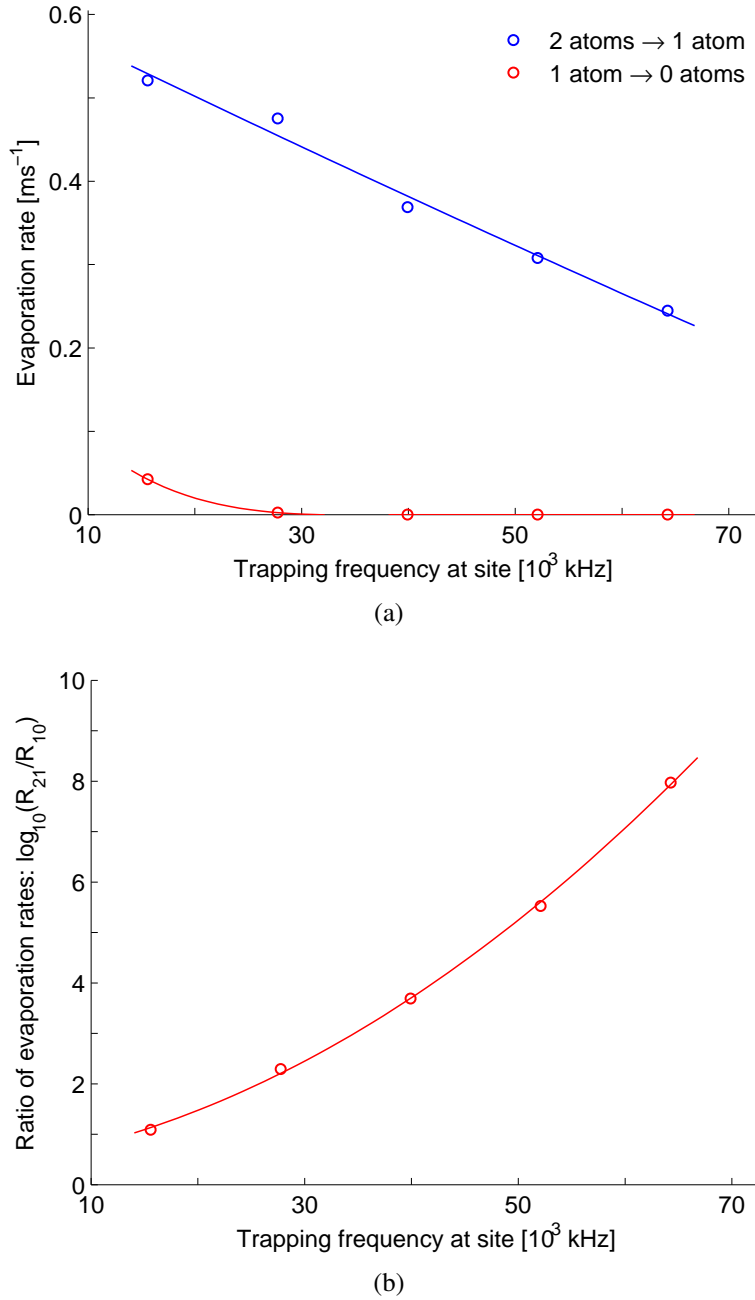


Figure 8.7: The performance of the inter-line optical trap evaporation (ILOTE) technique, relative to the trap frequency  $\nu$ . (a) The evaporation rates as a function of the trap frequency. (b) The logarithm of the ratio of the evaporation rates  $R_{2 \rightarrow 1}$  and  $R_{1 \rightarrow 0}$ . For the purposes of these plots, the calculations are performed in three dimensions, including the effects of gravity, exchange symmetry, spin-changing collisions and interatomic repulsion. Throughout, the RF Rabi frequency is kept constant ( $\Omega_{rf} = 1$  kHz) and the frequency detuning is set at  $\delta = -\nu/2 - 0.5 U/h$ . Note that  $U \propto \nu^{3/2}$  (Eqn. 8.7).

---

## CLOSING REMARKS

During the period of my DPhil I have carried out both theoretical and experimental research with the primary aim of developing techniques to probe strongly interacting many-body quantum systems in periodic potentials at the resolution of individual atoms. This has involved experimental work, to build a Bose-Einstein condensation apparatus, and to optimise the apparatus to make the condensates. In addition, I have developed several techniques during the course of my DPhil which should be of immediate relevance to the nascent field of quantum simulation, primarily dealing with the direct and precise observation of many-body quantum states at single-site and single-atom resolution, along with some work on the preparation of pure many-body starting states for quantum simulation.

In order to probe strongly interacting quantum systems of ultracold atoms at single atom resolution, I have developed two complimentary techniques. The accordion lattice, an optical lattice which can be dynamically altered on the millisecond time scale, allows quantum tunnelling between sites at small separations, but is also able to quickly separate the lattice sites, so that each site can be resolved in the subsequent measurement. Lock-in lattice fluorescent imaging offers a way to dramatically increase the signal from individual atoms in an ultracold atomic sample, whilst greatly suppressing inelastic light-assisted collisions, which plague all previous measurements of this type; as such it has the capability of mapping the spatial distribution of dilute samples of ultracold atoms with unprecedented confidence.

During my work on these techniques it has gradually become apparent to me that there is potential to use these techniques not only to directly probe strongly interacting ultracold atoms in optical lattices, but also to probe arbitrary samples of ultracold atoms, whether in a lattice, another type of optical trap, a magnetic trap, or expanding in free space. The accordion and imaging lattice techniques are most useful when they are used to probe a small volume of this arbitrary atomic distribution, containing perhaps a few hundred to a few thousand atoms. Within this volume, the potential spatial and number resolution of these techniques is impressive, as is the ability to view the spatial distribution in three dimensions. In my assessment, the development of such techniques (for atoms confined in lattices or otherwise) is the most significant part of my DPhil work.

Furthermore, I have developed two methods to increase the purity and predictability of the starting states for quantum simulation. Both these methods rely on increasing the interaction energy of atoms trapped at a site of an optical lattice, as a way to select a specific number of atoms per lattice site. Radio-frequency dressing of an optical lattice can be used to increase the interaction energy of atoms as they undergo a transition from a superfluid to Mott insulator state by the manipulation of the shape of the lattice potential between the sites. Alternatively, by using the technique of inter-line optical trap evaporation, a definite number state can be prepared in the ground state of each well of a lattice from a thermal starting state, by a process that involves the evaporation of atoms residing in higher energy and number states.

I expect that aspects of the techniques I have developed during my DPhil will, in the near future, be implemented on experiments within the Oxford ultracold atomic physics research group, and further afield. In particular, once the accordion and imaging lattice techniques have been successfully demonstrated in an experiment, a wide variety of strongly interacting quantum lattice systems will be opened to detailed study, as outlined in Chapter 2.

I hope that these techniques will become useful tools for probing the substantial complexities of strongly interacting many-body quantum systems.

**Publications**

Part of the work I have carried out during the period of my DPhil has already been published; I will submit further publications over the next few months. Of the papers that have already been published, the basic design of a electro-optically controlled accordion lattice is set out in Reference [99], and the effect of RF dressing on the tunnelling properties of atoms in optical lattices is set out in Reference [91]. I anticipate writing two papers on the direct imaging techniques using the accordion and imaging lattices; one of these will be more theoretical description of the system (including a description of the extended version of the Monte Carlo technique), and the other focussing on the experimental design. In addition, I am writing a paper with my supervisor on the effects of exchange symmetry in collisional 2-qubit quantum gates, which I expect to be published in the American Journal of Physics.

---

## ABBREVIATIONS AND TERMINOLOGY

---

Abbreviation	Full name
AOM	Acousto-optic modulator
AOD	Acousto-optic deflector
BEC	Bose-Einstein condensate
CCD	Charge-coupled device
CMOT	Compressed magneto-optic trap
DMRG	Density matrix renormalisation group
ILOTE	Inter-line optical trap evaporation
MI	Mott insulator
MLWF	Maximally localised Wannier function
MOSFET	Metal oxide semiconductor field effect transistor
MOT	Magneto-optic trap
NA	Numerical aperture (of a lens)
OBE	Optical Bloch Equations
QMCW	Quantum Monte Carlo wave function (method)
RF	Radio-frequency
SF	Superfluid
TA	Tapered amplifier (laser diode)
TOF	Time of flight (measurement)
UV	Ultra-violet
1(2,3)D	One (two, three) dimensions / dimensional

---

---

## THE BOSE-HUBBARD MODEL IN THE MEAN FIELD APPROXIMATION

The homogeneous, zero-temperature Bose-Hubbard model may be easily solved in the mean field approximation. The true Hamiltonian, expressed in the grand canonical form, is

$$H = -J \sum_{\langle i,j \rangle} \hat{a}_i^\dagger \hat{a}_j + \frac{U}{2} \sum_i \hat{n}_i(\hat{n}_i - 1) - \mu \sum_i \hat{n}_i. \quad (\text{B.1})$$

We replace the operators  $\hat{a}_i$  by fluctuation operators about the expectation value  $\hat{\delta}_i = \hat{a}_i - \langle \hat{a}_i \rangle$ . When in the mean field approximation we discard terms depending on the product of fluctuation operators, and subsequently re-substitute for  $\hat{a}_i$ , to obtain the mean field Hamiltonian

$$H = -J \sum_{\langle i,j \rangle} (\hat{a}_i^\dagger \langle \hat{a}_j \rangle + \langle \hat{a}_i^\dagger \rangle \hat{a}_j - \langle \hat{a}_i^\dagger \rangle \langle \hat{a}_j \rangle) + \frac{U}{2} \sum_i \hat{n}_i(\hat{n}_i - 1) - \mu \sum_i \hat{n}_i. \quad (\text{B.2})$$

By rearrangement and summation over the nearest neighbours of the site  $i$ , the Hamiltonian can be expressed as a sum of single-site Hamiltonians

$$H = \sum_i H_i; \quad H_i = -zJ (\langle \hat{a}_i \rangle \hat{a}_i^\dagger + \langle \hat{a}_i \rangle^* \hat{a}_i - \langle \hat{a}_i \rangle^* \langle \hat{a}_i \rangle) + \frac{U}{2} \hat{n}_i(\hat{n}_i - 1) - \mu \hat{n}_i \quad (\text{B.3})$$

where  $z$  is the co-ordination number of the lattice, and we have used  $\langle \hat{a}_i \rangle = \langle \hat{a}_j \rangle$  as a consequence of homogeneity. The single site Hamiltonian is now just a matrix equation.

The ground state of this equation can be found in a number of ways; for example, by propagating the Hamiltonian in complex time using the Cayley form of the unitary evolution operator (see Eqn. 5.33). For the method to be self-consistent, the Hamiltonian coefficient  $\langle \hat{a}_i \rangle$  must be calculated at each time step.

The results of such calculations are given in Figure 8.1. In the situations in which the ground state has a non-zero  $\langle \hat{a}_i \rangle$ , the ground state is a superposition of more than one Fock state, and so is a superfluid. If  $\langle \hat{a}_i \rangle = 0$ , the ground state is a Fock state, and is a Mott insulator. Thus  $\langle \hat{a}_i \rangle$  is an order parameter of this phase transition.

---

## ASPECTS OF THE DERIVATION OF THE DYNAMICAL EQUATIONS OF POLARISATION GRADIENT COOLING

### C.1 The direction of spontaneously emitted radiation

The classical intensity of the radiation obeys the relation

$$I(\mathbf{r}) \propto \langle \mathbf{E}^*(\mathbf{r})\mathbf{E}(\mathbf{r}) \rangle . \quad (\text{C.1})$$

For the quantum mechanical equivalent of this expression, the electric field must be replaced by the electric field operator; the correct order of the field operators must be used, which can be shown to be ([63] p173)

$$I(\mathbf{r}) \propto \langle \mathbf{E}^-(\mathbf{r})\mathbf{E}^+(\mathbf{r}) \rangle . \quad (\text{C.2})$$

The electric field of the spontaneously scattered light in the far field can be determined from the source-field expression ([63] p328) to have the relation

$$\mathbf{E}^+_{\alpha}(\mathbf{r}) \propto \mathbf{e}_{\alpha} (\mathbf{e}_{\alpha} \cdot \mathbf{D}^-) \quad (\text{C.3})$$

in which the unit vector  $\mathbf{e}_{\alpha}$  is the polarisation vector of the radiation mode labelled by  $\alpha$ .

If we divide the intensity into two perpendicular polarisations, conveniently  $\hat{\theta}$  and  $\hat{\phi}$  in spherical polar coordinates, we get the following relationships for intensity:

$$I_{\theta}(\mathbf{r}) \propto \langle (\hat{\theta}(\boldsymbol{\kappa}) \cdot \mathbf{D}^+) (\hat{\theta}(\boldsymbol{\kappa}) \cdot \mathbf{D}^-) \rangle \quad (\text{C.4})$$

$$I_{\phi}(\mathbf{r}) \propto \langle (\hat{\phi}(\boldsymbol{\kappa}) \cdot \mathbf{D}^+) (\hat{\phi}(\boldsymbol{\kappa}) \cdot \mathbf{D}^-) \rangle \quad (\text{C.5})$$

in which mode  $\alpha$  has been identified by the unit wave vector  $\kappa$  together with the polarisations, and the expectation value runs over the internal degrees of freedom of the atom.

It is convenient to express  $\hat{\theta}$  and  $\hat{\phi}$  in the  $\mp (\hat{x} \pm i\hat{y})$ ,  $z$  co-ordinate basis; in evaluating C.4 we need to remember that we have defined  $\mathbf{D}_{-1}^+ = \mathbf{D}_x^+ - i\mathbf{D}_y^+$  in Equation 5.6. Thus the scattered intensity may be shown to be

$$I_\sigma(\boldsymbol{\kappa}) \propto \sum_{\sigma \varepsilon \varepsilon'} f_{\varepsilon, \varepsilon'}^\sigma \langle \mathbf{D}_\varepsilon^+ \mathbf{D}_{\varepsilon'}^- \rangle . \quad (\text{C.6})$$

Integrating over  $\kappa$ , we set the total scattered power to be  $\hbar\omega\Gamma\langle \mathbf{P} \rangle$  :

$$I_\sigma(\boldsymbol{\kappa}) = \frac{\hbar\omega\Gamma}{r^2} \sum_{\sigma \varepsilon \varepsilon'} f_{\varepsilon, \varepsilon'}^\sigma \langle \mathbf{D}_\varepsilon^+ \mathbf{D}_{\varepsilon'}^- \rangle . \quad (\text{C.7})$$

The coefficients  $f_{\varepsilon, \varepsilon'}^\sigma$  are listed in Table C.1 with this normalisation.

The tensor  $\eta_{\varepsilon \varepsilon' ij}$  of Equation 5.18 are related to the functions  $f_{\varepsilon, \varepsilon'}^\sigma$  by

$$\eta_{\varepsilon \varepsilon' ij} = \sum_\sigma \int d^2\boldsymbol{\kappa} (\boldsymbol{\kappa} \cdot \hat{x}_i)(\boldsymbol{\kappa} \cdot \hat{x}_j) f_{\varepsilon, \varepsilon'}^\sigma \quad (\text{C.8})$$

in which  $\hat{x}_i$  is the unit vector in the  $i$  direction. The tensor  $\eta_{\varepsilon \varepsilon' ij}$  is given in Table C.2.

## C.2 The semiclassical approximation

As outlined above, the semiclassical approximation is taken by terminating the expansion of Taylor series of functions on the right hand side of the Wigner function evolution equation 5.18. In this section, we concentrate on the unitary evolution terms of this equation (those involving  $\mathbf{V}$ ), so the relevant expansion is that of 5.17.

We then must interpret terms such as

$$\int d^3s e^{ip \cdot s / \hbar} \left[ \boldsymbol{\rho} \left( \mathbf{r} + \frac{\mathbf{s}}{2}, \mathbf{r} - \frac{\mathbf{s}}{2}, t \right) \nabla V(\mathbf{r}) \cdot \left( -\frac{\mathbf{s}}{2} \right) \right] . \quad (\text{C.9})$$

These terms may be expressed in terms of the derivative of the Wigner function with respect to momentum:

$$\nabla_p \int d^3s \left\langle \mathbf{r} + \frac{\mathbf{s}}{2} \left| \boldsymbol{\rho} \left| \mathbf{r} - \frac{\mathbf{s}}{2} \right. \right. \right\rangle e^{-ip \cdot s / \hbar} = -\frac{i}{\hbar} \int d^3s \left\langle \mathbf{r} + \frac{\mathbf{s}}{2} \left| \boldsymbol{\rho} \left| \mathbf{r} - \frac{\mathbf{s}}{2} \right. \right. \right\rangle e^{-ip \cdot s / \hbar} \mathbf{s} . \quad (\text{C.10})$$

Table C.1: The parameters  $f_{\varepsilon,\varepsilon'}^\sigma$  of Equation C.7, in terms of the polar angle  $\theta$  and azimuthal angle  $\phi$ .

$f_{\varepsilon,\varepsilon'}^\theta$	$\varepsilon' = -1$	$\varepsilon' = 0$	$\varepsilon' = 1$
$\varepsilon = -1$	$\frac{3}{16\pi} \cos^2 \theta$	$-\frac{3}{16\sqrt{2}\pi} \sin 2\theta e^{-i\phi}$	$-\frac{3}{16\pi} \cos^2 \theta e^{-2i\phi}$
$\varepsilon = 0$	$-\frac{3}{16\sqrt{2}\pi} \sin 2\theta e^{i\phi}$	$\frac{3}{8\pi} \sin^2 \theta$	$\frac{3}{16\sqrt{2}\pi} \sin 2\theta e^{-i\phi}$
$\varepsilon = 1$	$-\frac{3}{16\pi} \cos^2 \theta e^{2i\phi}$	$\frac{3}{16\sqrt{2}\pi} \sin 2\theta e^{i\phi}$	$\frac{3}{16\pi} \cos^2 \theta$

$f_{\varepsilon,\varepsilon'}^\phi$	$\varepsilon' = -1$	$\varepsilon' = 0$	$\varepsilon' = 1$
$\varepsilon = -1$	$\frac{3}{16\pi}$	0	$\frac{3}{16\pi} e^{-2i\phi}$
$\varepsilon = 0$	0	0	0
$\varepsilon = 1$	$\frac{3}{16\pi} e^{2i\phi}$	0	$\frac{3}{16\pi}$

 Table C.2: The tensor  $\eta_{\varepsilon\varepsilon'ij}$  of Equation 5.18.

$\eta_{\varepsilon\varepsilon'ij}$	$\varepsilon' = -1$	$\varepsilon' = 0$	$\varepsilon' = 1$
$\varepsilon = -1$	$\frac{1}{10} \begin{bmatrix} 3 & 0 & 0 \\ 0 & 3 & 0 \\ 0 & 0 & 4 \end{bmatrix}$	$\frac{1}{10\sqrt{2}} \begin{bmatrix} 0 & 0 & -1 \\ 0 & 0 & i \\ -1 & i & 0 \end{bmatrix}$	$\frac{1}{10} \begin{bmatrix} 1 & -i & 0 \\ -i & -1 & 0 \\ 0 & 0 & 0 \end{bmatrix}$
$\varepsilon = 0$	$\frac{1}{10\sqrt{2}} \begin{bmatrix} 0 & 0 & -1 \\ 0 & 0 & -i \\ -1 & -i & 0 \end{bmatrix}$	$\frac{1}{5} \begin{bmatrix} 2 & 0 & 0 \\ 0 & 2 & 0 \\ 0 & 0 & 1 \end{bmatrix}$	$\frac{1}{10\sqrt{2}} \begin{bmatrix} 0 & 0 & 1 \\ 0 & 0 & -i \\ 1 & -i & 0 \end{bmatrix}$
$\varepsilon = 1$	$\frac{1}{10} \begin{bmatrix} 1 & i & 0 \\ i & -1 & 0 \\ 0 & 0 & 0 \end{bmatrix}$	$\frac{1}{10\sqrt{2}} \begin{bmatrix} 0 & 0 & 1 \\ 0 & 0 & i \\ 1 & i & 0 \end{bmatrix}$	$\frac{1}{10} \begin{bmatrix} 3 & 0 & 0 \\ 0 & 3 & 0 \\ 0 & 0 & 4 \end{bmatrix}$

Likewise,

$$\frac{\partial^2}{\partial p_i \partial p_j} \int d^3 s \left\langle \mathbf{r} + \frac{\mathbf{s}}{2} \left| \boldsymbol{\rho} \right| \mathbf{r} - \frac{\mathbf{s}}{2} \right\rangle e^{-i\mathbf{p}\cdot\mathbf{s}/\hbar} = -\frac{1}{\hbar^2} \int d^3 s_i s_j \left\langle \mathbf{r} + \frac{\mathbf{s}}{2} \left| \boldsymbol{\rho} \right| \mathbf{r} - \frac{\mathbf{s}}{2} \right\rangle e^{-i\mathbf{p}\cdot\mathbf{s}/\hbar} . \quad (\text{C.11})$$

We thus gain the  $V$ -containing terms of Equation 5.18.

### C.3 The recoil term: Wigner transformation and small recoil momentum approximation

The transformation of the terms containing the constant matrix  $\mathbf{P}$  is trivial, so this section will concentrate on the last term of Equation 5.11:

$$\Gamma \sum_{\varepsilon, \varepsilon', \sigma} \int d^2 \boldsymbol{\kappa} e^{ik_R \boldsymbol{\kappa} \cdot \mathbf{r}'} \mathbf{D}_{\varepsilon}^- \boldsymbol{\rho} \mathbf{D}_{\varepsilon'}^+ e^{-ik_R \boldsymbol{\kappa} \cdot \mathbf{r}} f_{\varepsilon \varepsilon'}^{\sigma}(\boldsymbol{\kappa}) . \quad (\text{C.12})$$

It is easiest to use the Wigner transformation expressed in the momentum representation, which can be found to be

$$\mathcal{W}\hat{A}(\mathbf{p}, t) = \frac{1}{h^3} \int d^3 \mathbf{q} \left\langle \mathbf{p} + \frac{\mathbf{q}}{2} \left| \hat{A} \right| \mathbf{p} - \frac{\mathbf{q}}{2} \right\rangle e^{i\mathbf{r}\cdot\mathbf{q}/\hbar} . \quad (\text{C.13})$$

The application of this transform onto the term C.12 involves expressions such as

$$e^{-ik_R \boldsymbol{\kappa} \cdot \mathbf{r}} |\mathbf{p}\rangle = |\mathbf{p} - \hbar k_R \boldsymbol{\kappa}\rangle, \quad (\text{C.14})$$

which can be evaluated by identification of the momentum translation operator. The matrices  $\mathbf{D}_{\varepsilon}^{\pm}$  are constant in spatial coordinates, so we end up with the Wigner transformed term

$$\Gamma \sum_{\varepsilon, \varepsilon', \sigma} \int d^2 \boldsymbol{\kappa} \mathbf{D}_{\varepsilon}^- \mathcal{W}(\mathbf{r}, \mathbf{p} + \hbar k_R \boldsymbol{\kappa}, t) \mathbf{D}_{\varepsilon'}^+ f_{\varepsilon \varepsilon'}^{\sigma}(\boldsymbol{\kappa}) . \quad (\text{C.15})$$

In the small momentum approximation, we expand terms on the right hand side of the evolution equation 5.18 in a Taylor series around  $\mathbf{r}$  and  $\mathbf{p}$ :

$$\mathcal{W}(\mathbf{r}, \mathbf{p} + \mathbf{q}', t) = \mathcal{W}(\mathbf{r}, \mathbf{p}, t) + \mathbf{q}' \cdot \nabla_{\mathbf{p}} \mathcal{W}(\mathbf{r}, \mathbf{p}, t) + \frac{1}{2} (\mathbf{q}' \cdot \nabla_{\mathbf{p}})^2 \mathcal{W}(\mathbf{r}, \mathbf{p}, t) + \dots . \quad (\text{C.16})$$

We then need to perform the integrals over the unit sphere, and sum over the polarisations; the terms containing odd powers of kappa will vanish, leaving the term

$$\frac{\Gamma \hbar^2 k_R^2}{2} \sum_{\varepsilon, \varepsilon', i, j} \eta_{\varepsilon \varepsilon' ij} \mathbf{D}_{\varepsilon}^- \frac{\partial^2 \mathcal{W}}{\partial p_i \partial p_j} \mathbf{D}_{\varepsilon'}^+ \quad (\text{C.17})$$

with the tensor  $\eta_{\varepsilon \varepsilon' ij}$  defined in Equation C.8.

#### C.4 Conversion to Langevin form

The conversion of Equation 5.18 to Langevin form is achieved the substitution the trial solution 5.21. We wish to have a trajectory characterised by quantum internal states but classical external states. This means we should take the expectation value over all external quantum states when finding the equation of motion for the internal coordinates; when finding the equation of motion for the external classical coordinates (which are themselves expectation values), we should integrate over all quantum coordinates, i.e. internal and external.

The evolution equation for the internal state 5.22 follows simply, so we will concentrate on the derivation of the equations of motion for the external coordinates 5.23 to 5.26. A key relation concerns the derivatives of the delta distribution

$$\int dx f(x) \frac{\partial^n \delta}{\partial x^n} = - \int dx \frac{df(x)}{dx} \frac{\partial^{n-1} \delta}{\partial x^{n-1}}. \quad (\text{C.18})$$

Using this relation we can find the equations of motion for  $\tilde{\mathbf{r}} = \langle \mathbf{r} \rangle$  etc. The non-zero expectation value for the second moments of momentum should be interpreted as a Langevin force.

#### C.5 The quantum Monte Carlo wave function method and the optical Bloch equation

The object of this section is to show that the Quantum Monte Carlo wave function, as set out in Equations 5.28 to 5.32 in Section 5.8, satisfies the optical Bloch Equation (Eqn. 5.22).

Without a quantum jump, the un-normalised density matrix at time  $t + \delta t$  is

$$|\psi(t + \delta t)\rangle\langle\psi(t + \delta t)| = \left(1 - \frac{i}{\hbar}\delta t \mathbf{H}'\right) |\psi(t)\rangle\langle\psi(t)| \left(1 + \frac{i}{\hbar}\delta t \mathbf{H}'^\dagger\right). \quad (\text{C.19})$$

Substituting for  $\mathbf{H}'$  and ignoring terms of order  $(\delta t)^2$  we find

$$|\psi(t + \delta t)\rangle\langle\psi(t + \delta t)| = |\psi(t)\rangle\langle\psi(t)| - \frac{i}{\hbar}\delta t [\mathbf{V}, |\psi(t)\rangle\langle\psi(t)|] - \frac{1}{2}\Gamma\delta t \{\mathbf{P}, |\psi(t)\rangle\langle\psi(t)|\};. \quad (\text{C.20})$$

Normalising this density matrix requires division by

$$1 - \Gamma\delta t \langle \mathbf{P} \rangle. \quad (\text{C.21})$$

On the other hand, with a quantum jump, the normalised density matrix at time  $t + \delta t$  is

$$|\psi(t + \delta t)\rangle\langle\psi(t + \delta t)| = \frac{D_{\varepsilon}^{-}|\psi(t)\rangle\langle\psi(t)|D_{\varepsilon}^{+}}{\langle D_{\varepsilon}^{+}D_{\varepsilon}^{-}\rangle}. \quad (\text{C.22})$$

Combining the alternatives using the definition of the density matrix

$$\mathbf{w} = \sum_i p_i |\phi_i\rangle\langle\phi_i| \quad (\text{C.23})$$

we find

$$\begin{aligned} \mathbf{w}(t + \delta t) &= (1 - \Gamma\delta t\langle\mathbf{P}\rangle) \frac{\mathbf{w}(t) - \frac{i}{\hbar}\delta t [V, \mathbf{w}(t)] - \frac{1}{2}\Gamma\delta t \{\mathbf{P}, \mathbf{w}(t)\}}{1 - \Gamma\delta t\langle\mathbf{P}\rangle} \\ &+ \sum_{\varepsilon} \Gamma\delta t \langle D_{\varepsilon}^{+}D_{\varepsilon}^{-}\rangle \frac{D_{\varepsilon}^{-}\mathbf{w}(t)D_{\varepsilon}^{+}}{\langle D_{\varepsilon}^{+}D_{\varepsilon}^{-}\rangle} \end{aligned} \quad (\text{C.24})$$

which reduces to the optical Bloch equation 5.22.

## BIBLIOGRAPHY

- [1] M. Anderlini, E. Courtade, D. Ciampini, J. Müller, O. Morsch, and E. Arimondo, *Two-photon ionization of cold rubidium atoms*, Journal of the Optical Society of America B, **21**, 480 (2004).
- [2] M. Anderlini, P. J. Lee, B. L. Brown, J. Sebby-Strabley, W. D. Phillips, and J. V. Porto, *Controlled exchange interaction between pairs of neutral atoms in an optical lattice*, Nature, **448**, 452 (2007).
- [3] M. H. Anderson, J. R. Ensher, M. R. Matthews, C. E. Wieman, and E. A. Cornell, *Observation of Bose-Einstein condensation in a dilute atomic vapor*, Science, **269**, 198 (1995).
- [4] W. S. Bakr, J. I. Gillen, A. Peng, S. Foelling, and M. Greiner, *A quantum gas microscope - detecting single atoms in a Hubbard regime optical lattice*, arXiv: 0908.0174 (2009).
- [5] P. Bouyer and M. A. Kasevich, *Heisenberg-limited spectroscopy with degenerate Bose-Einstein gases*, Physical Review A, **56**, R1083 (1997).
- [6] T. Brys, S. Czekaj, M. Daum, P. Fierlinger, D. George, R. Henneck, Z. Hochman, et al, *Magnetic field stabilization for magnetically shielded volumes by external field coils*, Journal of Research of the National Institute of Standards and Technology, **110**, 173 (2005).
- [7] G. K. Campbell, J. Mun, M. Boyd, P. Medley, A. E. Leanhardt, L. G. Marcassa, D. E. Pritchard, and W. Ketterle, *Imaging the Mott insulator shells by using atomic clock shifts*, Science, **313**, 649 (2006).

- 
- [8] Y. Castin and J. Dalibard, *Quantization of atomic motion in optical molasses*, Europhysics Letters, **14**, 761 (1991).
- [9] P. Cheinet, S. Trotzky, M. Feld, U. Schnorrberger, M. Moreno-Cardoner, S. Fölling, and I. Bloch, *Counting atoms using interaction blockade in an optical superlattice*, Physical Review Letters, **101**, 090404 (2008).
- [10] A. Cho, *Condensed-matter physics: The mad dash to make light crystals*, Science, **320**, 312 (2008).
- [11] C. S. Chuu, F. Schreck, T. P. Meyrath, J. L. Hanssen, G. N. Price, and M. G. Raizen, *Direct observation of sub-Poissonian number statistics in a degenerate Bose gas*, Physical Review Letters, **95**, 260403 (2005).
- [12] D. Ciampini, M. Anderlini, J. H. Müller, F. Fuso, O. Morsch, J. W. Thomsen, and E. Arimondo, *Photoionization of ultracold and Bose-Einstein-condensed Rb atoms*, Physical Review A, **66**, 043409 (2002).
- [13] J. I. Cirac, P. Zoller, H. J. Kimble, and H. Mabuchi, *Quantum state transfer and entanglement distribution among distant nodes in a quantum network*, Physical Review Letters, **78**, 3221 (1997).
- [14] C. Cohen-Tannoudji, *Atomic motion in laser light*, in *Fundamental systems in quantum optics*, Proceedings of the Les Houches Summer School 1990, p. 91 (Elsevier, Amsterdam, 1992).
- [15] C. Cohen-Tannoudji, J. Dupont-Roc, and G. Grynberg, *Atom-photon interactions* (Wiley-VCH, Berlin, 2004).
- [16] Y. Colombe, E. Knyazchyan, O. Morizot, B. Mercier, V. Lorent, and H. Perrin, *Ultracold atoms confined in RF-induced two-dimensional trapping potentials*, Europhysics Letters, **67**, 593 (2004).
- [17] N. R. Cooper and N. K. Wilkin, *Composite fermion description of rotating Bose-Einstein condensates*, Physical Review B, **60**, R16279 (1999).

- 
- [18] J. Dalibard and C. Cohen-Tannoudji, *Laser cooling below the Doppler limit by polarization gradients: simple theoretical models*, Journal of the Optical Society of America B, **6**, 2023 (1989).
- [19] B. Damski, J. Zakrzewski, L. Santos, P. Zoller, and M. Lewenstein, *Atomic Bose and Anderson glasses in optical lattices*, Physical Review Letters, **91**, 080403 (2003).
- [20] K. B. Davis, M. O. Mewes, M. R. Andrews, N. J. V. Druten, D. S. Durfee, D. M. Kurn, and W. Ketterle, *Bose-Einstein condensation in a gas of sodium atoms*, Physical Review Letters, **75**, 3969 (1995).
- [21] C. M. Dion, P. Sjölund, S. J. H. Petra, S. Jonsell, and A. Kastberg, *Time dependence of laser cooling in optical lattices*, Europhysics Letters, **72**, 369 (2005).
- [22] L. Fallani, C. Fort, J. E. Lye, and M. Inguscio, *Bose-Einstein condensate in an optical lattice with tunable spacing: transport and static properties*, Optics Express, **13**, 4303 (2005).
- [23] S. Fölling, A. Widera, T. Müller, F. Gerbier, and I. Bloch, *Formation of spatial shell structure in the superfluid to Mott insulator transition*, Physical Review Letters, **97**, 060403 (2006).
- [24] M. J. J. Garvels, J. K. C. W. V. Ommeren, and D. P. Kroese, *On the importance function in splitting simulation*, European Transactions on Telecommunications, **13**, 363 (2002).
- [25] N. Gemelke, X. Zhang, C. Hung, and C. Chin, *In situ observation of incompressible Mott-insulating domains in ultracold atomic gases*, Nature, **460**, 995 (2009).
- [26] T. Gericke, P. Wurtz, D. Reitz, T. Langen, and H. Ott, *High-resolution scanning electron microscopy of an ultracold quantum gas*, Nature Physics, **4**, 949 (2008).
- [27] P. Glasserman, P. Heidelberger, P. Shahabuddin, and T. Zajic, *Multilevel splitting for estimating rare event probabilities*, Operations Research, **47**, 585 (1999).

- [28] M. Greiner, O. Mandel, T. Esslinger, T. W. Hänsch, and I. Bloch, *Quantum phase transition from a superfluid to a Mott insulator in a gas of ultracold atoms*, *Nature*, **415**, 39 (2002).
- [29] A. Griessner, A. J. Daley, S. R. Clark, D. Jaksch, and P. Zoller, *Dark-state cooling of atoms by superfluid immersion*, *Physical Review Letters*, **97**, 220403 (2006).
- [30] R. Grimm, M. Weidemüller, and Y. B. Ovchinnikov, *Optical dipole traps for neutral atoms*, in *Advances in atomic, molecular, and optical physics*, vol. 42, pp. 95–170 (Elsevier, Amsterdam, 1999).
- [31] H. Gross, *Handbook of optical systems, volume 3, Aberration theory and correction of optical systems*, p. 225 (Wiley-VCH, Berlin, 2007).
- [32] G. Grynberg and C. Robilliard, *Cold atoms in dissipative optical lattices*, *Physics Reports*, **355**, 335 (2001).
- [33] R. Gupta, J. J. McClelland, P. Marte, and R. J. Celotta, *Raman-induced avoided crossings in adiabatic optical potentials: Observation of  $\lambda/8$  spatial frequency in the distribution of atoms*, *Physical Review Letters*, **76**, 4689 (1996).
- [34] D. J. Han, S. Wolf, S. Oliver, C. McCormick, M. T. DePue, and D. S. Weiss, *3D Raman sideband cooling of cesium atoms at high density*, *Physical Review Letters*, **85**, 724 (2000).
- [35] D. Hayes, P. S. Julienne, and I. H. Deutsch, *Quantum logic via the exchange blockade in ultracold collisions*, *Physical Review Letters*, **98**, 070501 (2007).
- [36] W. H. Heathcote, E. Nugent, B. T. Sheard, and C. J. Foot, *A ring trap for ultracold atoms in an RF-dressed state*, *New Journal of Physics*, **10**, 043012 (2008).
- [37] S. Hofferberth, I. Lesanovsky, B. Fischer, J. Verdu, and J. Schmiedmayer, *Radiofrequency-dressed-state potentials for neutral atoms*, *Nature Physics*, **2**, 710 (2006).

- 
- [38] C. Honerkamp and W. Hofstetter, *Ultracold fermions and the  $SU(N)$  Hubbard model*, Physical Review Letters, **92**, 170403 (2004).
- [39] S. Inouye, M. R. Andrews, J. Stenger, H. J. Miesner, D. M. Stamper-Kurn, and W. Ketterle, *Observation of Feshbach resonances in a Bose-Einstein condensate*, Nature, **392**, 151 (1998).
- [40] A. Itah, H. Veksler, O. Lahav, A. Blumkin, C. Moreno, C. Gordon, and J. Steinhauer, *Direct observation of number squeezing in an optical lattice*, arXiv:0903.3282 (2009).
- [41] D. Jaksch, H. J. Briegel, J. I. Cirac, C. W. Gardiner, and P. Zoller, *Entanglement of atoms via cold controlled collisions*, Physical Review Letters, **82**, 1975 (1999).
- [42] D. Jaksch, C. Bruder, J. I. Cirac, C. W. Gardiner, and P. Zoller, *Cold bosonic atoms in optical lattices*, Physical Review Letters, **81**, 3108 (1998).
- [43] D. Jaksch and P. Zoller, *Creation of effective magnetic fields in optical lattices: the Hofstadter butterfly for cold neutral atoms*, New Journal of Physics, **5**, 56.1 (2003).
- [44] D. Jaksch and P. Zoller, *The cold atom Hubbard toolbox*, Annals of Physics, **315**, 52 (2005).
- [45] J. Javanainen, *Phonon approach to an array of traps containing Bose-Einstein condensates*, Physical Review A, **60**, 4902 (1999).
- [46] T. Jelte, J. M. McNamara, W. Hogervorst, W. Vassen, V. Krachmalnicoff, M. Schellekens, A. Perrin, et al, *Comparison of the Hanbury Brown-Twiss effect for bosons and fermions*, Nature, **445**, 402 (2007).
- [47] S. Jonsell, C. M. Dion, M. Nylén, S. J. H. Petra, P. Sjölund, and A. Kastberg, *A nonadiabatic semi-classical method for dynamics of atoms in optical lattices*, European Physical Journal D, **39**, 67 (2006).

- [48] M. Karski, L. Frster, J. M. Choi, W. Alt, A. Widera, and D. Meschede, *Nearest-neighbor detection of atoms in a 1D optical lattice by fluorescence imaging*, Physical Review Letters, **102**, 053001 (2009).
- [49] M. Kasevich and S. Chu, *Laser cooling below a photon recoil with three-level atoms*, Physical Review Letters, **69**, 1741 (1992).
- [50] A. Kastberg, W. D. Phillips, S. L. Rolston, R. J. C. Spreeuw, and P. S. Jessen, *Adiabatic cooling of cesium to 700 nK in an optical lattice*, Physical Review Letters, **74**, 1542 (1995).
- [51] A. J. Kerman, V. Vuletić, C. Chin, and S. Chu, *Beyond optical molasses: 3D Raman sideband cooling of atomic cesium to high phase-space density*, Physical Review Letters, **84**, 439 (2000).
- [52] W. Ketterle, D. S. Dufree, and D. M. Stamper-Kurn, *Making, probing and understanding Bose-Einstein condensates*, in *Proceedings of the International School of Physics "Enrico Fermi"* (IOS Press, Amsterdam, 1999).
- [53] M. Köhl, H. Moritz, T. Stöferle, C. Schori, and T. Esslinger, *Superfluid to Mott insulator transition in one, two, and three dimensions*, Journal of Low Temperature Physics, **138**, 635 (2005).
- [54] S. Kraft, A. Günther, J. Fortágh, and C. Zimmermann, *Spatially resolved photoionization of ultracold atoms on an atom chip*, Physical Review A, **75**, 063605 (2007).
- [55] T. D. Kühner, S. R. White, and H. Monien, *One-dimensional Bose-Hubbard model with nearest-neighbor interaction*, Physical Review B, **61**, 12474 (2000).
- [56] S. Kuhr, W. Alt, D. Schrader, M. Müller, V. Gomer, and D. Meschede, *Deterministic delivery of a single atom*, Science, **293**, 278 (2001).
- [57] P. L'Ecuyer, V. Demers, and B. Tuffin, *Rare events, splitting, and quasi-Monte Carlo*, ACM Transactions on Modeling and Computer Simulation, **17**, 9 (2007).

- 
- [58] P. J. Lee, M. Anderlini, B. L. Brown, J. Sebby-Strabley, W. D. Phillips, and J. V. Porto, *Sublattice addressing and spin-dependent motion of atoms in a double-well lattice*, Physical Review Letters, **99**, 020402 (2007).
- [59] P. D. Lett, R. N. Watts, C. I. Westbrook, W. D. Phillips, P. L. Gould, and H. J. Metcalf, *Observation of atoms laser-cooled below the Doppler limit*, Physical Review Letters, **61**, 169 (1988).
- [60] J. Li, V. Yu, A. M. Dudarev, and Q. Niu, *Interaction broadening of Wannier functions and Mott transitions in atomic BEC*, New Journal of Physics, **8**, 154 (2006).
- [61] T. C. Li, H. Kelkar, D. Medellin, and M. G. Raizen, *Real-time control of the periodicity of a standing wave: an optical accordion*, Optics Express, **16**, 5465 (2008).
- [62] R. L. Liboff, *Kinetic theory: classical, quantum, and relativistic descriptions* (Springer, New York, 2003).
- [63] R. Loudon, *The quantum theory of light* (Oxford University Press, Oxford, 2000).
- [64] N. Lundblad, P. J. Lee, I. B. Spielman, B. L. Brown, W. D. Phillips, and J. V. Porto, *Atoms in a radio-frequency-dressed optical lattice*, Physical Review Letters, **100**, 150401 (2008).
- [65] O. Mandel, M. Greiner, A. Widera, T. Rom, T. W. Hänsch, and I. Bloch, *Controlled collisions for multi-particle entanglement of optically trapped atoms*, Nature, **425**, 937 (2003).
- [66] N. Marzari and D. Vanderbilt, *Maximally localized generalized Wannier functions for composite energy bands*, Physical Review B, **56**, 12847 (1997).
- [67] H. J. Metcalf and P. V. der Straten, *Laser cooling and trapping* (Springer, 1999).

- [68] Y. Miroshnychenko, W. Alt, I. Dotsenko, L. Förster, M. Khudaverdyan, A. Rauschenbeutel, and D. Meschede, *Precision preparation of strings of trapped neutral atoms*, *New Journal of Physics*, **8**, 191 (2006).
- [69] A. J. Moerdijk, B. J. Verhaar, and T. M. Nagtegaal, *Collisions of dressed ground-state atoms*, *Physical Review A*, **53**, 4343 (1996).
- [70] K. Mølmer, Y. Castin, and J. Dalibard, *Monte Carlo wave-function method in quantum optics*, *Journal of the Optical Society of America B*, **10**, 524 (1993).
- [71] K. D. Nelson, X. Li, and D. S. Weiss, *Imaging single atoms in a three-dimensional array*, *Nature Physics*, **3**, 556 (2007).
- [72] M. A. Nielsen and I. L. Chuang, *Quantum computation and quantum information* (Cambridge University Press, 2000).
- [73] D. V. Oosten, P. V. der Straten, and H. T. C. Stoof, *Quantum phases in an optical lattice*, *Physical Review A*, **63**, 053601 (2001).
- [74] C. Orzel, A. K. Tuchman, M. L. Fenselau, M. Yasuda, and M. A. Kasevich, *Squeezed states in a Bose-Einstein condensate*, *Science*, **291**, 2386 (2001).
- [75] A. Öttl, S. Ritter, M. Köhl, and T. Esslinger, *Hybrid apparatus for Bose-Einstein condensation and cavity quantum electrodynamics: single atom detection in quantum degenerate gases*, *Review of Scientific Instruments*, **77**, 063118 (2006).
- [76] B. Paredes, A. Widera, V. Murg, O. Mandel, S. Fölling, I. Cirac, G. V. Shlyapnikov, et al, *Tonks-Girardeau gas of ultracold atoms in an optical lattice*, *Nature*, **429**, 277 (2004).
- [77] C. J. Pethick and H. Smith, *Bose-Einstein condensation in dilute gases* (Springer, New York, 2002).
- [78] K. I. Petsas, G. Grynberg, and J. Y. Courtois, *Semiclassical Monte Carlo approaches for realistic atoms in optical lattices*, *European Physical Journal D*, **6**, 29 (1999).

- [79] G. Raithel, G. Birkl, A. Kastberg, W. D. Phillips, and S. L. Rolston, *Cooling and localization dynamics in optical lattices*, Physical Review Letters, **78**, 630 (1997).
- [80] A. Reischl, K. P. Schmidt, and G. S. Uhrig, *Temperature in one-dimensional bosonic Mott insulators*, Physical Review A, **72**, 063609 (2005).
- [81] J. L. Roberts, N. R. Claussen, J. P. Burke, C. H. Greene, E. A. Cornell, and C. E. Wieman, *Resonant magnetic field control of elastic scattering in cold  $^{85}\text{Rb}$* , Physical Review Letters, **81**, 5109 (1998).
- [82] I. I. Ryabtsev, D. B. Tretyakov, and I. I. Beterov, *Applicability of Rydberg atoms to quantum computers*, Journal of Physics B, **38**, S421 (2005).
- [83] C. Salomon, J. Dalibard, W. D. Phillips, A. Clairon, and S. Guellati, *Laser cooling of cesium atoms below  $3\ \mu\text{K}$* , Europhysics Letters, **12**, 683 (1990).
- [84] L. Santos, M. A. Baranov, J. I. Cirac, H. U. Everts, H. Fehrmann, and M. Lewenstein, *Atomic quantum gases in Kagomé lattices*, Physical Review Letters, **93**, 030601 (2004).
- [85] M. Schellekens, R. Hoppeler, A. Perrin, J. V. Gomes, D. Boiron, A. Aspect, and C. I. Westbrook, *Hanbury Brown Twiss effects for ultracold quantum gases*, Science, **310**, 648 (2005).
- [86] W. Schleich, *Quantum optics in phase space*, p. 74 (Wiley-VCH, Berlin, 2001).
- [87] N. Schlosser, G. Reymond, and P. Grangier, *Collisional blockade in microscopic optical dipole traps*, Physical Review Letters, **89**, 023005 (2002).
- [88] U. Schneider, L. Hackermüller, S. Will, T. Best, I. Bloch, T. A. Costi, R. W. Helmes, et al, *Metallic and insulating phases of repulsively interacting fermions in a 3D optical lattice*, Science, **322**, 1520 (2008).

- [89] J. Sebby-Strabley, M. Anderlini, P. S. Jessen, and J. V. Porto, *Lattice of double wells for manipulating pairs of cold atoms*, Physical Review A, **73**, 033605 (2006).
- [90] P. W. Shor, *Polynomial-time algorithms for prime factorization and discrete logarithms on a quantum computer*, SIAM Journal on Computing, **26**, 1484 (1997).
- [91] M. Shotton, D. Trypogeorgos, and C. Foot, *Enhancement of on-site interactions of tunneling ultracold atoms in optical potentials using radio-frequency dressing*, Physical Review A, **78**, 051602 (2008).
- [92] A. Stibor, S. Kraft, T. Campey, D. Komma, A. Günther, J. Fortágh, C. J. Vale, et al, *Calibration of a single-atom detector for atomic microchips*, Physical Review A, **76**, 033614 (2007).
- [93] K. A. Suominen, E. Tiesinga, and P. S. Julienne, *Nonadiabatic dynamics in evaporative cooling of trapped atoms by a radio-frequency field*, Physical Review A, **58**, 3983 (1998).
- [94] E. Tiesinga, B. J. Verhaar, and H. T. C. Stoof, *Threshold and resonance phenomena in ultracold ground-state collisions*, Physical Review A, **47**, 4114 (1993).
- [95] A. Öttl, S. Ritter, M. Köhl, and T. Esslinger, *Correlations and counting statistics of an atom laser*, Physical Review Letters, **95**, 090404 (2005).
- [96] P. J. Ungar, D. S. Weiss, E. Riis, and S. Chu, *Optical molasses and multilevel atoms: theory*, Journal of the Optical Society of America B, **6**, 2058 (1989).
- [97] M. Villén-Altamirano and J. Villén-Altamirano, *Analysis of RESTART simulation: theoretical basis and sensitivity study*, European Transactions on Telecommunications, **13**, 373 (2002).
- [98] N. K. Wilkin and J. M. F. Gunn, *Condensation of “composite bosons” in a rotating BEC*, Physical Review Letters, **84**, 6 (2000).

- 
- [99] R. A. Williams, J. D. Pillet, S. Al-Assam, B. Fletcher, M. Shotton, and C. J. Foot, *Dynamic optical lattices: two-dimensional rotating and accordion lattices for ultracold atoms*, Optics Express, **16**, 16977 (2008).
- [100] W. Yi, A. J. Daley, G. Pupillo, and P. Zoller, *State-dependent, addressable sub-wavelength lattices with cold atoms*, New Journal of Physics, **10**, 073015 (2008).
- [101] S. Yoon, Y. Choi, S. Park, J. Kim, J. H. Lee, and K. An, *Definitive number of atoms on demand: controlling the number of atoms in a few-atom magneto-optical trap*, Applied Physics Letters, **88**, 211104 (2006).
- [102] C. Zener, *Non-adiabatic crossing of energy levels*, Proceedings of the Royal Society A, **137**, 696 (1932).
- [103] R. Zhang, N. V. Morrow, P. R. Berman, and G. Raithel, *Laser cooling in an optical lattice that employs Raman transitions*, Physical Review A, **72**, 043409 (2005).
- [104] W. Zwerger, *Mott-Hubbard transition of cold atoms in optical lattices*, Journal of Optics B, **5**, S9 (2003).